Cold Atom Microtraps above a Videotape Surface

Jocelyn Anna Retter

Submitted for the degree of D. Phil.

University of Sussex

December, 2002

Declaration

I hereby declare that this thesis has not been submitted, either in the same or different form, to this or any other University for a degree.

Acknowledgements

Of the many people who deserve mention, I would especially like to thank the following:

Ed Hinds, the guiding force behind the experiment, for the opportunity to work in SCOAP. His enthusiasm for physics is quite inspiring. I have learnt a great deal from his approach to the experiment and have greatly appreciated his excellent supervision.

Brenton Hall has worked on this experiment all the time I have been here — without his effort, none of the work presented in this thesis would have been accomplished!

Peter Rosenbusch, for guiding me through the experiment when I arrived, getting the new experiments going, recording endless reels of videotape and providing me with much encouragement.

Ben Sauer, who keeps the entire lab running smoothly and has always made time to help with any technical problems.

Chris Sinclair, who in his first few months in the group, helped acquire some much needed, last-minute data.

Alan Butler and John Knight, who have constructed many components of the experiment.

Matt Jones, with whom I have shared a lab, an office and a house, not to mention the entire thesis-writing experience [36]. Thank you for sharing all the ups and downs of lab-life!

Everyone in SCOAP — I've learnt lots working with you all and it's been great fun too.

And finally, my family, for their support and encouragement.

Cold Atom Microtraps above a Videotape Surface

Jocelyn Anna Retter

Submitted for the degree of D. Phil.

University of Sussex

December, 2002

Summary

Much progress has been made in the last two years towards miniaturizing magnetic traps for cold atoms. This will enable manipulation of coherent samples of atoms, such as Bose-Einstein condensates, or single atoms, on the scale of the atomic de Broglie wavelength.
This thesis concerns an array of microscopic magnetic potentials formed close to the surface of magnetized videotape, when a uniform bias field is applied. The recorded magnetization is a $100\,\mu$m sine wave, which covers a $12.5\,\text{mm} \times 22\,\text{mm}$ piece of commercial videotape. This videotape is glued flat onto a thin glass substrate and is gold coated by evaporation so that atoms can be trapped close to the surface in a mirror-MOT. An 'atom chip' has been developed, incorporating the videotape and current-carrying wires located below the magnetized surface. A single wire and bias field create a magnetic tube potential, oriented parallel with the microtraps and with a quadrupole radial field. This allows the mirror-MOT to be compressed and distorted in order to match it to a magnetic trap formed by the same wire and bias field. Increasing the bias field and reducing the wire current further compresses the atom cloud and brings it closer to the surface, until it is fully transferred to the videotape microtraps. The atom cloud is confined axially by the potential produced by two parallel current-carrying wires with 8mm separation.
This is the first demonstration of loading cold atoms into microtraps formed above a permanently magnetized surface. It is interesting to compare the properties of such traps with those formed above current carrying wires. We present measurements of the lifetimes of trapped atom clouds as a function of height and trap frequency. These results suggest that this technology may prove to be a promising basis for future experiments with atom chips.

Contents

List of Figures

List of Tables

Chapter 1

Introduction

1.1 Research area

The manipulation of atomic trajectories using static magnetic fields was first demonstrated in 1921 by Stern and Gerlach [1]. For the next 50 years, such experiments were restricted to thermal atomic beams [2], which have a large kinetic energy and velocity spread. The development of laser cooling and trapping techniques [3, 4] in the 1980s has made it possible to routinely prepare cold clouds of atoms at temperatures of a few microkelvin. At such temperatures, the thermal energy of the atoms is no longer dominant and atoms can be trapped and controlled using modest magnetic and optical potentials. More importantly, the atomic de Broglie wavelength becomes significant at low atomic momenta, enabling exploitation of the wave-like properties of atoms.

The availability of a source of cold atoms has provoked rapid progress in the field of Atom Optics [5, 6] over the last two decades. Many atom-optical analogues of standard optical elements have been demonstrated: mirrors [7, 8, 9, and references therein], lenses [10, 11, 12], gratings [13, 14, 15] and guides [16, 17]. These generally fall into two broad categories - those based on optical forces [7], and those based on magnetic forces. The exception is the use of the quantum reflection of slow atoms from the attractive van der Waals potential at a solid surface [18, 19].

The future of atom optics lies in combining these atom-optical elements to form integrated atom-optical devices. One could envisage such a device which combines several elements, together with a cold atom source, a detection method and a means of transport between the elements, on a common substrate. Much research effort is now directed at miniature substrate-based atom optics experiments, known as *atom chips*, by analogy with their microelectronic counterparts. Atom chips pro-

vide a powerful method for miniaturizing atom-optical devices and for combining such elements in a robust manner. Established nanofabrication techniques, developed for the microelectronics and opto-electronic communications industries, can be used for fabrication of miniature lens systems, or of sub-micron scale patterned magnetizations or conductors on a substrate. The manufacturing processes allow for accurate reproduction, scalability and integration of different components on a single substrate.

Atom optics techniques were initially developed using thermal clouds of atoms, but the achievements of both Bose-Einstein condensation in dilute gases [20] and single atom trapping [21, 22] open up a wealth of new applications for atom chips, for example to Quantum Information Processing (QIP) [23, 24], cavity QED [25, 26], atom-interferometry [27, 28, 29] and low-dimensional physics [30, 31]. Atom chips are particularly suited to many of these applications as miniaturization allows steep trapping potentials to be created. These tight traps can have a large energy level spacing, which can be greater than the atomic thermal energy. Experiments with single atoms require steep potentials for precise control of the atom. This is important for cavity QED and QIP, where strong localization and defined spacing of qubits is required. Trapping potentials with large energy level spacings can be used to restrict BEC to one or two dimensions, to create so-called quasi-condensates and Tonks gases [30]. Waveguides with large transverse energy level spacings can be used to isolate BEC from environmental fluctuations, leading to more stable coherent transport.

1.2 Atom chip experiments

Several research groups around the world are using atom chips to created microscopic magnetic potentials for experiments with cold atoms. Most of these atom chips are based on magnetic potentials formed above microfabricated conductors [32, 33, 17, 34, 35], or supported wires [36]. The principle here is that the small wires create a strong magnetic field gradient, while a superimposed uniform bias field makes a zero whose position is adjustable. Magnetic traps have proved to be particularly versatile, since any atomic species with a magnetic moment can be trapped. The atom chip presented in this thesis is unique in that a microscopic pattern of permanent magnetization is used to create the micropotentials. The pattern is a $100\,\mu$m sine wave, recorded onto a piece of videotape. This magnetization generates a strong field gradient above the videotape surface. Applying a uniform bias field creates an array of two-dimensional microscopic traps, as illustrated in

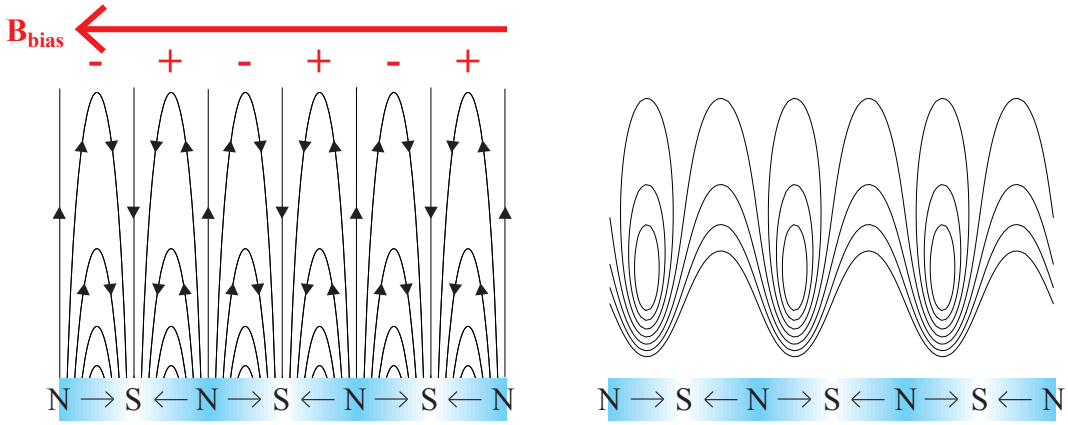

Figure 1.1 *Magnetic microtraps above magnetized videotape. An in-plane periodic magnetization pattern gives rise to an exponentially decaying magnetic field above the surface — the field lines are shown in the left-hand image above. When a uniform bias field is applied, the magnetic field cancels periodically above the surface to form an array of microtraps, as indicated by the closed magnetic field strength contours in the right-hand image. These traps extend in the direction orthogonal to the page, so can be visualized as an array of tubes, spaced by the wavelength of the recorded pattern.*

Figure 1.1. The strong surface field of the videotape, 215 G, provides a steep barrier between the ultra cold atom cloud and the room-temperature surface. In this thesis, we present the first demonstration of loading atoms into microtraps above a permanently magnetized surface.

The main advantage of microtraps is realized at small distances from the surface, where the high field gradients provide steep trapping potentials. Normally, the coupling between magnetically trapped atoms and the far-field blackbody radiation of their room-temperature environment is very weak and so the ultracold atoms are thermally isolated from their surroundings. As the atom–surface distance is reduced into the micron range, it is possible that the atoms will be perturbed by coupling to the near field of the surface. For the purposes of future experiments with coherent matter waves, or even single atoms in microtraps close to surfaces, the mutual influences of the atoms and the surface needs to be understood. We expect to observe some differences between the behaviour of atoms trapped above videotape and atoms trapped above current-carrying wires, particularly with respect to the lifetime of trapped clouds.

Henkel *et al* [37] have made theoretical predictions of the nature of atom–surface interactions and the length and time scales associated with these. One possible

source of interactions concerns atoms trapped above a conducting surface. The existence of thermally driven current fluctuations in the surface would lead to fluctuations in the near field above the surface. A subsequent increase in atom loss rate would be expected within ~ 10 microns of the surface. Atom chips based on current-carrying wires typically have wire thickness of several microns. In contrast, our atom chip surface is a dielectric layer (the videotape surface) coated with a thin layer of gold, so that it is optically reflective. This gold coating is very thin, $\sim 100\,\mathrm{nm}$: current fluctuations will be confined to a much thinner layer, leading to much smaller field fluctuations.

Surprisingly, Fortágh *et al* [38] have observed a linear dependence of lifetime on distance from the surface, over a range of $20 - 300\,\mu$m. We have measured lifetimes for atoms trapped at a range of distances from the surface, from $30\,\mu$m to 1 mm. In contrast, we see no variation of the low-density lifetime with proximity to the surface, nor do we observe any dependence on trap frequency, as discussed in Section 6.9 of this thesis.

Recently, several groups have observed that a cloud trapped within $40\,\mu$m of the surface begins to fragment into several smaller clouds at temperatures below $60\,\mu$K [38, 39, 40]. Kraft *et al* [41] have shown that this is due to a non-uniform longitudinal field formed above copper current-carrying wires. This modifies the depth of the tube potential along its length by up to 10 mG. The cause of the field is unknown — it must arise from a transverse current flow in the conductor. This fragmentation may ultimately impose a limit on the distance from the surface at which atoms can be trapped for experiments above conducting wires, thus limiting the trap gradient. If this proves to be the case, then atom chips based on permanent magnetization patterns could prove to be a suitable alternative.

The challenge of loading cold atoms into microscopic traps has been achieved in several ways: in one experiment atoms are precooled in a standard, six-beam MOT, then transferred to the chip using macroscopic wire traps [42]; Gustavson *et al* [43] have used the method of optical tweezers to transport a BEC from a separate trapping region to the atom chip, where it was loaded into a guide. In this experiment, we use a mirror-MOT [35] to trap atoms from background vapour directly above the surface, then transfer to the microtraps using macroscopic wires located beneath the surface.

Once atoms are held in the microscopic traps, it is possible to split the clouds [44, 45] and to transport them across the surface of the chip [46, 47]. The high density available in the traps permits rapid cooling by evaporation, down to temperatures where the cloud can Bose condense [48, 42, 36].

1.3 Overview of the experiment

This section aims to familiarize the reader with the principles of the experiment and to describe a typical experimental sequence.

The atom chip presented in this thesis is based on a permanently magnetized videotape surface. The videotape is recorded with a sine wave of wavelength $\lambda_M \sim 100\,\mu$m, using custom-built recording equipment. The magnetic field above the videotape has a strength B_1 of 215 G at the surface, and decays exponentially with a characteristic length scale of $\lambda_M/2\pi$. An array of microscopic guide potentials is formed by applying a uniform bias field B_{bias}, as shown in Figure 1.1: the distance, y_0, of the array from the surface is given by:

$$y_0 = \frac{\lambda_M}{2\pi} \ln\left(\frac{B_1}{B_{bias}}\right), \tag{1.1}$$

while the gradient of the trapping field is given by $2\pi\, B_{bias}/\lambda_M$. With no further modification, these potentials are simply 'guides'. By adding a confining potential along the axis, atoms can be magnetically trapped in all three dimensions.

We have developed an atom chip incorporating the magnetized videotape and a series of current-carrying wires located below the magnetized surface. One of these wires is used to form a macroscopic 'wire and bias field' guide, which is used to load atoms into the microscopic array. A pair of parallel wires generates a confining field along the axis of the guides, and a further pair is used as a radio-frequency (rf) antenna for evaporative cooling. The magnetized videotape is 12.5 mm × 22 mm and is attached to a glass substrate of thickness 150 μm and area 22 mm × 22 mm. The surface is gold coated so that it is optically reflective. The atom chip is positioned, magnetized surface lowermost, at the centre of the vacuum chamber. Ultra-high vacuum is necessary to minimize atom loss due to collisions with background gases.

The experimental sequence used to load the atoms into the traps can be described by the following steps:

- 5×10^7 rubidium atoms (^{87}Rb) are collected and cooled above the atom chip surface in a mirror-MOT. The mirror-MOT [35], illustrated in Figure 1.2 is a variation of the standard six-beam MOT and is implemented by reflecting two of the 780 nm laser beams off the atom chip surface at 45°. To make the surface reflective, the videotape is evaporatively coated with a thin ($\sim$100 nm) layer of gold. A magnetic quadrupole field is generated at the intersection of the laser beams by a pair of anti-Helmholtz coils outside the vacuum chamber.

- The mirror-MOT is compressed in two directions so that its shape becomes cylindrical and the atom number density increases. This is achieved, as shown

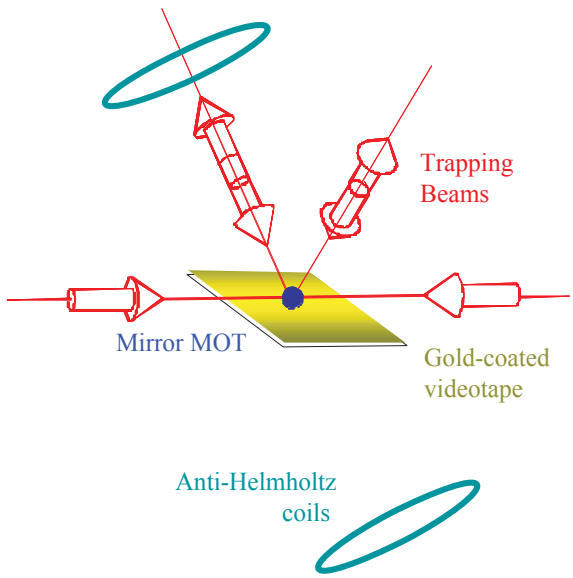

Figure 1.2 *The mirror-MOT: four laser beams, two of which are reflected by the atom chip surface, intersect at the centre of a magnetic quadrupole field. The latter is formed by the two anti-Helmholtz coils, which are located outside of the vacuum chamber.*

in Figure 1.3, using a uniform bias field, B_{bias} and a single wire carrying a current I_{centre}, located below the surface of the atom chip. This 'centre' wire is oriented parallel with the microtraps of the videotape. The field due to the current in the wire is cancelled at a given height by the applied bias field, to form a line of zero magnetic field above the surface, parallel to the wire. This magnetic potential is a two-dimensional quadrupole field, as illustrated in the inset of Figure 1.3. For the correct orientation of current and bias field, the field lines around this 2D quadrupole match those of the mirror-MOT quadrupole field. Superimposing the 2D quadrupole field with the 3D mirror-MOT field has the effect of compressing the MOT radially, so that it becomes tube shaped. Atoms are cooled in this compressed MOT (CMOT) to a temperature of 50 μK. Optimization of the CMOT will be discussed in Section 5.2.

- Atoms are transferred from the compressed MOT to a magnetic trap. This magnetic trap (the 'wire trap') is formed by the centre wire and bias field as described in the previous step. The contours of the magnetic trap are shown in Figure 1.3. Like the videotape microtraps, the magnetic potential formed by the wire current and bias field is simply a 2D guide. The ends of the guide are

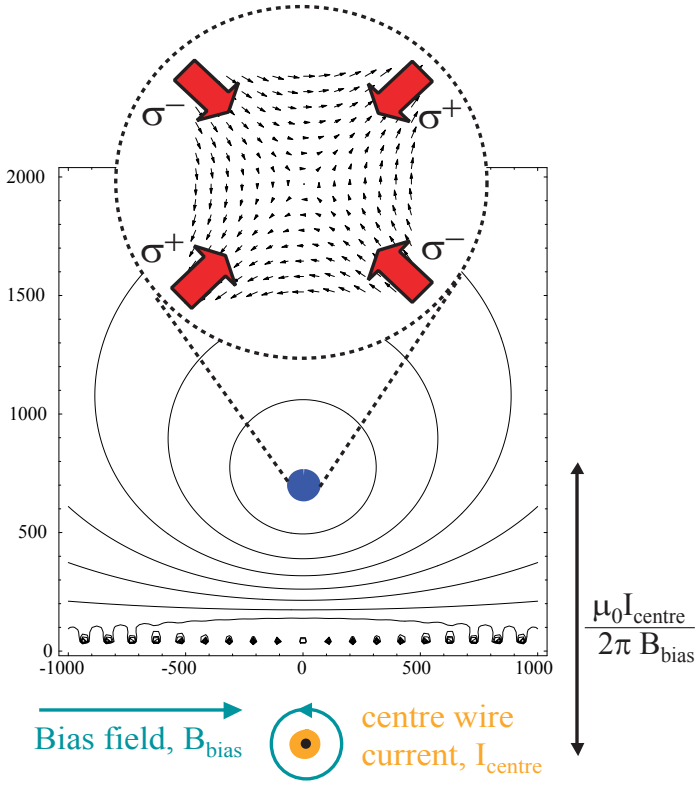

Figure 1.3 *Magnetic field due to the centre wire and bias field. For the current and bias field indicated at the bottom of the figure, a line of magnetic field zero is formed above the wire, as indicated by the closed contours. The inset shows the orientation of the magnetic field lines about this zero. This field is a 2D quadrupole: the cross-section of this field matches the mirror-MOT quadrupole field, formed by the anti-Helmholtz coils. The red arrows indicate the laser beams in the 2D plane, with helicities as labelled. The axes are labelled in microns.*

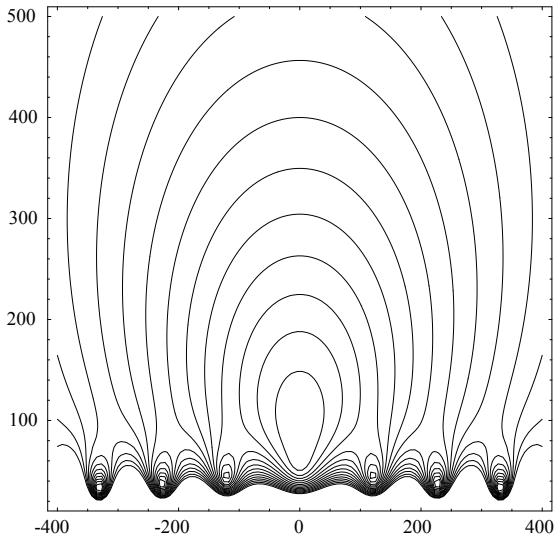

Figure 1.4 *Compression of the atom cloud into the microtraps. The bias field has been increased to a value where the magnetic trap formed above the centre wire merges with one of the videotape microtraps. The axes are labelled in microns.*

closed by two auxiliary current-carrying wires as will be discussed in Section 2.3.4

- The atoms are compressed into the videotape microtraps. Increasing the bias field and reducing the centre wire current shifts the wire trap towards the surface of the atom chip. At the same time, the radial field gradient of the trap increases, compressing the atom cloud to a smaller volume. Once the trap reaches a distance of about 80 μm from the surface, the magnetic field of the videotape begins to dominate and the wire trap merges with the microtrap array of the videotape. Figure 1.4 shows the magnetic field contours of the wire trap at a height above the surface where it is about to merge with a microtrap.

Once the atom cloud is magnetically trapped, it can be cooled by rf evaporation, as described in Section 6.10. A pair of parallel wires forms a current loop which serves as an antenna for the rf magnetic field.

Data is collected in the form of digital images by absorption imaging onto a CCD camera. The imaging technique is discussed in Section 4.4.

1.4 Organization of this thesis

Chapter 2 outlines the background theory necessary to understand this thesis. The principles of laser cooling, magneto-optical trapping and magnetic trapping are described. The trapping potentials are then derived for the wire trap and videotape microtraps. Chapter 3 describes the construction and characterization of the atom chip. The experimental set-up, comprising the laser system, vacuum chamber, rubidium source, imaging system and auxiliary equipment is described in Chapter 4. The experimental procedures for cooling atoms and loading the magnetic traps are presented in Chapters 5 and 6. Chapter 5 discusses the preparation of laser-cooled atoms in a mirror-MOT and Compressed-MOT, together with the findings of the initial experiments to load atoms into the microtraps using MOT forces. The work on magnetic trapping of atoms above the surface is contained in Chapter 6. The main results of this thesis, namely lifetime measurements of atom clouds when brought close to the surface, are presented here. A summary and concluding remarks are given in Chapter 7.

Chapter 2

Theoretical Basics

In the first part of this chapter, the basic theory of laser cooling techniques is described, with reference to ^{87}Rb. Laser cooling was first proposed in 1975 [49, 50]. The first slowed atomic beam was produced using this technique in 1982 [51], followed swiftly by development of three-dimensional optical molasses and the magneto-optical trap (MOT) [52, 53, 54]. The recent idea of the mirror-MOT [35] is crucial to this experiment — this technique enables atoms to be collected in a magneto-optical trap close to the surface of the atom chip. In the second part of this chapter, the principles of magnetic trapping are briefly discussed. In the final section, the trapping potentials above the atom chip are derived and discussed. The sinusoidal magnetization pattern, used in conjunction with a bias field to generate two-dimensional microscopic trapping potentials, has been used extensively in this research group and elsewhere for the creation of magnetic atom-mirrors. The wire trap, used here as an intermediate loading stage for the microtraps, was first used to confine atoms by [55]. Miniaturization of this type of trap, by microfabrication of wires on substrates, has formed the basis of several atom chip guiding experiments [32, 33, 17, 34, 35, 36]. The method for closing the ends of these tube-like potentials using an axial potential is presented, followed by a summary of the overall trapping potential.

2.1 Laser cooling and trapping

2.1.1 Doppler cooling

Doppler cooling is a method of slowing atoms with laser light, based on the strong scattering force an atom experiences in a laser light field. The scattering process operates as a cycle of stimulated absorption and spontaneous emission events. Each

time an atom absorbs a photon from a laser beam, it gains a momentum $\hbar\mathbf{k}$ in the direction of the laser beam, where $\mathbf{k} = \frac{2\pi}{\lambda}\hat{\mathbf{k}}$ is the wavevector associated with light of wavelength λ. The time-average momentum gain of an atom due to spontaneous emission of photons is zero, since photons are emitted symmetrically. The time-averaged force on an atom, from a laser beam of intensity I and frequency ν_L, is therefore

$$\langle \mathbf{F} \rangle = \hbar\mathbf{k}R(I, \nu_L), \tag{2.1}$$

where $R(I, \nu_L)$ is the rate at which an atom absorbs and emits photons. If the laser beam is directed opposite to an atom's direction of motion, the atom will be slowed.

The scattering rate for a two-level atom in a laser beam of intensity I, which is effectively detuned by a frequency interval $\Delta_\nu = \frac{\Delta}{2\pi}$ from the atomic transition, is

$$R(I, \nu_L) = \frac{\Gamma}{2}\frac{I/I_{Sat}}{1 + I/I_{Sat} + (2\Delta/\Gamma)^2} = \frac{\Gamma}{2}\frac{I/I_{Sat}}{1 + I/I_{Sat} + (2\Delta_\nu/\Gamma_\nu)^2}, \tag{2.2}$$

where $\tau = 1/\Gamma$ is the excited state lifetime ($\tau = 26.24\,\text{ns}$ for the $5\text{P}_{3/2}$ level of Rb [56]), $\Gamma_\nu = \Gamma/2\pi$ is the natural linewidth ($\Gamma_\nu = 6.07\,\text{MHz}$ in Rb) and I_{Sat} is the saturation intensity of the transition:

$$I_{Sat} = \frac{I\Gamma^2}{2\Omega^2}. \tag{2.3}$$

In Equation 2.3, Ω is the Rabi frequency, which is related to the atoms's dipole moment. For the specific case of a two-level system, Γ and Δ can be related through the dipole moment, and Equation 2.3 reduces to:

$$I_{Sat} = \frac{\pi hc\Gamma}{3\lambda^3}. \tag{2.4}$$

The key to Doppler cooling is that the scattering rate of an atom depends strongly on the atom's velocity, $\mathbf{v}$, via Δ, the effective detuning. The Doppler shift, $\mathbf{k}\cdot\mathbf{v}$, changes the effective laser frequency in the frame of a moving atom. Hence the effective detuning is

$$\Delta = 2\pi(\nu_L - \nu_0) - \mathbf{k}\cdot\mathbf{v}, \tag{2.5}$$

where ν_L is the laser frequency, ν_0 is the atomic transition frequency in zero magnetic field and $\mathbf{k}\cdot\mathbf{v}$ is the first order Doppler shift.

In one dimension, laser cooling is achieved by a pair of counter-propagating laser beams, each red-detuned ($\nu_L < \nu_0$) from the atomic transition frequency. In the frame of a moving atom, the beams are Doppler-shifted toward and away from resonance, such that the atom preferentially absorbs photons from the beam which opposes its direction of motion.

The 1D time-averaged force on a two-level atom positioned in this counter-propagating pair of beams (with $B = 0$) is

$$\langle F_x \rangle = \frac{\hbar k_x \Gamma}{2} \left(\frac{I/I_{Sat}}{1 + 2I/I_{Sat} + \left(\frac{2(\nu_L - \nu_0 - v_x/\lambda)}{\Gamma_\nu}\right)^2} - \frac{I/I_{Sat}}{1 + 2I/I_{Sat} + \left(\frac{2(\nu_L - \nu_0 + v_x/\lambda)}{\Gamma_\nu}\right)^2} \right), \tag{2.6}$$

which has the Taylor expansion

$$\langle F_x \rangle = \frac{8\hbar k_x^2 (\nu_L - \nu_0)}{\Gamma_\nu} \frac{I/I_{Sat}}{\left(1 + 2I/I_{Sat} + (2(\nu_L - \nu_0)/\Gamma_\nu)^2\right)^2} v_x = -\alpha\, v_x \tag{2.7}$$

for red-detuned light. That is, the total scattering force damps the motion of the atom. (For blue-detuned light, the effect is to accelerate the atoms.)

This cooling scheme can be extended to three dimensions: the standard scheme is to use three pairs of orthogonal, counter-propagating, red-detuned laser beams. 3D Doppler cooling is known as *optical molasses*, due to the nature of the damping force.

It is appropriate in most cases to assign a temperature to the width of the velocity distribution of a cloud of laser-cooled atoms, since the velocity distribution is generally Maxwellian. An effective temperature T, for an n-dimensional trap, is defined by taking the thermal energy to be $\frac{1}{2}k_B T$ per degree of freedom:

$$\frac{n}{2} k_B T = \sum_{i=1}^{n} \frac{m}{2} v_i^2, \tag{2.8}$$

where v_i is the r.m.s. velocity in the ith direction. The theoretical minimum temperature achievable by Doppler cooling is reached when the rate of removal of kinetic energy by the damping force is balanced by the heating rate due to the random nature of the absorption and emission of photons [57]. An atom at rest has an equal probability of absorbing a photon from any the laser beams. Each cycle of absorption and emission represents two random-walk steps of size $\hbar k$ in momentum space: after N such steps, the r.m.s. momentum grows as $\sqrt{N}\,\hbar k$. This leads to the Doppler temperature:

$$T_D = \frac{\hbar \Gamma}{4 k_B} \frac{1 + I/I_{Sat} + (2\Delta/\Gamma)^2}{-2\Delta/\Gamma}, \tag{2.9}$$

which has a minimum for low intensity of $T_D = \hbar\Gamma/2k_B$ at $\Delta = -\Gamma/2$. For rubidium, this temperature is $T_D = 145\,\mu$K.

2.1.2 Magneto-optical trapping

Magneto-optical traps (MOTs) combine the velocity dependent force of optical molasses with a spatially dependent force, achieved by applying a spatially varying magnetic field, $\mathbf{B}$, in the trapping region. The Zeeman interaction, $-\boldsymbol{\mu} \cdot \mathbf{B}$, of the atomic magnetic dipole moment, $\boldsymbol{\mu}$, with the local magnetic field, shifts the atomic energy levels, thereby modifying the atomic transition frequency. The effective laser detuning becomes:

$$\Delta = 2\pi(\nu_L - \nu_0) - \mathbf{k}.\mathbf{v} - \frac{\mu_B B}{\hbar}(m_e g_e - m_g g_g), \tag{2.10}$$

where $\frac{\mu_B B}{\hbar}(m_e g_e - m_g g_g)$ is the linear Zeeman shift. m_g, m_e, g_g, g_e are the respective magnetic quantum numbers, m_F, and Landé factors, g_F, of the ground and excited state. A quadrupole magnetic field increases linearly in strength from the centre of the trap. This field tunes the scattering rate as a function of position, producing a confining force directed towards the centre. In this way, it is possible to trap and cool atoms simultaneously.

The usual MOT scheme is shown in Figure 2.1(a) (not to scale). A quadrupole magnetic field of gradient b, $\mathbf{B} = b(x_{MOT}, -y_{MOT}/2, -z_{MOT}/2)$ is generated by a pair of anti-Helmholtz coils and oriented such that the field vectors are parallel with the laser beam directions. The MOT system is complex, since the scattering rate from each laser beam depends not only on the energy shifts of the magnetic sublevels, but also on the relative transition rates between different sublevels and hence on the polarization of the light field relative to the local magnetic field. The simplest 1D model of the MOT, illustrated in Figure 2.1(b), uses a transition between the two hyperfine levels: $|F, m_F\rangle = |0, 0\rangle \rightarrow |F', m'_F\rangle = |1, -1\rangle, |1, 0\rangle, |1, +1\rangle$, where m_F is the projection of the total atomic angular momentum, F, onto the quantization axis. The magnitude of the field increases linearly from the centre, thus the hyperfine levels are split into sublevels $|F, m_F\rangle$ whose energy shifts vary linearly with the field: $\Delta E(m_F) = \mu_B g_F m_F B = \mu_B g_F m_F b x_{MOT}$ for small B. Transitions between these sublevels must obey the following selection rules: $\Delta m_F = +1$ for σ^+ light (right-hand circularly polarized with respect to $\mathbf{B}$); $\Delta m_F = -1$ for σ^- light (left-hand circularly polarized with respect to $\mathbf{B}$); $\Delta m_F = 0$ for π light (linearly polarized parallel to $\mathbf{B}$).

The $|F, m_F\rangle = |0, 0\rangle \rightarrow |F', m'_F\rangle = |1, -1\rangle$ transition is tuned increasingly towards the red-detuned laser frequency as the magnetic field increases. Therefore, if all polarizations of laser light are present, atoms will preferentially absorb σ^- photons as they move away from the trap centre. If the laser beams are both circularly polarized as in Figure 2.1(a), such that they are σ^- with respect to the magnetic

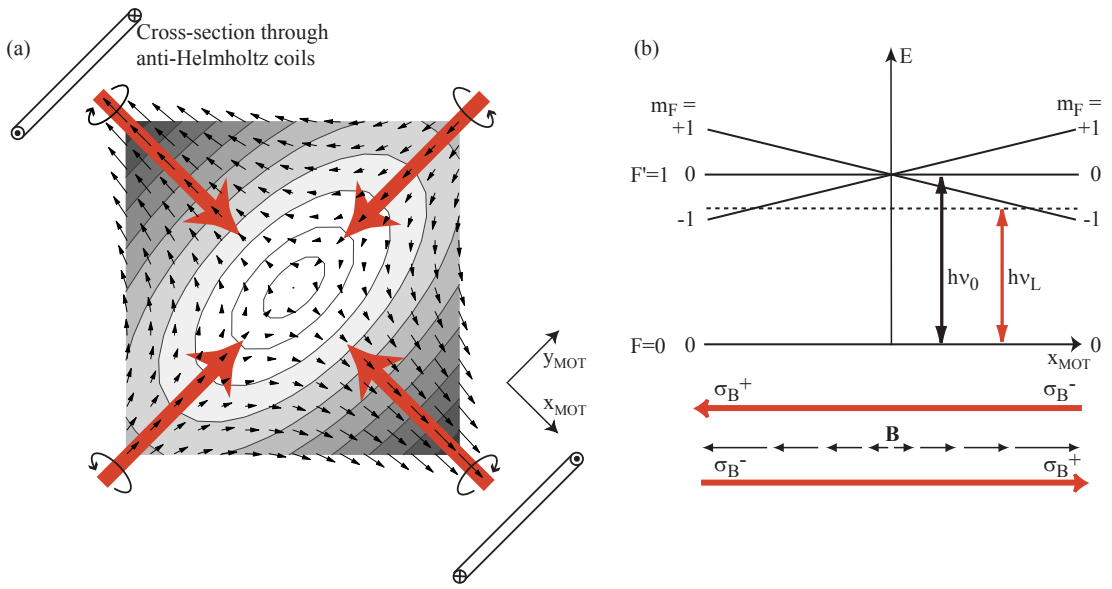

Figure 2.1 *(a) The laser beams, magnetic field coils and quadrupole field configuration of a six-beam MOT: the magnetic field strength and direction are indicated by the contours and small arrows; the red arrows represent the laser beams, with helicities as indicated. Only four of the six beams are shown: there is a third pair (not shown), orthogonal to the page. Relative to the laser beam wavevectors, the laser beams which pass through the anti-Helmholtz coils have opposite helicity from the other beams. (b) One-dimensional MOT energy level scheme: the magnetic field and laser beam polarizations (relative to the local magnetic field direction) are indicated at the bottom of the figure.*

field vector as they approach the centre and σ^+ as they leave (Figure 2.1(b)), an atom at $|x| > 0$ will scatter most photons from the beam directed towards the centre of the trap. The force on an atom close to the MOT centre is derived in the same way as Equation 2.7, giving

$$\langle F \rangle = -\alpha v - \kappa |x|, \tag{2.11}$$

where $\kappa \propto \alpha b$ is defined as the spring constant of the trap. Again, this set-up is simply extended to three dimensions: the required polarizations are obtained by fixing each laser beam polarization as indicated in Figure 2.1(a). Note that the field gradient along the axis of the field coils is necessarily twice the field gradient along the other two axes: a consequence of $\nabla \cdot \mathbf{B} = 0$.

In this experiment, rubidium is collected in the MOT from an uncooled vapour. Only atoms moving slower than the 'capture velocity' of the MOT will be slowed and trapped: typical capture velocities [58] are calculated to be of the order of $20\,\mathrm{ms}^{-1}$ for the parameters of this experiment, corresponding to a small (but significant)

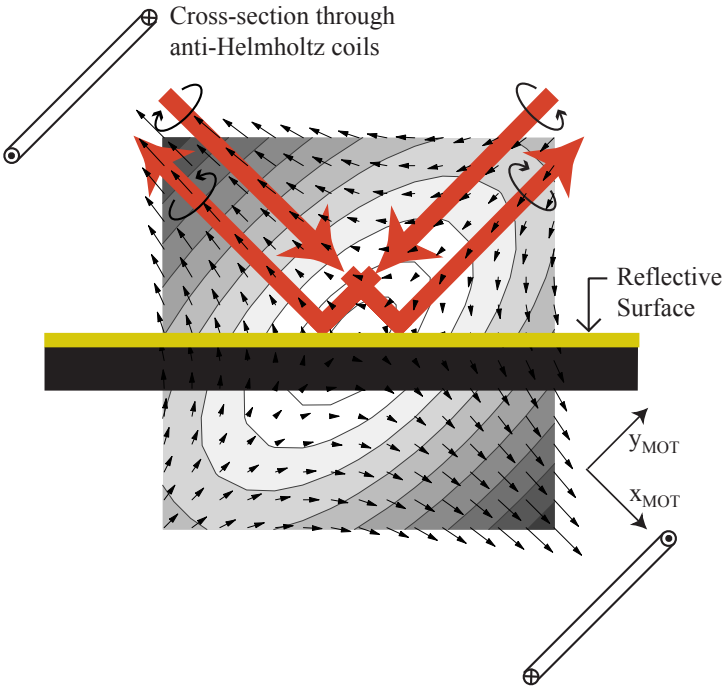

Figure 2.2 *Schematic of the four-beam mirror-MOT. There is a further pair of beams (not shown), orthogonal to the page, as in Figure 2.1. The two beams shown are reflected to realize the six-beam MOT configuration in the half-space above the reflective surface. The helicities of the beams are indicated, before and after reflection.*

fraction of the Boltzmann distribution.

2.1.3 The mirror-MOT

The main goal of this experiment is to bring cold atoms close to a magnetized surface. The development of the *mirror-MOT* [35] is an important stepping-stone towards this. Using a conventional six-beam MOT as described above, it is impossible to bring a surface into the trapping region without it obstructing the laser beams. The mirror-MOT overcomes this by having a reflecting surface situated at the mid-plane of the quadrupole field, as shown in Figure 2.2. Only four beams are used, two of which are reflected off the mirror surface at 45°. This automatically generates the correct polarizations for the reflected beams, since a circularly polarized beam undergoes a reversal of helicity on reflection, with respect to its direction of propagation. The usual MOT geometry is therefore realized in the half-space above the mirror.

2.1.4 Sub-Doppler cooling

One of the exciting discoveries of optical molasses experiments was that the temperature attained was nearly six times lower than that predicted by Doppler cooling theory [54]. This showed that there is an additional cooling mechanism, which operates in low magnetic fields ($B < 100\,\mathrm{mG}$) and with optimum detuning greater than that predicted by Doppler theory. The extra cooling mechanism relies on the spatial variation of the polarization of the light field in optical molasses, so is known as *polarization gradient cooling*. A detailed treatment is given in [59]. The most commonly cited polarization gradient cooling mechanism is known as *Sisyphus cooling*. Consider a one-dimensional standing wave generated by two linearly polarized beams with orthogonal polarization axes: the polarization along this standing wave varies from σ^+ to σ^- and back with a wavelength $\lambda/2$. This causes spatial variations in the light shifts experienced in the ground states. The light shift depends on the Clebsch-Gordan coefficient for the transition coupled by the polarization and is negative for red-detuned light. Hence the largest AC Stark shifts are experienced by the $m_F = \pm F$ sub-levels, for $\sigma^\pm$ polarized light respectively. At points where the polarization is purely σ^+ (σ^-), the atoms are optically pumped towards the $m_F = +F$ ($m_F = -F$) sub-level, which has the largest negative light shift for this σ^+ (σ^-) polarization. In this way, each time an atom moves away from a potential minimum, it is driven by optical pumping to a state with a lower energy. Atoms thereby lose potential energy and are cooled. Because the light shifts are relatively small, this mechanism works only for atoms travelling at quite low velocities. In optical molasses, atoms are pre-cooled by the Doppler mechanism before these processes come in to effect.

The case of a one-dimensional standing wave generated by two circularly polarized beams, with opposite handedness of polarization, can be considered as follows: the resultant standing-wave is linearly polarized at all points, but the electric field vector rotates by 2π every wavelength. In this case the light field does not give rise to any spatial variation in the light shift of the atomic ground state sub-levels: an atomic population at rest in the light field has a symmetric population distribution of ground state sub-levels due to optical pumping processes. However, if an atom has some velocity along the axis of the light field, it interacts with a rotating linear polarization. The optical pumping process is not instantaneous and so the population lags behind the rotation of the polarization. In a new basis defined by the local axis of polarization, this is represented by an asymmetric mixing of the groundstate m_F levels, which occurs in such a way as to promote preferential absorption from the beam towards which the atom moves, hence slowing the atom further. This

process is essentially no different from the Sisyphus cooling mechanism described above: both are motion-induced orientation effects, in that the atomic population always lags behind the spatially varying polarization.

To determine the equilibrium temperature, one considers once again the balance between cooling due to the damping force and heating due to momentum diffusion. At detunings $\Delta > \Gamma$, the latter can be dominated by fluctuations in the instantaneous dipole force rather than the spontaneous emission of photons, for many positions within the standing wave. This yields an equilibrium temperature which is proportional to intensity and inversely proportional to detuning of the trapping beams, as observed experimentally [54]. The limit on the lowest theoretically achievable temperature by sub-Doppler cooling is that corresponding to the recoil of one photon. This is given by

$$T_{recoil} = \frac{\hbar^2 k^2}{k_B m}, \tag{2.12}$$

which, for ^{87}Rb, corresponds to $0.4\,\mu$K. Typically, the lowest temperature obtained in optical molasses experiments is around $10\,T_{recoil}$

Polarization gradient cooling mechanisms occur in MOTs, but only in regions of small magnetic field [60]. Drewsen *et al* [61] have shown experimentally that the temperature in a caesium MOT, containing between 10^5 and 10^8 atoms, has a strong dependence on atom number N, obeying the empirical equation:

$$T \propto N^{1/3}\frac{\Omega}{\Delta}, \tag{2.13}$$

for field gradients of up to $12\,\mathrm{G\,cm^{-3}}$, where $\Omega = \Gamma\sqrt{I/2I_{Sat}}$ is the Rabi frequency per beam. Even for an atom number of 10^8, temperatures well below the Doppler limit are obtained. In the limit of low atom number, the temperature of a MOT is identical to that of 3D sub-Doppler optical molasses.

2.1.5 Trapping Rubidium

The experiments described in this thesis were performed using the ^{87}Rb isotope. Alkali atoms are used in many laser cooling experiments due to their advantageous atomic structure. Doppler and sub-Doppler cooling generally work well for alkali atoms, due to their large hyperfine energy splittings. This allows for large laser detunings from a given transition, without driving transitions to a different level. In addition, the optical transitions in Rb are located in the infra-red region and can be driven using inexpensive diode lasers. The optical transitions in rubidium are shown in Figure 2.3.

The transition used for cooling and trapping ^{87}Rb is the D2 transition (780.25 nm in vacuum) between the ground state $5S_{1/2}$ and the excited state $5P_{3/2}$. ^{87}Rb has

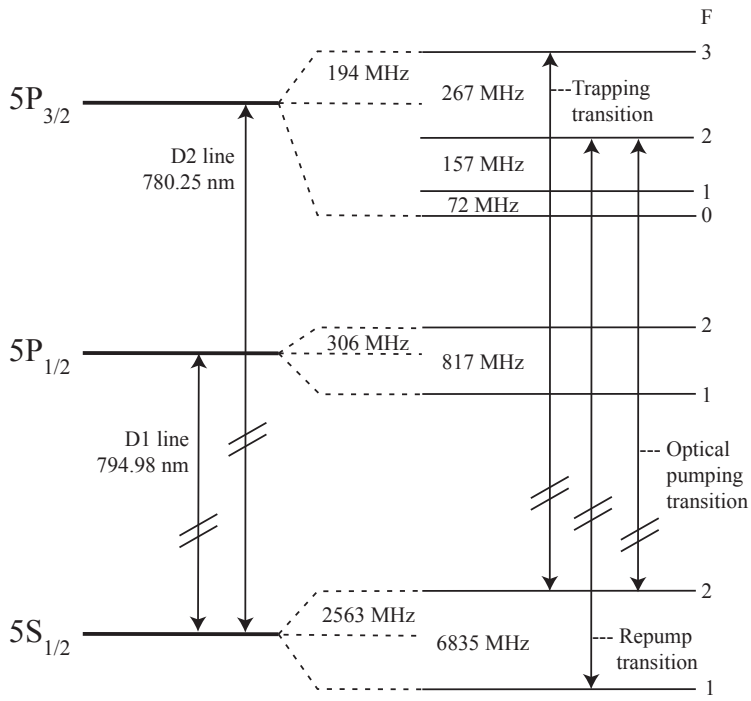

Figure 2.3 *Energy levels of* ^{87}*Rb. (Atomic data sources: [62, 63].)*

nuclear spin $I = 3/2$, giving rise to the hyperfine levels shown in Figure 2.3 . Ideally a MOT should operate on a closed transition. In Rb, the MOT beams are tuned to the $F = 2 \rightarrow F' = 3$ transition. From the $F' = 3$ level, an atom can decay only back to the $F = 2$ level, due the selection rule $\Delta F = 0, \pm 1$. However, off-resonant excitation of the $F' = 2$ level also occurs, particularly if the trapping beams are far-detuned, from which 3/8 of the population decays to $F = 1$. Once in this state, the atoms are no longer excited by the trapping light as the 6.8 GHz hyperfine splitting of the ground state is much greater than the 6.07 MHz natural linewidth of the trapping transition. Given a MOT detuning of 15 MHz, the probability of exciting an atom to the $F' = 2$ state followed by decay to $F = 1$ is approximately 1:500. With only trapping light, all the atoms would quickly accumulate in the lower hyperfine level of the ground state and be lost from the trap. The $F = 2$ level of the ground state is therefore repopulated using *repump* laser light, overlapped with the trapping beams and tuned to the $F = 1 \rightarrow F' = 2$ transition.

The stretched state transition $5S_{1/2}\,|F, m_F\rangle = |2, 2\rangle \rightarrow 5P_{3/2}\,|F, m_F\rangle = |3, 3\rangle$ is a closed transition and has a saturation intensity of $1.65\,\mathrm{mWcm^{-2}}$, using Equation 2.4. This is the saturation intensity used throughout this thesis. The Clebsch-Gordan coefficients for the D2 transition are tabulated in Appendix A.

2.2 Magnetic Trapping

2.2.1 Atom–magnetic field interactions of ^{87}Rb

Atoms interact with magnetic fields via their magnetic moment, $\boldsymbol{\mu}$. The Hamiltonian describing the ground state of an alkali metal atom is:

$$\hat{H} = \frac{A}{I+\frac{1}{2}}\mathbf{I}.\mathbf{J} - \boldsymbol{\mu}.\mathbf{B}, \tag{2.14}$$

where the atomic state is given in the basis of the total electronic ($\mathbf{J}$) and nuclear ($\mathbf{I}$) angular momentum states $|J, m_J; I, m_I\rangle$. The first term is the hyperfine interaction, where A is the hyperfine splitting — in the case of ^{87}Rb, between the two ground state levels, $F = 1$ and $F = 2$, for which $A/h = 6385\,\text{MHz}$. The second term is the Zeeman interaction between the atomic magnetic moment, $\boldsymbol{\mu}$ and the external applied magnetic field, $\mathbf{B}$. Both the electronic and nuclear magnetic moments contribute to the atomic magnetic moment:

$$\begin{aligned}\boldsymbol{\mu} &= -g_J\mu_B\mathbf{J} - g_I\mu_N\mathbf{I} \\ &= -g_J\mu_B\mathbf{J} + g_I'\mu_B\mathbf{I},\end{aligned} \tag{2.15}$$

where g_J and g_I are the Landé g-factors for the total electronic and nuclear angular momentum respectively. For ^{87}Rb, $g_I = 1.353$, $g_I' = 0.995 \times 10^{-3}$ and $I = 3/2$. In the approximation where $g_s \approx 2$, the g_J factors are given by:

$$g_J = \frac{3J(J+1) - L(L+1) + S(S+1)}{2J(J+1)}. \tag{2.16}$$

For the $5S_{1/2}$ ground state of the D2 transition, g_J=2; for the $5P_{3/2}$ state, $g_J = 4/3$.

For the special case of zero orbital angular momentum ($\mathbf{L} = 0$, $\mathbf{J} = \frac{1}{2}$), the energies, E, of the magnetic sublevels are given by the Breit-Rabi formula [64]:

$$E = -\frac{hA}{2(2I+1)} + (-1)^F\frac{hA}{2}\sqrt{1 + \frac{2m_F}{I+\frac{1}{2}}x + x^2}, \tag{2.17}$$

$$\text{where} \qquad x = \frac{(g_I + g_S)\mu_B B}{hA}.$$

Figure 2.4 shows the Breit-Rabi diagram for ^{87}Rb. The state labels, $|F, m_F\rangle$, are appropriate to the limit of low magnetic field. In this limit, the Hamiltonian of the ground state is approximately diagonal in the basis of the total angular momentum operator, $\mathbf{F} = \mathbf{J} + \mathbf{I}$. The Zeeman interaction lifts the degeneracy in m_F and the resulting energy shift, $\Delta E(m_F)$, is proportional to the applied magnetic field strength, B:

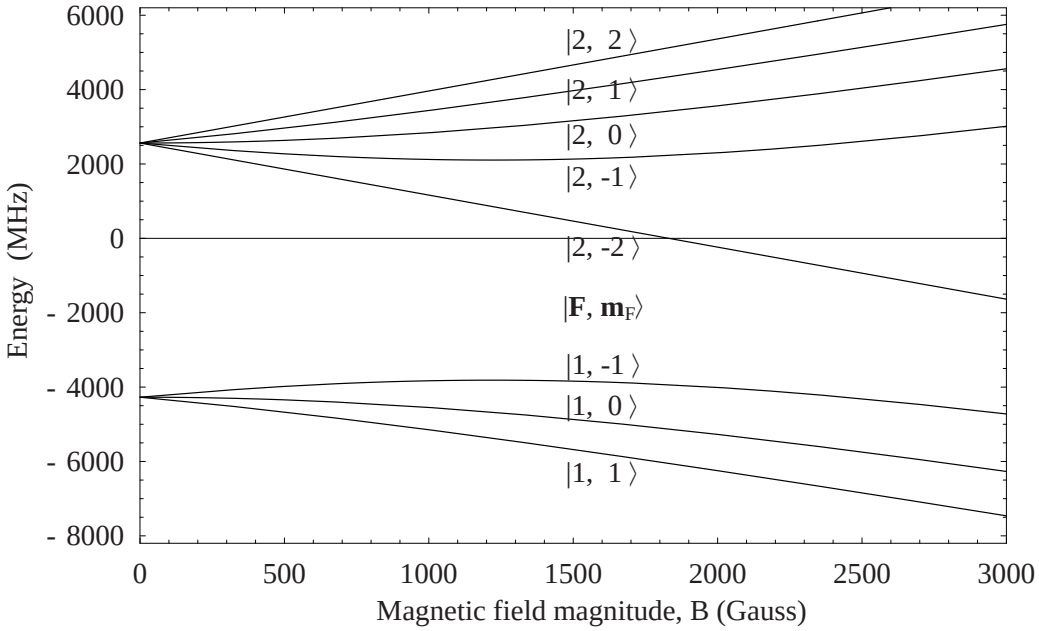

Figure 2.4 *Groundstate Breit-Rabi diagram for ^{87}Rb. The $|F, m_F\rangle$ labels are appropriate to the states in the weak-field limit (Hamiltonian diagonal in the $|F, m_F\rangle$ basis).*

$$\Delta E(m_F) = \mu_B g_F m_F B \qquad (B < 300\,\mathrm{G}) \tag{2.18}$$

where

$$g_F = \frac{g_J(F(F+1) + J(J+1) - I(I+1)) + \frac{\mu_N}{\mu_B} g_I(F(F+1) - J(J+1) + I(I+1))}{2F(F+1)} \tag{2.19}$$

Since $\mu_N \ll \mu_B$, the g_F values in the two ground states, $|F = I \pm 1/2, m_F\rangle$, are:

$$\begin{aligned} g_F &= \frac{\pm 2}{2I+1} \\ &= \pm 1/2 \qquad \text{in } ^{87}\text{Rb.} \end{aligned} \tag{2.20}$$

Hence, the energy shifts are inverted with respect to m_F for the lower ($F = 1$) hyperfine level.

2.2.2 Magnetic trapping and the adiabatic condition

The orientation of the magnetic moment of an atom relative to the applied magnetic field is quantized [1]. Once an atom is polarized in a particular Zeeman sub-level,

it is driven by the Stern-Gerlach force,

$$\mathbf{F} = -\nabla E = -g_F m_F \mu_B \nabla B \tag{2.21}$$

towards either high or low magnetic field. Atoms for which $g_F m_F > 0$ are attracted to regions of low magnetic field and can thus be trapped in a minimum of the magnetic field. In the weak field limit, the 'low-field seeking' Zeeman sub-levels are $|F, m_F\rangle = |2,2\rangle, |2,1\rangle, |2,0\rangle, |1,-1\rangle$. From Equation 2.21 we see that the highest m_F states are trapped most strongly, hence in these experiments, clouds of atoms are prepared in the $|F, m_F\rangle = |2,2\rangle$ state by optical pumping (Section 6.1) before magnetic trapping.

It is not possible to generate a magnetic field maximum using static fields. However, high-field seeking states have been trapped using time-varying magnetic fields in an AC trap, such as [65]. Such traps have the advantage that atoms can be trapped in the lowest energy state, thus minimizing hyperfine changing atomic collisions, but typical trap depths are only of the order of a few Gauss.

The above derivation of the Zeeman energy is only strictly valid for constant magnetic fields. In a magnetic trap, an atom experiences a spatially varying magnetic field. Equation 2.18 will remain valid only if the projection of the atomic magnetic moment, m_F, on the field direction is a constant of the motion. Quantum mechanically, this is to say that spin-flipping transitions between magnetic sublevels do not occur. If the atom moves slowly through the magnetic field, the magnetic moment will follow the field adiabatically. The atom–field interaction energy is then independent of the direction of the field and is dependent only on its magnitude, as in Equation 2.18. The condition to be fulfilled is the *adiabatic condition* [66].

For an atom moving with velocity $\mathbf{v} = (v_x, v_y, v_z)$ through a static magnetic field,

$$\frac{\mathrm{d}\mathbf{B}}{\mathrm{d}t} = \frac{\partial \mathbf{B}}{\partial x} v_x + \frac{\partial \mathbf{B}}{\partial y} v_y + \frac{\partial \mathbf{B}}{\partial z} v_z. \tag{2.22}$$

This can be decomposed into two components, one parallel and one orthogonal to $\mathbf{B}$:

$$\frac{\mathrm{d}\mathbf{B}}{\mathrm{d}t} = \omega_1 \mathbf{B} + \boldsymbol{\omega} \times \mathbf{B}, \tag{2.23}$$

where ω_1 and $\boldsymbol{\omega}$ have the dimensions of angular frequency and are given by

$$\omega_1 = \frac{\mathbf{B}}{B^2} \cdot \frac{\mathrm{d}\mathbf{B}}{\mathrm{d}t} \qquad \text{and} \qquad \boldsymbol{\omega} = \frac{\mathbf{B}}{B^2} \times \frac{\mathrm{d}\mathbf{B}}{\mathrm{d}t}$$

Here, ω_1 is the rate of change of magnitude of $\mathbf{B}$ along its direction and $\boldsymbol{\omega}$ is the rate of change of the direction of $\mathbf{B}$. In the classical picture, the atomic magnetic moment, $\boldsymbol{\mu}$, precesses about $\mathbf{B}$ with the instantaneous Larmor frequency, $\omega_0(t) =$

$-g_F m_F \mu_B B(t)/\hbar$. If the field direction changes slowly enough, the magnetic moment of the atom follows the direction of the magnetic field adiabatically and no transitions occur between spin states. The adiabatic condition is therefore expressed as:

$$|\omega(\mathbf{t})/\omega_0(t)| \ll 1$$

or

$$\left| \frac{\mathbf{B}}{B^2} \times \frac{\mathrm{d}\mathbf{B}}{\mathrm{d}t} \right| \ll \omega_0 \tag{2.24}$$

This condition can be derived in the context of quantum mechanics, by considering the evolution of any Hamiltonian quantum system [67]. In this case, the adiabatic condition has the same form, but with a more general interpretation of ω_0. It is the minimum value of the angular frequency of the different allowed transitions between the levels of the quantum system.

The adiabatic condition is generally fulfilled for cold atoms in magnetic traps, since their low velocity limits the rate of change of magnetic field experienced by any single atom. However, it clearly breaks down at points where $B = 0$ and spin-flipping transitions ('Majorana transitions' [68]) can occur. The magnetic traps of this thesis are designed such that there are no regions where $B = 0$. As will be seen in the following sections of this chapter, the trapping potentials are tube-like, with the magnetic field vectors all lying in the x–y plane. To remove regions of zero field along the axis of the trap, it is sufficient to simply add an orthogonal, axial (z) field. The adiabatic condition will be discussed in the context of the magnetic trapping potentials of the atom chip in Section 2.3.3.

2.3 Videotape microtraps and wire traps

2.3.1 Magnetic mirrors and microtraps

A magnetic mirror for cold neutrons based on a periodic array of current carrying wires was first proposed by Vladimirskii in 1961 [69]. As an extension of this idea, Opat *et al* [70] proposed a scheme for reflecting slowly moving atoms using periodic magnetic and electric structures. The first magnetic mirror for cold atoms was realized in this research group by Roach *et al* in 1995 [71]. As will be seen below, it is a simple extension to the magnetic mirror to create an array of magnetic microtraps above the surface by applying a uniform bias field. The mirror-like properties remain a useful diagnostic tool when optimizing and calibrating various parameters of the experiment.

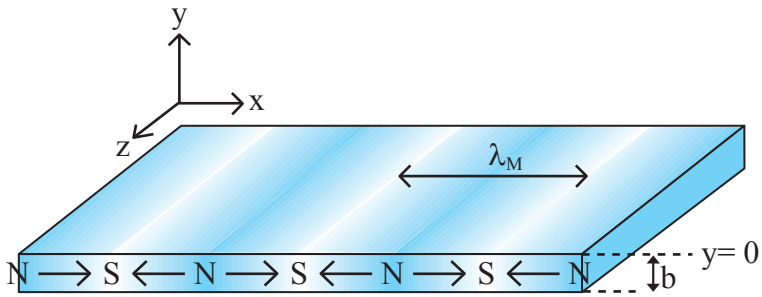

Figure 2.5 *Schematic of the videotape magnetization.*

The magnetic field above the videotape magnetic mirror

The magnetic mirror is a thin layer of magnetic material, of thickness b. It lies in the x–z plane, with $\hat{\mathbf{y}}$ being the outward, normal vector, as shown in Figure 2.5. It has a periodic, in-plane magnetization, $\mathbf{M}$, of wavelength λ_M. The mirror we use is recorded with a $\sim 100\,\mu$m sine wave[1]. The dimensions of the piece of recorded videotape (12.5 mm $\times$ 22 mm) are much greater than the recorded wavelength, so end effects are negligible and the magnetization can be treated as an infinite pattern.

Since there are no real currents, $\nabla\times\mathbf{H}$ and $\nabla\times\mathbf{B}$ are both zero everywhere above the mirror. The magnetic field configuration above the mirror can therefore be derived by considering a scalar magnetic potential [72], ϕ, such that the magnetic field, $\mathbf{B}$, is given by

$$\mathbf{B} = -\nabla\phi. \tag{2.25}$$

The periodic boundary conditions on $\mathbf{B}$ require that ϕ is similarly periodic in x and independent of z. ϕ must satisfy the Laplace equation, which reduces to 2D, given the independence in z:

$$\nabla^2\phi(x,y) = \frac{\partial^2\phi}{\partial x^2} + \frac{\partial^2\phi}{\partial x^2} = 0. \tag{2.26}$$

[1]Due to saturation during the recording process, (see Section 3.2.2), the magnetization of the mirror used for this work is more like a square wave than a sine wave.

Since ϕ is periodic, it can be expanded as a Fourier Series:

$$\phi(x,y) = \frac{1}{2}\sum_{n=0}^{\infty} \phi_n(y)\, e^{i(nkx+\delta_n)} + c.c. \tag{2.27}$$

where $$k = 2\pi/\lambda_M$$

and $$\phi_n(y) = \frac{k}{\pi}\int_0^{\lambda_M} \phi(x,y)\, e^{-i(nkx+\delta_n)}\, \mathrm{d}x \qquad (n \neq 0)$$

$$\phi_0(y) = \frac{k}{2\pi}\int_0^{\lambda_M} \phi(x,y)\, \mathrm{d}x \qquad (n = 0)$$

Substituting the Fourier expansion (2.27) into (2.26) yields a differential equation for the Fourier coefficients, ϕ_n:

$$\frac{\partial^2 \phi_n(y)}{\partial y^2} - n^2 k^2 \phi_n(y) = 0. \tag{2.28}$$

This has real solutions of the form $e^{\pm nky}$, of which only the decaying exponential is a physical solution, thus:

$$\phi_n(y) = \phi_n(0) e^{-nky}. \tag{2.29}$$

A periodic magnetization produces primarily a fundamental component, $n = 1$, plus higher harmonics, with amplitudes decreasing with n.[2] Equation 2.29 shows that each harmonic decays exponentially with distance from the surface: in particular, the higher the harmonic, the greater the decay rate. At distances greater than $\lambda_M/10$ ($\sim 10\,\mu$m) from the surface, only the fundamental Fourier component is significant, due to its slower exponential decay. (This assumes that a second harmonic term has not been deliberately introduced — on the grounds of symmetry, we expect only odd harmonics.) In this regime, Equation 2.27 becomes

$$\phi(x,y) = \frac{1}{2}\phi_1(0) e^{-ky} e^{i(kx+\delta_1)} + c.c.\,, \tag{2.30}$$

which leads to

$$B_x = -\frac{\partial \phi}{\partial x} = k e^{-ky} \phi_1(0) \sin(kx + \delta_1) \tag{2.31}$$

$$B_y = -\frac{\partial \phi}{\partial y} = k e^{-ky} \phi_1(0) \cos(kx + \delta_1), \tag{2.32}$$

where $\phi_1(0)$ and δ_1 are still to be determined.

[2] c.f. a square wave has Fourier components proportional to $\sum_{n=odd} \frac{e^{inkx}}{n}$.

To evaluate the coefficients $\phi_1(0)$ and phases δ_1, we need to relate the potential, ϕ, to the magnetization, $\mathbf{M}$, of the magnetic medium. The magnetization

$$\mathbf{M} = M_1 \cos(kx)\,\hat{\mathbf{x}} \tag{2.33}$$

can be replaced by fictitious surface currents [72], $\mathbf{K}$, per unit width, given by

$$\mathbf{K} = \mathbf{M} \times \hat{\mathbf{n}} = \pm M_1 \cos(kx)\,\hat{\mathbf{z}}, \tag{2.34}$$

where $\hat{\mathbf{n}}$ is the outer normal to the surface and the $\pm$ refers to the upper and lower surfaces of the magnetic layer respectively. This replaces the bulk magnetization by two sinusoidal current sheets of opposite sense, one on the upper surface of the magnetic layer (at $y = 0$) and one on the lower surface ($y = -b$). We can then apply Ampère's law to a loop enclosing a small section of the upper surface between x_A and x_B. For paths infinitesimally close to the upper surface (above or below), the exponential factor in Equation 2.31 has the value of unity. An Ampère loop enclosing the current between x_A and x_B gives

$$-2\int_{x_A}^{x_B} k\phi_1(0)\,\sin(kx+\delta)\,\mathrm{d}x = \mu_0 I_{enclosed} \tag{2.35}$$

$$= \mu_0 \int_{x_A}^{x_B} M_1 \cos(kx)\,\mathrm{d}x, \tag{2.36}$$

from which we deduce that δ is equal to $\pi/2$ and that $\phi_1(0)$ is related to the magnetization by

$$2k\phi_1(0) = -\mu_0 M_1. \tag{2.37}$$

Hence the field components above the upper current sheet are

$$\begin{pmatrix} B_x \\ B_y \end{pmatrix} = \frac{1}{2}\mu_0 M_1 e^{-ky} \begin{pmatrix} -\cos(kx) \\ +\sin(kx) \end{pmatrix}. \tag{2.38}$$

The lower current sheet has opposite sign and therefore produces a magnetic field with opposite sign. Thus when we add the contribution from the lower sheet in the plane $y = -b$, the total field above the surface at height y becomes

$$\begin{pmatrix} B_x \\ B_y \end{pmatrix} = \frac{1}{2}\mu_0 M_1 (1 - e^{-kb})\, e^{-ky} \begin{pmatrix} -\cos(kx) \\ +\sin(kx) \end{pmatrix}. \tag{2.39}$$

It should be noted that these equations can also be obtained by integration of Equation (5.100) of [72]:

$$\phi(x,y) = -\frac{\mu_0}{4\pi}\int_V \frac{\nabla' \cdot \mathbf{M}(\mathbf{r}')}{|\mathbf{r}-\mathbf{r}'|}\mathrm{d}^3r' + \frac{\mu_0}{4\pi}\oint_S \frac{\mathbf{n}' \cdot \mathbf{M}(\mathbf{r}')}{|\mathbf{r}-\mathbf{r}'|}\mathrm{d}^2r', \tag{2.40}$$

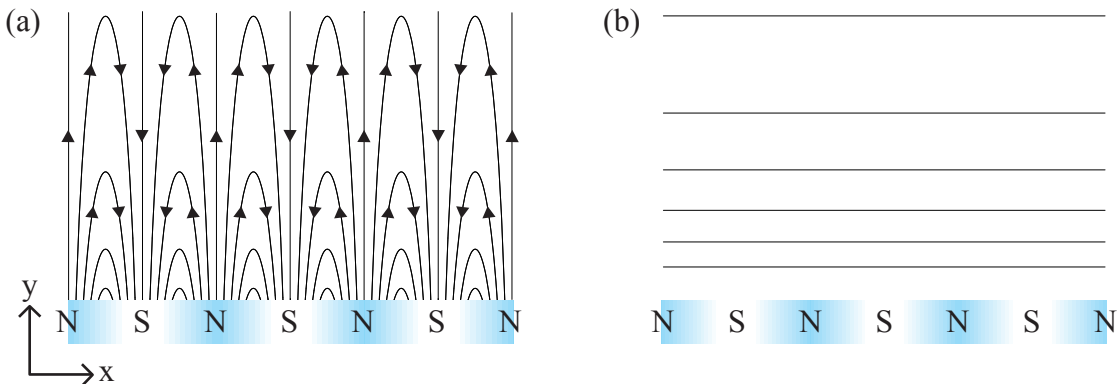

Figure 2.6 *(a) The magnetic field above the magnetic mirror; (b) Contours of constant magnetic field strength.*

which relates ϕ directly to the magnetization, for the specific case where $\mathbf{M}$ is periodic, parallel to x and independent of z and y (see [73] or [74]).

The direction of the magnetic field in Equation 2.39 rotates in the x–y plane with a cyclic pattern of field lines, as shown in Figure 2.6(a). However, the magnetic field magnitude, B, and thus the atom–magnetic field interaction energy, depends only on height y above the surface, as shown in Figure 2.6(b):

$$\begin{aligned} B &= \frac{1}{2}\mu_0 M_1 (1 - e^{-kb})\, e^{-ky} \\ &= B_1\, e^{-ky}. \end{aligned} \tag{2.41}$$

Consequently, the Stern-Gerlach force is everywhere normal to the magnetic surface and so this creates a specular atomic reflector.

B_1 is defined by Equation 2.41 as the field strength of the fundamental at the surface of the magnetic mirror:

$$B_1 = \frac{1}{2}\mu_0 M_1 (1 - e^{-kb}). \tag{2.42}$$

The factor $(1 - e^{-kb})$ can be understood as a 'finite-thickness' effect in which the opposing field from the lower current sheet partially cancels the upper one. As the magnetic layer becomes thicker, this factor rapidly saturates to a value of unity once the thickness b of the magnetic layer is larger than $1/k$. The maximum field outside the mirror is $\frac{1}{2}\mu_0 M_1$, half the remanent field that exists inside the material. The factor of one half is due to the symmetry in the magnetization, which causes half of the magnetic field lines to go up and half to go down.

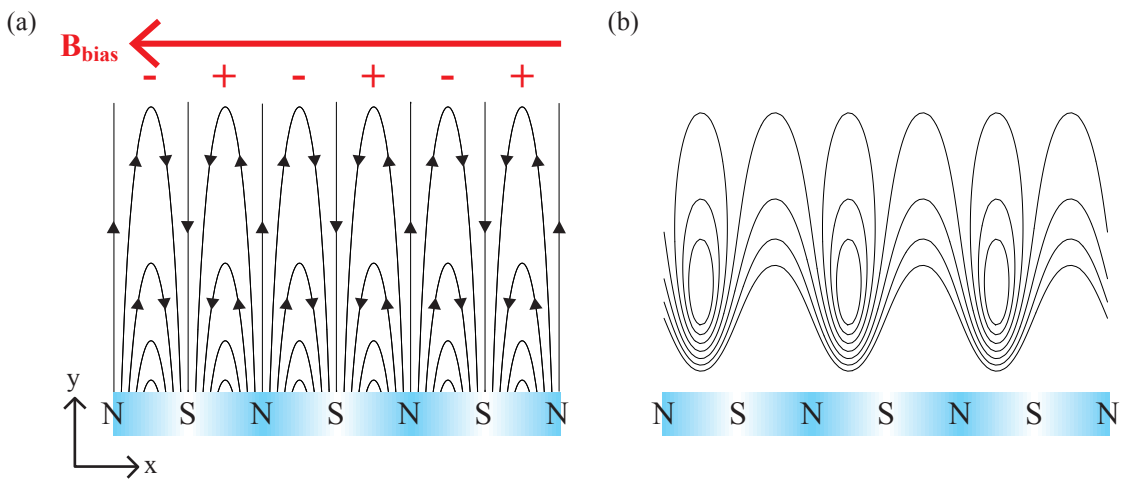

Figure 2.7 *(a) Addition of a uniform bias field to the field above the magnetic mirror; (b) the resulting magnetic potential. The closed contours indicate lines of minimum magnetic field: these extend along the z-axis as tube-like guides.*

Formation of magnetic microtraps

The magnetic microtraps are created by adding a bias field, $\mathbf{B_{bias}} = -B_{bias}\,\hat{\mathbf{x}}$, to the field of the magnetic mirror, such that

$$\begin{pmatrix} B_x \\ B_y \end{pmatrix} = \begin{pmatrix} -B_1 e^{-ky}\,\cos(kx) - B_{bias} \\ +B_1 e^{-ky}\,\sin(kx) \end{pmatrix}. \tag{2.43}$$

This bias field alternately adds and cancels with the mirror field (Figure 2.7(a)), leading to a field strength

$$B = \sqrt{B_1^2\,e^{-2ky} + 2B_1 B_{bias}\,e^{-ky}\,\cos(kx) + B_{bias}^2}, \tag{2.44}$$

which is plotted in Figure 2.7(b). There are points where $\mathbf{B}_{bias} = -\mathbf{B}_1$ and the net field strength goes to zero. These points are surrounded by closed contours, which indicate that there are elliptical tubes running parallel to the mirror surface along the z-direction.

The field zeroes occur at positions $x_0 = \lambda_M\,(n \pm 1/2)$ and at a height

$$y_0 = \frac{1}{k}\ln\left(\frac{B_1}{B_{bias}}\right). \tag{2.45}$$

Taylor expanding the field about the zero gives, to first order:

$$\begin{pmatrix} B_x \\ B_y \end{pmatrix} = -kB_{bias}\begin{pmatrix} y - y_0 \\ x - x_0 \end{pmatrix}. \tag{2.46}$$

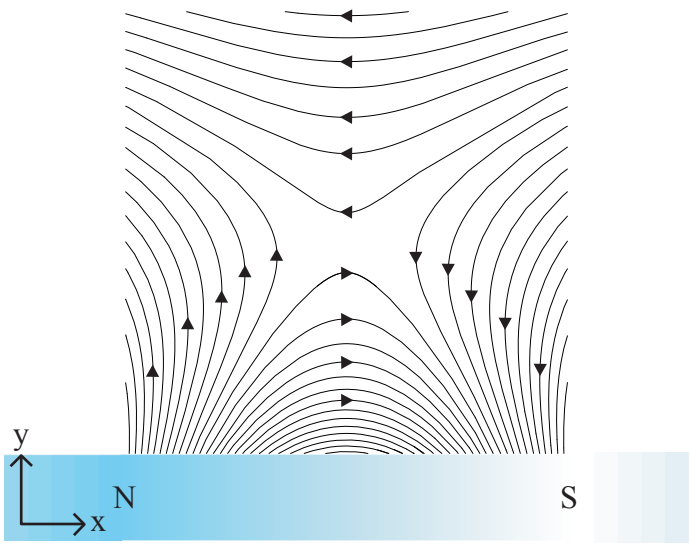

Figure 2.8 *Orientation of the magnetic field lines around a microtrap.*

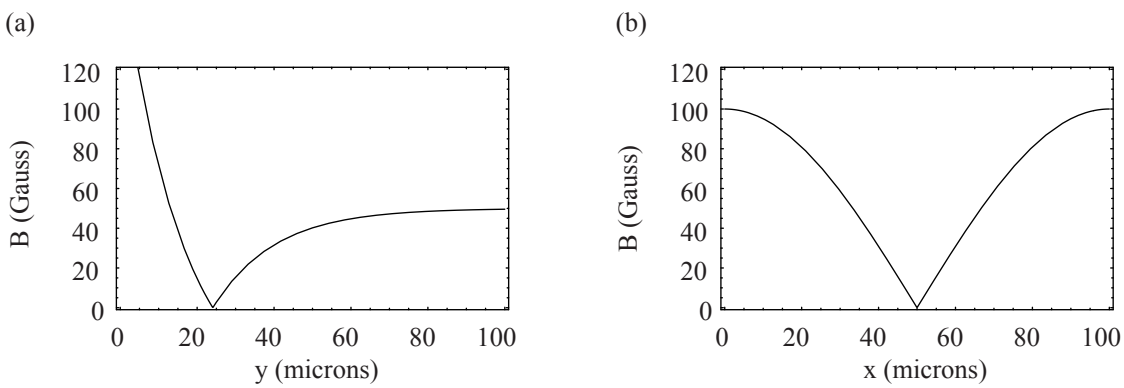

Figure 2.9 *Cross-sections of the magnetic microtrap potentials, for* $B_1 = 227\,G$, B_{bias}=$50\,G$, $\lambda_M = 100\,\mu m$.

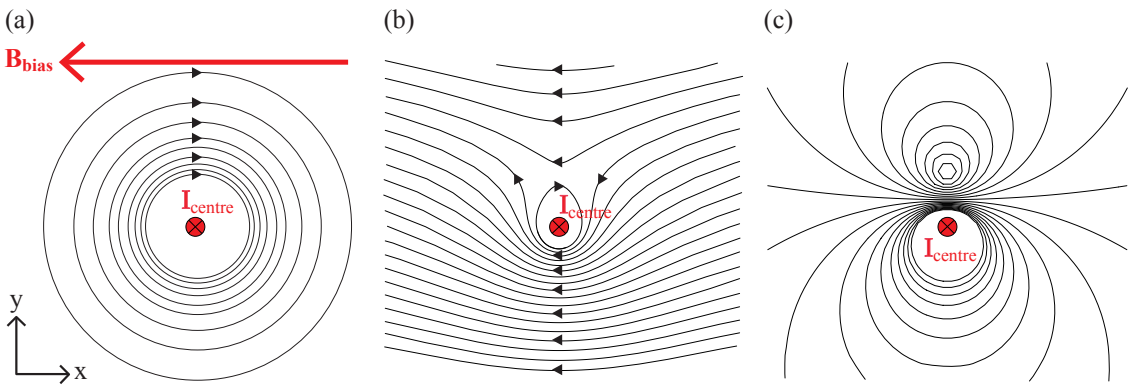

Figure 2.10 *(a) Addition of bias field, B_{bias} to field generated by centre wire current, I_{centre}; (b) Magnetic field vectors around the wire trap; (c) contours of constant magnetic field strength.*

This is the form of a quadrupole field, with the same orientation as is used for magneto-optical trapping (c.f. Section 2.1.2). The magnetic field lines around one of the zeroes are shown in Figure 2.8. The depth of each trap is equal to the applied bias field strength, B_{bias}. Close to the zero, the microtraps are cylindrically symmetrical: the radial ($r^2 = x^2 + y^2$) gradient is given by:

$$\alpha = \frac{\partial B}{\partial r} = kB_{bias}. \tag{2.47}$$

Cross-sections of the magnetic microtrap potentials are plotted in Figure 2.9.

The videotape manufacturer's specifications quote a thickness $b = 3.5\,\mu$m and a magnetic remanence field strength of 2.3 kG (see Section 3.2.1). From this, a surface field strength $B_1 = 227$ G is calculated for a $100\,\mu$m wavelength recording. The maximum bias field we can generate in the lab is at present ~ 50 G. This produces microtraps at a minimum distance of $25\,\mu$m from the surface. Therefore, the approximation made in writing Equation 2.30 is valid.

2.3.2 The wire trap

We now turn to the traps formed using the current carrying wires beneath the magnetic mirror surface. The 'centre' wire, a distance $d_c \approx 0.5$ mm below the surface is used in conjunction with the bias field to form a macroscopic trap by which atoms are transferred from the mirror-MOT to the microtraps.

The wire trap is formed as shown in Figure 2.10. The field from a current, I_{centre}, flowing along $\hat{\mathbf{z}}$ in a long wire located at $x = 0,\ y = -d_c$ is given by:

$$\begin{pmatrix} B_x \\ B_y \end{pmatrix} = \frac{\mu_0 I_{centre}}{2\pi(x^2 + (y + d_c)^2)} \begin{pmatrix} y + d_c \\ -x \end{pmatrix}. \tag{2.48}$$

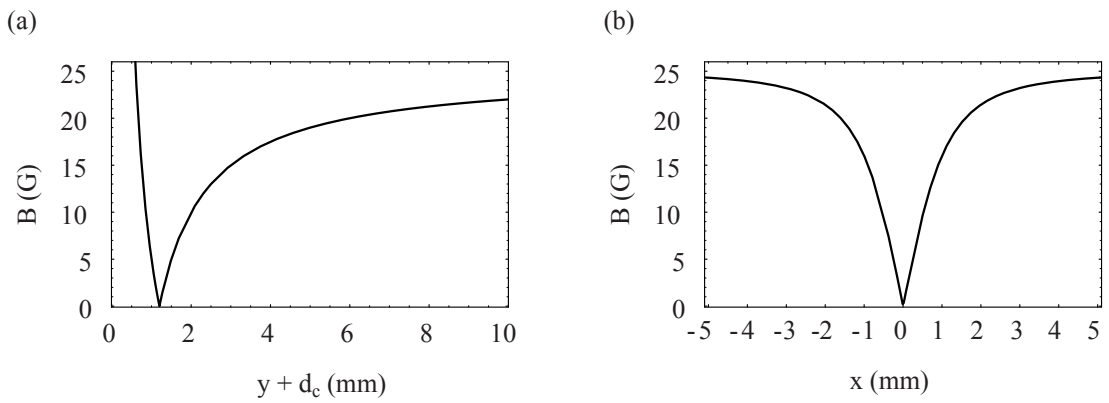

Figure 2.11 *Cross-sections of the wire trap, for $I_{centre} = 15\,A$, $B_{bias} = 25\,G$. ($y + d_c$ is the total distance from the centre wire.)*

(Here, $y = 0$ refers to the position of the videotape surface, as before.) When a uniform bias field, $\mathbf{B}_{bias} = -B_{bias}\,\hat{\mathbf{x}}$ is added, it cancels the field at a point above the wire where the two field are equal and opposite. This creates a line of zero field, parallel to the wire, at $x_0 = 0$ and a distance

$$y_0 = \frac{\mu_0 I_{centre}}{2\pi B_{bias}} - d_c \tag{2.49}$$

above the atom chip surface. The magnitude of the field is given by

$$B = \sqrt{\left(\frac{\mu_0 I_{centre}}{2\pi}\right)^2 \frac{1}{x^2 + (y+d_c)^2} - 2\left(\frac{\mu_0 I_{centre}}{2\pi}\right)\frac{(y+d_c)}{x^2+(y+d_c)^2} B_{bias} + B_{bias}^2}. \tag{2.50}$$

By making a Taylor expansion about the trap centre, the field close to the centre can be approximated as

$$\begin{pmatrix} B_x \\ B_y \end{pmatrix} = -\frac{2\pi B_{bias}^2}{\mu_0 I_{centre}} \begin{pmatrix} y - y_0 \\ x - x_0 \end{pmatrix} \tag{2.51}$$

$$= -\frac{B_{bias}}{y_0} \begin{pmatrix} y - y_0 \\ x - x_0 \end{pmatrix}. \tag{2.52}$$

This has the form of a quadrupole field, as can be seen from the field vectors plotted in Figure 2.10(b), with gradient

$$\alpha = \frac{\partial B}{\partial r} = \frac{2\pi B_{bias}^2}{\mu_0 I_{centre}}. \tag{2.53}$$

This approximation is valid to better than 10% within a radius $\sim y_0/2$ from the field zero. The cross-sections through the trap centre, (x_0, y_0), are plotted in Figure 2.11.

The similarity between the cross-sections of the wire trap and of the videotape microtraps should be noted (Figures 2.11 and 2.9). In theory, such a trap can be formed by cancelling any spatially varying magnetic field with a uniform bias field. This will always produce a linear trapping region, on the assumption that the field has a first order term in the Taylor expansion.

2.3.3 Addition of a uniform axial field

Both the microtraps and the wire trap presented above have a line of zero field along the z-axis, about which the radial field gradient is approximately linear. To prevent Majorana spin-flips at the axis of these 2D traps, it is necessary to eliminate the regions of zero field, as discussed in Section 2.2.2. Addition of a uniform bias field, B_0, along the axis of a 2D quadrupole trap acts to 'round out' the bottom of the trap, creating a harmonic region, as shown in Figure 2.12. This is because the orthogonal fields add in quadrature and the field at the centre of the 2D trap is no longer zero.

$$\begin{aligned} B &= \sqrt{B_x^2 + B_y^2 + B_z^2} \\ &= \sqrt{\alpha^2 r^2 + B_0^2}, \end{aligned} \tag{2.54}$$

where α is defined by Equations (2.47) and (2.53) for the microtraps and for the wire trap respectively. The radial trap cross-section becomes hyperbolic: parabolic

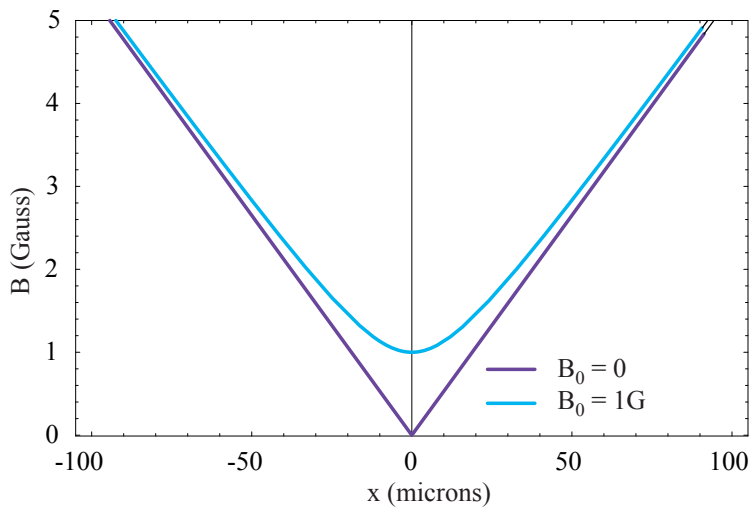

Figure 2.12 *Addition of an axial field to a 2D quadrupole field. The cross-sections are plotted for the wire trap, with parameters $I_{centre} = 15\,A$, $B_{bias} = 40\,G$. In the absence of the axial field ($B_0 = 0$), the radial cross-section is linear. Adding a field of 1 G creates a harmonic region at the centre of the trap.*

when $r \lesssim \sqrt{2}B_0/\alpha$ and linear when $r \gtrsim \sqrt{2}B_0/\alpha$.

In the harmonic region, the magnetic potential approximates to

$$B = B_0 + \frac{1}{2}\frac{\alpha^2 r^2}{B_0} \tag{2.55}$$

$$= B_0 + \frac{1}{2}\beta_r r^2, \tag{2.56}$$

where β_r is the radial trap curvature, $\beta_r = \partial^2 B/\partial r^2$. For harmonic trapping regions, it is possible to define a trap frequency. Consider a simple harmonic oscillator, $F = -m\omega_r^2 r$. For an atom of mass m in a 2D harmonic magnetic potential, such as Equation 2.55,

$$F = -dE/dr = -g_F m_F \mu_B (dB/dr)$$

$$= -g_F m_F \mu_B \beta_r r, \tag{2.57}$$

thus

$$\omega_r = \sqrt{(g_F m_F \mu_B/m)\beta_r}. \tag{2.58}$$

For this particular case, we can express the trap frequency in terms of the radial field gradient, α and the axial field, B_0:

$$\omega_r = \sqrt{\frac{g_F m_F \mu_B \alpha^2}{m B_0}}. \tag{2.59}$$

2.3.4 Axial confinement

The microtraps and wire trap, as described so far, are strictly guides, not traps. In order to confine atoms in these geometries, the potentials must also exhibit a minimum in the axial direction. In this experiment, two parallel wires, orthogonal to the axis of the traps are used to generate an axially confining potential. This is shown in Figure 2.13. These 'end wires' have a separation $s = 8.5\,\mathrm{mm}$ and are located at a depth $d_e \approx 1.4\,\mathrm{mm}$ below the atom chip surface.

The upper part of the figure shows the wires and field lines around each; the lower part shows the variation of the z-component of the field with z for two fixed heights above the atom chip. It is important to understand that the axial confinement field is simply the z-component, not the total magnitude, of the field generated by the end wire currents. The end wires generate a significant field component along $\hat{\mathbf{y}}$, but this does not contribute to axial confinement. To understand this, consider the magnetic guide potentials described in the preceding sections: the magnetic field vectors lie in the x–y plane and the trap centres are defined by a line of zero field parallel to the z-axis. When the field from the end wires is superposed, any y-component from

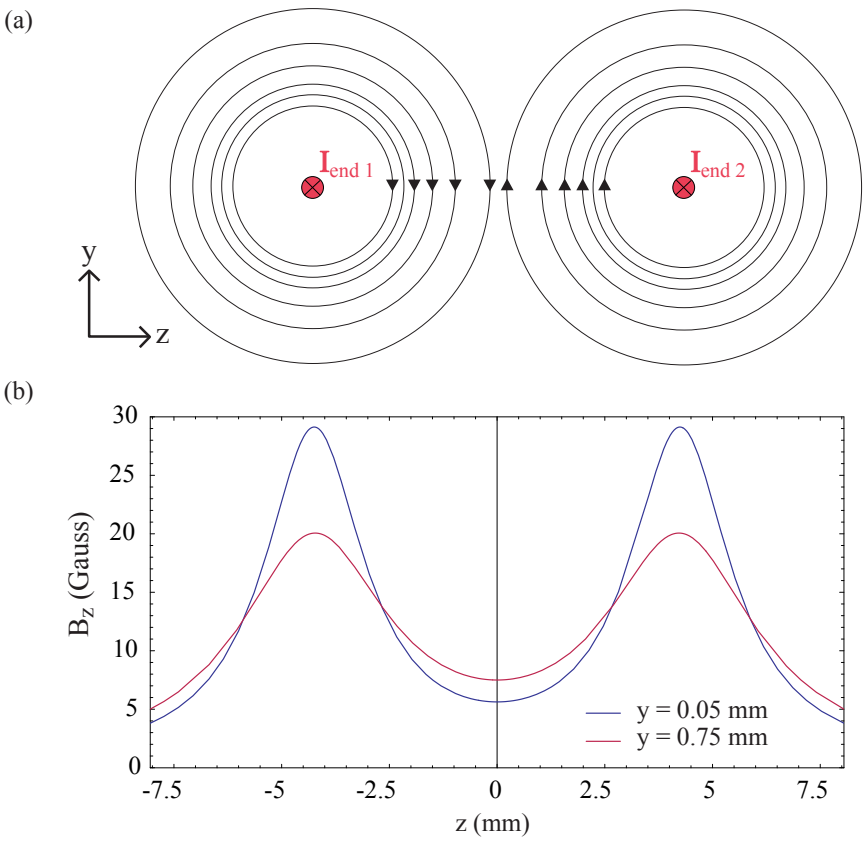

Figure 2.13 *Generation of the axial confinement potential. (a) Magnetic field vectors due to the two end wires; (b) axial variation of z-component of the magnetic field at two distances to the atom chip surface, for* $I_{end} = 10\,A$*. (These positions correspond approximately to the limits of the region in which atoms are trapped in the experiments of this thesis.)*

this field will simply add with the 2D quadrupole fields, acting to shift the position (x_0, y_0) of the magnetic field minimum. (This effect will be dealt with later.) Along the line of this new radial field minimum, the additional potential generated by the end wires is simply the z-component of their field. Atoms trapped radially by the magnetic tube potential minimum will experience a (non-zero) spatially varying magnetic field as they travel along the guide, which prevents them from escaping at the ends. Hence, for a current I_{end} in the end wires, the field producing axial confinement is given by:

$$B_z = \frac{\mu_0 I_{end}(d_e + y)}{2\pi}\left(\frac{1}{(d_e+y)^2 + (-s/2+z)^2} + \frac{1}{(d_e+y)^2 + (s/2+z)^2}\right) \quad (2.60)$$

As shown in Figure 2.13, the profile of $B_z(z)$ is a function of the height above the surface. The depth of the axial trap depends on the difference ΔB_z between $B_z(\pm s/2)$ at each end and $B_z(0)$ at the centre. This difference is plotted in Figure 2.14 for the region of interest. Figure 2.15 shows $B_z(0)$ versus y.

A non-zero axial field is necessary to prevent Majorana spin-flips and to create a harmonic trapping region in the radial direction. However, the radial frequency decreases with increasing axial field (Equation 2.59). Therefore, a uniform axial field is applied, which opposes the field of the end wires — this partially cancels the axial field at the trap centre and is used to tune the radial trap frequency. This axial 'cancelling field' is produced by an external pair of Helmholtz coils, and can be considered uniform over the trapping region. The axial trap depth and profile remain unchanged — Equation 2.60 is modified only by addition of a constant. The minimum field is typically chosen to be $\sim 1-2\,\mathrm{G}$. This is sufficient to prevent spin-flips but still low enough to permit tight radial confinement and high radial trap frequencies.

The axial field is harmonic within $\sim 10\%$ over a region of several millimetres around $z = 0$. At a height of 0.75 mm above the surface, the harmonic region extends over 3.5 mm. Closer to the surface, at a height of 0.05 mm, the harmonic region is 2.6 mm. By analogy with Equation 2.58, we can express the axial trap frequency as:

$$\omega_z = \sqrt{(g_F m_F \mu_B/m)\beta_z}\,, \quad (2.61)$$

where

$$\beta_z = \frac{\partial^2 B_z}{\partial z^2} \quad (2.62)$$

is the axial field curvature. This leads to:

$$\omega_z = \sqrt{\frac{\mu_0 I_{end}}{2\pi}\frac{(d_e+y)g_F m_F \mu_B}{m}\left(\frac{4s^2}{((d_e+y)^2+(s/2)^2)^3} - \frac{4}{((d_e+y)^2+(s/2)^2)^3}\right)}. \quad (2.63)$$

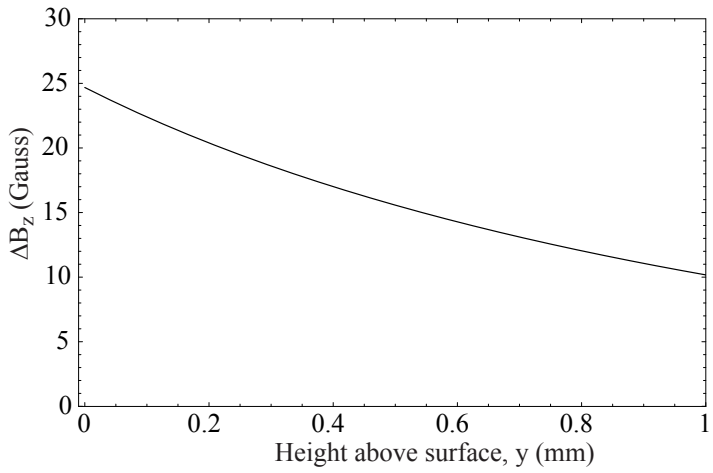

Figure 2.14 ΔB_z *as a function of height above the atom chip surface. This is a measure of the trap depth for axial motion.*

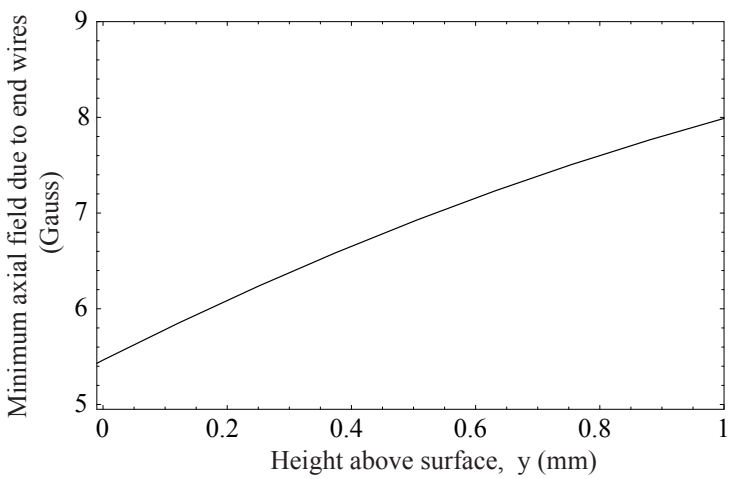

Figure 2.15 *Minimum axial field generated by the end wires, as a function of height above the atom chip surface.*

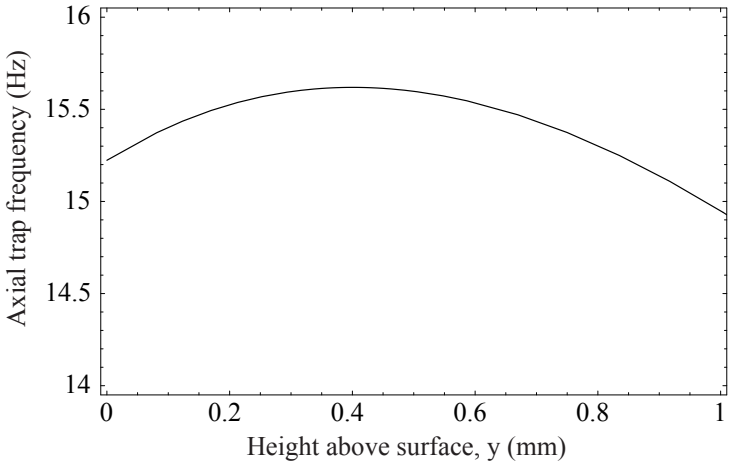

Figure 2.16 *Axial trap frequency as a function of height above the atom chip surface.*

The axial frequency as a function of height is plotted in Figure 2.16.

2.3.5 Trap twist

The end wires also produce a significant field component, ΔB_y, in the $\hat{\mathbf{y}}$ direction. This is zero at the trap centre and increases approximately linearly to a maximum close to the trap ends. The magnitude of this component decreases with height above the surface, as shown in Figure 2.17. When considering the effect of this on the wire trap, we can treat it as a perturbation of the bias field, B_{bias}. This rotates the effective bias field through a small angle, resulting in a small shift of the trap centre. This is depicted in Figure 2.18. The effective bias field, B'_{bias}, is rotated by an angle $\theta = \arctan(\Delta B_y / B_{bias})$, as well as undergoing a small change in magnitude. The displacement of the wire trap position is:

$$\Delta x = \frac{\mu_0 I_{wire}}{2\pi B'_{bias}} \sin\theta \tag{2.64}$$

$$\Delta y = \frac{\mu_0 I_{wire}}{2\pi B_{bias}} - \frac{2 I_{wire}}{B'_{bias}} \cos\theta. \tag{2.65}$$

Since the y-component of the field generated by the end wires varies along the trap axis, the displacements Δx and Δy also vary along the length of the trap. The result is that the wire trap is slightly twisted/rotated, rather than being parallel to $x = y = 0$. The displacements Δx and Δy are plotted in Figure 2.19 for typical trap parameters, $B_{bias} = 22\,\mathrm{G}$ and $I_{wire} = 15\,\mathrm{A}$. This trap is formed at a height of $0.7\,\mathrm{mm}$ above the atom chip surface and corresponds to the trap into which atoms are initially loaded from the CMOT.

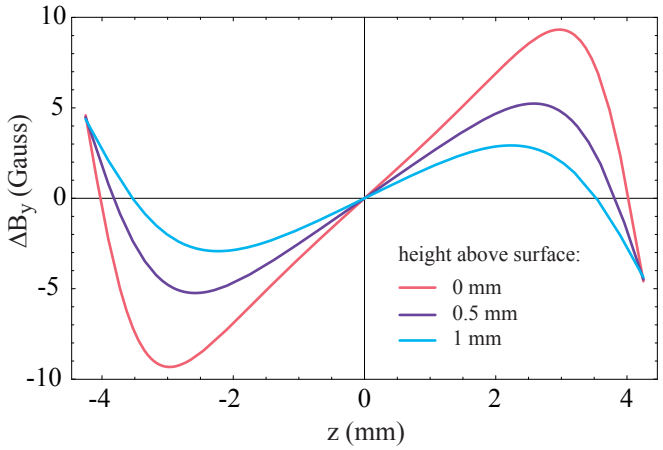

Figure 2.17 *The end wires generate a magnetic field component ΔB_y in the y-direction, in addition to the axial confinement field. This is plotted for three different heights above the atom chip surface.*

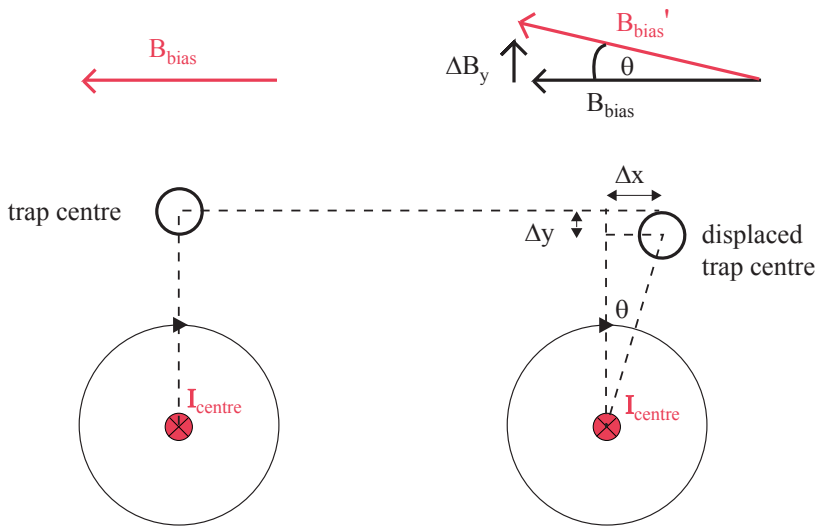

Figure 2.18 *Shift of wire trap position due to y-component of end wire field. This additional component, ΔB_y, adds with B_{bias} to form B'_{bias}. The effective bias field is rotated, shifting the position of the trap minimum.*

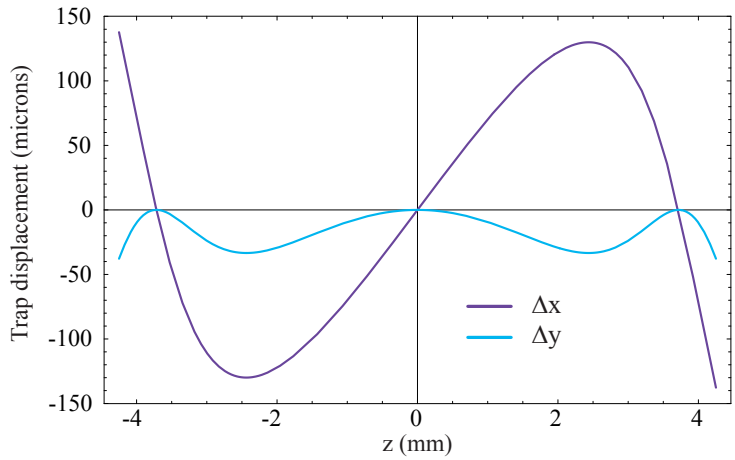

Figure 2.19 *Trap displacement due to end wire field. The graph shows the displacement of a typical wire trap (I_{centre}=15 A, B_{bias}=22 G, y_0=0.7 mm) due the y component of magnetic field generated by 20 A in the end wires.*

2.3.6 Effect of gravity on the trapping potential

In addition to the magnetic potential, gravity also contributes to the potential in which atoms are trapped. The derivations of magnetic potentials presented in this chapter have so far assumed that the atom chip was positioned with the magnetized surface uppermost. In fact, during the course of the development of this experiment, the atom chip was inverted: it is now suspended upside down in the vacuum chamber. Therefore, gravity acts in the $+\hat{\mathbf{y}}$ direction. The equilibrium point of a magnetic trap is shifted by a distance Δy, where:

$$\begin{aligned} +m\omega_r^2 \Delta y &= mg \\ \Delta y &= g/\omega_r^2. \end{aligned} \tag{2.66}$$

The weakest magnetic trap we load atoms into has a radial frequency of $2\pi \times 90\,\mathrm{Hz}$. The shift in the $\hat{\mathbf{y}}$ direction is therefore equal to $30\,\mu\mathrm{m}$, which is approximately 10 times smaller than the FWHM of a typical cloud trapped with these parameters (c.f. Section 5.2). In the experiments of this thesis, the trap displacement due to gravity is always negligible.

2.3.7 Contour plots of the traps

So far, we have considered each contribution to the magnetic trapping potential separately. Using Mathematica, the total potentials can be plotted for any given

parameters. As will be described later in this thesis, atoms are loaded into the wire trap, $\sim 0.7\,\mathrm{mm}$ from the surface, after which the centre wire current and bias field are ramped to values where the wire trap merges with the microtrap array. Figure 2.20(a) shows the upper wire trap. For the typical parameters shown, the wire trap is located $\sim 0.3\,\mathrm{mm}$ from the surface; very close to the surface, the videotape microtraps can be seen. We can consider the microtraps to be formed by the videotape magnetic field and an 'effective bias field', that is the vector sum of the applied bias field and the opposing field of the centre wire at the surface. Figure 2.20(b) shows the magnetic traps for a different set of parameters, at which the upper wire trap merges with the microtrap array. For these parameters ($I_{centre} = 11\,\mathrm{A}$, $B_{bias} = 42\,\mathrm{G}$), the effective bias field at the surface is $15\,\mathrm{G}$. However, the trap depth is still determined by the applied bias field, $42\,\mathrm{G}$.

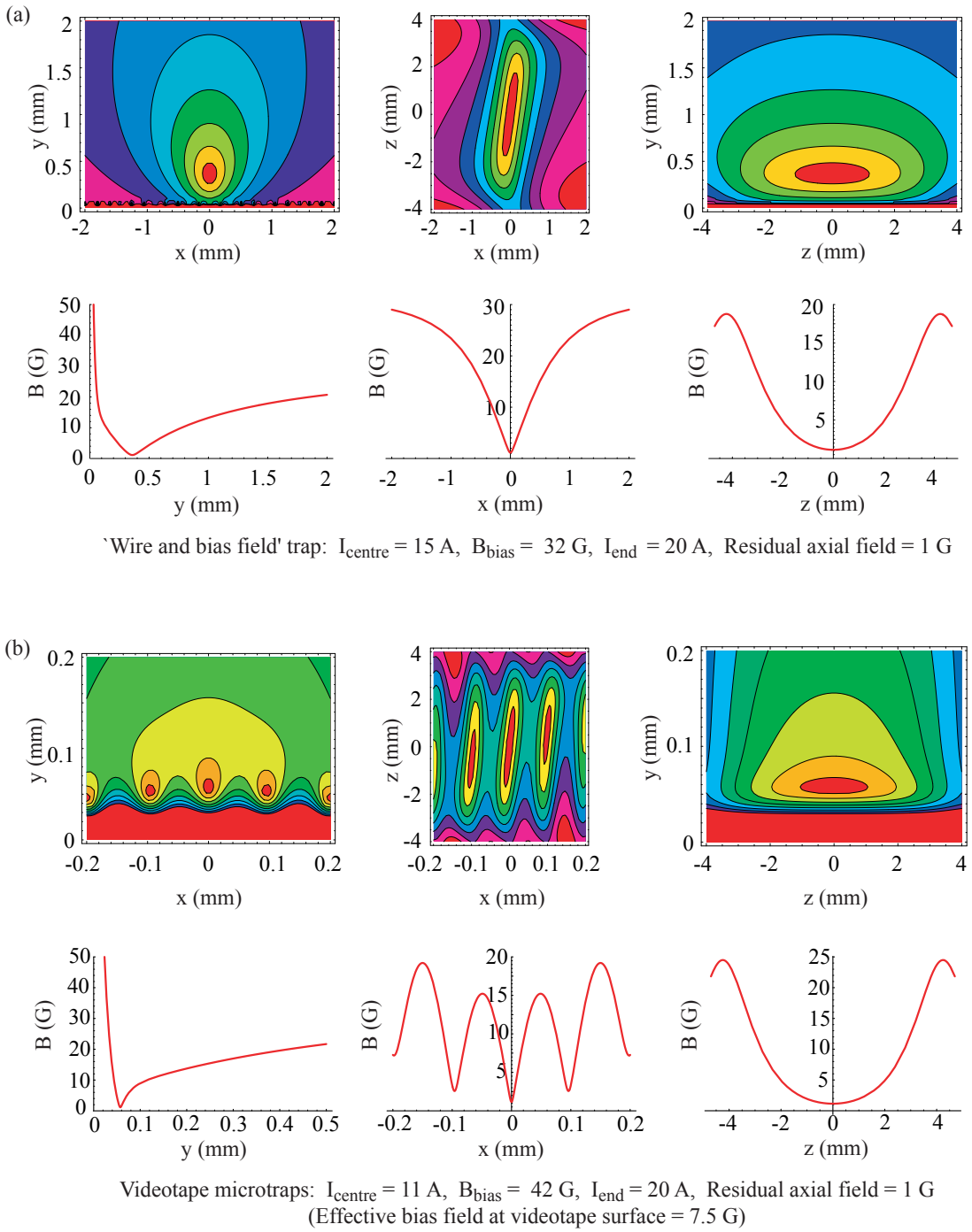

Figure 2.20 *Contour plots of the magnetic traps, using calculations of the full potentials, including gravity. The sections are plotted at the height of the field zero; the contours correspond to 4, 8, 12, 16, 24, 28, 32 G. In the experiment, the chip is suspended upside down, so gravity acts along $+y$.*

Chapter 3

The Atom Chip

This chapter deals with the construction and characterization of the atom chip, which is central to this thesis. The unique aspect of this atom chip is the permanently magnetized surface, which is used in conjunction with a uniform bias field to generate microscopic trapping potentials. All other magnetic atom chip experiments under investigation are based on arrangements of current-carrying wires.

Various design features of the atom chip are important for the processes involved in loading atoms into the microtraps. The magnetized surface is gold coated so that it acts as a reflector for the mirror-MOT — atoms can be collected from the background vapour and cooled just a few millimetres from the magnetized surface. A current-carrying wire below the surface (the 'centre' wire) is used both to compress the mirror-MOT (see Section 5.2) and to form a wire trap for transfer of the atoms from the MOT to the microtraps. The chip also incorporates wires for closing the ends of the magnetic traps and for generating an rf field for evaporative cooling.

The convention in our laboratory (and in this thesis) is that we describe the atom chip as if its surface is uppermost. In practice, the chip is inverted in the vacuum chamber, but in this thesis we shall continue to refer to the region of space in which atoms are trapped as 'above the atom chip surface'.

3.1 Atom chip design

This section describes the bulk structure of the atom chip. The magnetic mirror, which forms the upper layer of the atom chip, will be described in detail in the next section. The magnetic mirror consists of a magnetized piece of videotape, glued to a thin glass substrate and coated with a reflective layer of gold. In relation to the rest of the atom chip, the important criterion for the magnetic mirror is that it be

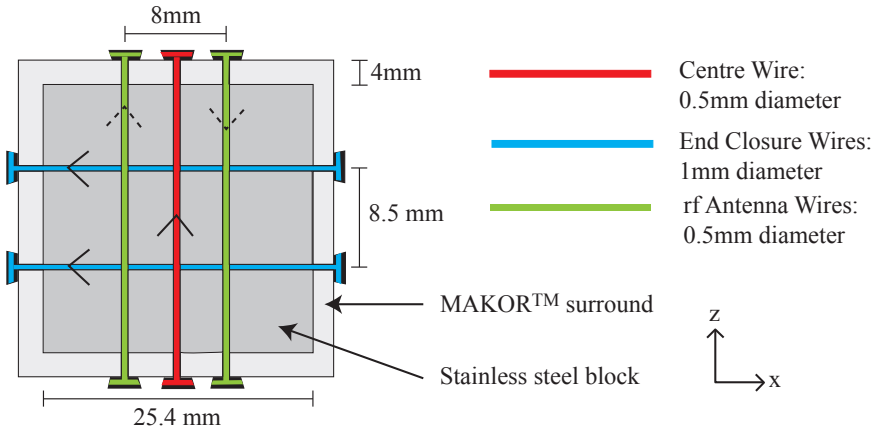

Figure 3.1 *Schematic of the atom chip. The magnetic mirror (not shown) covers over the area of the steel block. Typical currents are 15 A in the centre wire and 20 A in the end wires. The arrows indicate the direction of currents in the wires.*

kept as thin as possible, so that the distance between the underlying wires and the trapping region is minimized. It must also provide a large reflective surface area, comparable with the diameter of the mirror-MOT beams.

A schematic of the atom chip is shown in Figure 3.1. It is made from a 1 inch square stainless steel block surrounded by MACOR (a ceramic compound). The block is machined with channels to carry the wires, which are made from ceramic-coated copper and connect to screws on the MACOR surround. The centre wire, used to form the wire trap, is 500 μm in diameter and positioned so that its upper surface is flush with the surface of the block. Two additional 500 μm wires lie on either side of the centre wire. These are connected in series, such that current flows in a loop, and are used an rf antenna. Two parallel end closure wires run orthogonal to the centre wire, with an 8.5 mm separation. These wires have a diameter of 1 mm and carry a typical current of 20 A.

Heatsinking and vacuum compatibility are important considerations for design of the atom chip. Ceramic coated wires proved to be a good choice on both counts. The insulation is a good thermal conductor, so the wires are well heatsunk by contact with the steel bulk of the atom chip. We initially experimented with Kapton-coated wire — the insulation is thinner, which would have slightly reduced the distance between the wires and the trapping region. However, this was found to outgas in vacuum when resistively heated by the wire currents. In contrast, we have run currents of up to 20 A in the ceramic coated wires, for up to 15 s, with no

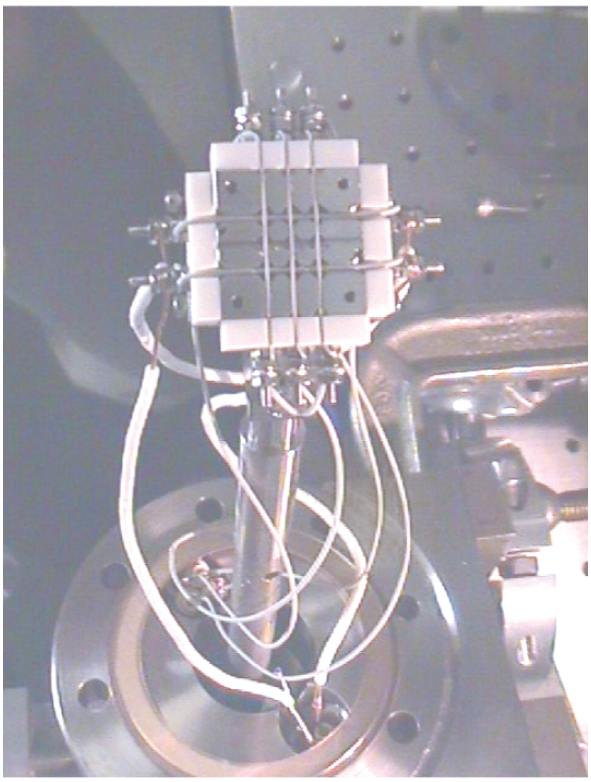

Figure 3.2 *The atom chip assembly, with magnetic mirror removed to show the underlying wires.*

deterioration of the vacuum.[1]

To complete the atom chip, the magnetic mirror is stuck to the surface of the steel block using a UHV-compatible epoxy glue (BYLAPOX 7285). It is oriented such that the lines of constant magnetization are parallel with the centre wire. The magnetic mirror substrate is a glass coverslip of area 22 mm × 22 mm and thickness 150 μm. The distance from the upper surface to the axis of the centre wire is therefore expected to be no less than $\sim$ 400 μm. A calibration will be described in Section 6.6, based on measurements of the magnetic trap position for different centre wire currents, which shows that this distance is actually $\sim$ 580 μm.

The atom chip is attached to a flange of the vacuum chamber by a 23 cm long stalk, Figure 3.2. The atom chip surface is horizontal and located at the centre of the vacuum chamber. The wires on the atom chip are connected to feedthroughs on this flange by bare 0.5 mm copper wires. Ceramic spacers are used to prevent these wires touching each other or the stalk of the atom chip.

[1] We observe no reduction in the lifetime of magnetically trapped clouds of atoms after running current in the wires.

3.2 The magnetic mirror

Methods of creating permanent periodic magnetization patterns for magnetic atom-mirrors fall into two main categories: those constructed from assemblies of small permanent magnets [75, 76] and those based on magnetic storage media, developed within this research group [8]. Various magnetic media have been investigated: audio tape, floppy disk and videotape. Of these, Ampex 398 Betacam SP videotape proved to be the most suitable for atom-optics experiments. One advantages is its high magnetic remanence, 2.3 kG, which leads to high surface fields (215.5 G for the recorded wavelength of these experiments). This provides a steep barrier between trapped atoms and the surface, and prevents loss of atoms to the surface. The second advantage is the capability to record a single track over the full 12 mm width of the videotape, thereby minimizing boundary effects. The technology for recording the videotape is well understood from previous work in this research group, but new techniques were developed to create a flat surface and to coat the surface with gold.

3.2.1 Material and magnetic properties of videotape

The videotape used, Ampex 398 Betacam SP [77], is $\frac{1}{2}$ inch (12.5 mm) wide and 14.5 μm thick. It is constructed from an 11 μm thick polyester film support with a graphite back-coating. The magnetic layer on the upper side is 3.5 μm thick and has a magnetic remanence field strength of 2.3 kG. As a commercial product, the videotape is designed to hold data reliably and robustly, which allows it to withstand being glued and pressed onto a substrate (see Section 3.2.3).

Tests were carried out in our laboratory to assess the compatibility of the videotape with UHV [78]. It was found that the videotape undergoes some chemical decomposition at temperatures above about 120 °C, therefore setting our temperature limit for baking the chamber[2] at 100 °C. After baking at 100 °C for 200 hours, the videotape has an outgassing rate at room temperature of $4 \times 10^{-10}\,\mathrm{Torr\,l\,s^{-1}\,cm^{-2}}$, mainly due to hydrogen [78]. This is probably further reduced by the gold surface coating. An important parameter for this experiment is the rate at which trapped atoms collide with background gas atoms, which limits trap lifetimes. This rate is proportional to the background pressure, $\sim 10^{-10}$ Torr in this set-up. For atoms trapped directly above the videotape surface, the collision rate due to outgassing hydrogen molecules is equivalent to an isotropic pressure of $p = Q/\bar{v}$, where Q is the outgassing rate and $\bar{v}$ is the mean speed of the desorbing molecules. Assuming a room temperature speed of $1800\,\mathrm{ms^{-1}}$, this equivalent pressure is 2×10^{-12} Torr,

[2] To achieve UHV, the vacuum chamber must be baked at a high temperature for a few days, see Section 4.2.

which indicates that trap lifetimes will be limited by the background pressure in the chamber, rather than by outgassing from the videotape surface.

The magnetic coating of the videotape consists of needle-like metal (Fe) particles, on average 100 nm long and 10 nm in diameter [79], embedded in a plastic binder. Each needle behaves as a single magnetic domain with uniaxial anisotropy. This arises due to minimization of the energy associated with the magnetic field surrounding each needle and causes the magnetization in each to point along its long axis [80]. While the binder is still liquid, the manufacturer applies a magnetic field parallel with the videotape. This results in all the needles aligning parallel with the videotape direction. Once the binder has set, the needles are no longer free to change their alignment. Hence the overall magnetization of the videotape is either parallel or anti-parallel with the videotape.

The magnetic properties of the videotape have been studied previously and found to agree well with the manufacturers specifications [81]. A hysteresis curve, shown in Figure 3.3, was obtained using an alternating gradient-field magnetometer (AGFM) [82, 83], which measures the total magnetic moment, μ, of a small sample in a homogeneous magnetic field. This can then be converted to a remanent magnetic field using the relation $B_r = \mu_0 M_r = \mu_0 \mu / V$, where V is the volume of the sample. (The measured sample had a diameter of 2 mm; we use the thickness, 3.5 μm, of the magnetic layer specified by the manufacturer.) The hysteresis curve plotted in Figure 3.3 was obtained for an applied field parallel with the videotape.

The hysteresis loop shows that a field of $4\,\mathrm{kG}/\mu_0$ is required to saturate the magnetic moment of the videotape. The magnetic remanence is calculated from the remanent field at $H = 0$ after saturation and is in agreement with the value 2.3 kG stated by the manufacturer. The coercive field is defined as the field required to reduce the remanent field to zero after saturation. The hysteresis loop indicates a coercive field of $1.5\,\mathrm{kG}/\mu_0$. This gives an estimate of the field strength that a recorded piece of videotape can be exposed to before becoming demagnetized.

3.2.2 Recording process and analysis of magnetization

The videotape was recorded using a standard $\frac{1}{2}$ inch tape drive (AMPEX VR-7003H) with custom-built record and playback heads [84]. This equipment can record a single track of up to 19 mm, thereby recording across the whole 12.5 mm width of the videotape. The recording process translates a time dependent voltage across the record head into a spatially varying magnetization pattern on the tape. To record the videotape for the atom chip, a constant 500 Hz sinusoidal signal was fed to the record head while the videotape was spooled at 60 rpm. With a spool radius of

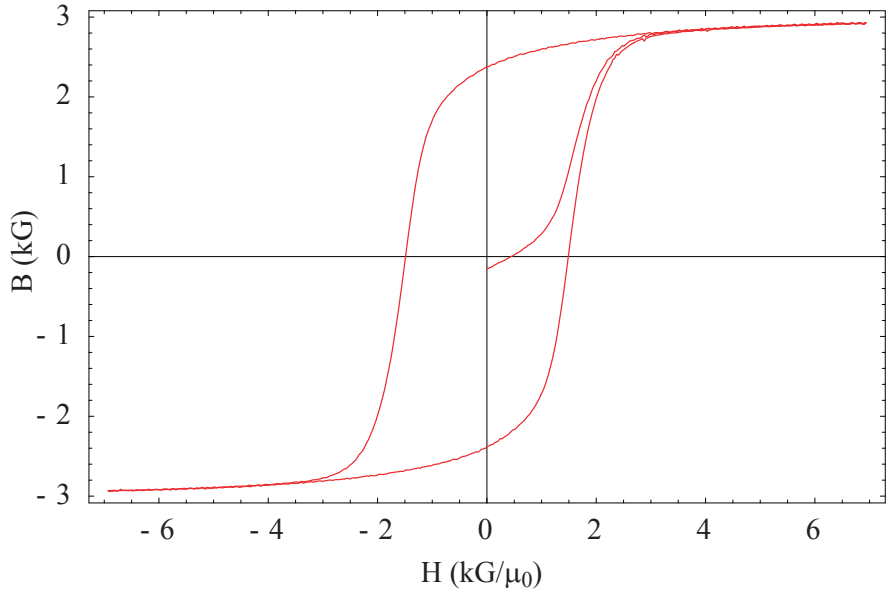

Figure 3.3 *Hysteresis curve for AMPEX 398 videotape measured with an AGFM. This graph is reproduced from [81]. The magnetic field is swept at a rate of* $500\,(G/\mu_0)\,s^{-1}$. *The magnetic field evolves from 0 to* $+7\,kG/\mu_0$ *to* $-7\,kG/\mu_0$ *then back to* $+7\,kG/\mu_0$. *The AGFM measures the total magnetic moment of a 2 mm diameter sample of videotape, from which the remanent field is calculated (see text).*

8 mm, this resulted in a sinusoidal magnetization of period $\sim 100\,\mu$m. Since the radius of the videotape on the spool grew with time, the recorded wavelength increased gradually along the length of the recorded videotape. The recorded wavelength of $100\,\mu$m is well above the minimum wavelength that can be recorded ($\sim 1\mu$m). At shorter wavelengths, it becomes increasingly difficult to saturate the magnetization of the videotape. A complete account of the recording process, together with a detailed description of the recording equipment, is given in [81].

MFM Analysis

Magnetic Force Microscopy (MFM) [85, 86] provides a method of investigating the field above the recorded videotape directly. We use a Digital Instruments Dimension 3100 Scanning Probe Microscope. This instrument employs a sharp, magnetized probe attached to an oscillating cantilever, which is scanned at a fixed height (typically $1\,\mu$m) above the sample surface. The cantilever is driven at a constant frequency by a piezo, close to the zero-field cantilever resonance. Typically, the oscillation amplitude is in the range $20-100$ nm. The interaction between the magnetized tip and magnetic fields produced by the surface changes the effective spring constant by an amount equal to the average vertical force gradient. The resulting frequency shifts are detected by measuring the phase shift of the cantilever oscillation relative to the piezo drive. Deflections of the cantilever are detected by reflecting a laser beam off its surface onto a quadrant photodiode.

In order to maintain a constant height above the surface during the MFM scan, the microscope first collects topographical information using Atomic Force Microscopy (AFM). The same tip is driven up and down very close to the sample surface, such that it taps on the surface lightly as it scans. Changes in the mean distance between the tip and the surface change the oscillation amplitude of the tip. The vertical position of the scanner is continuously adjusted to maintain a constant oscillation amplitude, thus recording the surface profile.

The x, y and z displacements of the scanning tip are controlled and measured by calibrated piezoelectric scanners. The probe is scanned back and forth across the x direction, while advancing very slowly along the z direction. During MFM operation, the surface and magnetic field scan lines are interleaved. Topographical data recorded during the surface scan is used to maintain a constant height during the following scan of the magnetic field above the surface. In this way, information about the surface topography and the magnetic field can be collected in the same scan.

To obtain detailed quantitative information from the MFM scans, we need to

consider the response of the tip to the magnetic fields above the surface. The analysis [73] given in Appendix B derives the relation between the magnetic field and the MFM signal. For the field above the magnetized videotape,

$$\begin{pmatrix} B_x \\ B_y \end{pmatrix} = \sum_{n=0}^{\infty} B_n e^{-nky} \begin{pmatrix} -\cos(nkx + \delta_n) \\ +\sin(nkx + \delta_n) \end{pmatrix}, \tag{3.1}$$

it is shown that the MFM signal is given by (Equation B.6):

$$\text{MFM Signal} = \sum_n \xi_n B_n \sin(nkx + \varphi_n) e^{-nky}. \tag{3.2}$$

The MFM signal is shown to be proportional to $\partial^2 B_y/\partial y^2$. Differentiating or integrating in y only contributes a constant factor, since we make the approximation that ξ_n of Equation 3.2 is a constant. Since $\nabla \cdot \mathbf{B} = 0$ and $B_z = 0$ (the field is independent of z), it follows that $\partial B_y/\partial y = -\partial B_x/\partial x$. From this, it should be clear that the MFM signal is also proportional to $\partial B_x/\partial x$.

Figure 3.4(a) shows an MFM scan of a rectangular area ($110\,\mu$m $\times$ $80\,\mu$m) of videotape, which was taken from the recorded length of videotape used to make the magnetic mirror of the atom chip. The MFM signal is represented by the colour scaling of the image. Integrating the image along z, i.e. orthogonal to the direction in which the videotape was recorded, gives the profile shown in Figure 3.4(b). The MFM profile is clearly not a pure sine wave — the recorded magnetization has been strongly distorted by the presence of higher harmonics in the magnetization. In order to produce as high a surface field as possible, a relatively high current was fed to the record head during the recording process. The subsequent saturation of the videotape magnetization resulted in the recorded pattern bearing closer resemblance to a square wave than a sine wave. The peaks and troughs of the MFM profile occur at the points where the horizontal component of the magnetization flips sign.

From Equation 3.1, the higher harmonics decay faster with height than the fundamental and the field eventually becomes sinusoidal at some distance from the surface. If we assume that the field at the surface is a square wave, then the relative amplitude of the third harmonic to the fundamental is $a_3/a_1 = 1/3$. We calculate that this ratio will have decreased to 1/30 at a height of $18\,\mu$m, and to 1/300 at a height of $37\,\mu$m above the surface. Above this height we can assume that the field lines follow a pure sinusoidal pattern. For the experiments in this thesis, the closest distance between magnetic trap centre and videotape surface is $25\,\mu$m, corresponding to an applied field of 50 G.

MFM does not lend itself well to analysis of such long wavelengths due to technical constraints: the maximum scan range is $112\,\mu$m and the maximum lift height

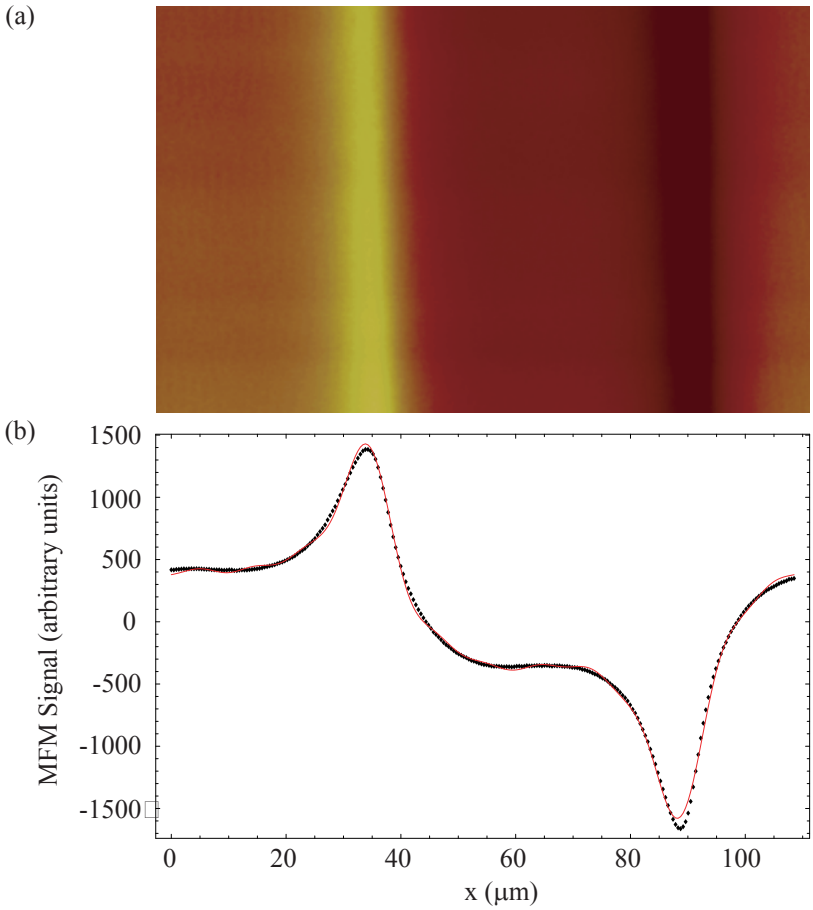

Figure 3.4 *MFM scan of the recorded videotape, at a height of 1 μm above the surface. (a) Image of the scanned area (110 μm $\times$ 80 μm), with MFM signal indicated by the colour scaling; (b) Profile of MFM scan (points), obtained by integrating the upper image along the z direction. Approximating ξ_n of Equation 3.2 to be a constant value, the profile was fitted (red line) to the function $\sum_n a_n \sin(nkx + \phi_n)$ for $n \leq 13$. (k and a_n are free parameters.) We find that the even harmonics have negligible amplitudes, as is expected on the grounds of symmetry. The dominant harmonics have relative amplitudes: $a_3/a_1 = 0.5, a_5/a_1 = 0.25, a_7/a_1 = 0.15$. These amplitude ratios are similar to those expected for a square wave.*

of the probe is $3\,\mu$m. Therefore it is neither possible to scan across several wavelengths, nor to scan the magnetic field at heights comparable to the decay length of the fundamental harmonic.

Demagnetizing Experiments

The magnetic mirror surface is located $\sim 500\,\mu$m above the centre of the underlying wires. If the centre wire carries a current of 15 A, the field at the surface will be $\sim$ 75 G. We were concerned that repeated switching of this field would begin to demagnetize the videotape, despite its high coercivity ($1.5\,\mathrm{kG}/\mu_0$). An experiment was therefore performed whereby recorded samples of the videotape were exposed to high magnetic fields in the range $0 - 3$ kG and then scanned using the MFM to check for a reduction in the surface field. The fields were created using two very strong permanent magnets. These were fixed at the necessary distance apart to create the required field at their midpoint, which was measured using a calibrated gaussmeter. The videotape samples were passed through this field such that the field lines were parallel to the direction of recording. The amplitude of the magnetic field above the videotape was then obtained from an MFM scan at a fixed height above the surface. Videotape recorded with a much shorter wavelength ($\sim 10\mu$m) was used for this experiment, to facilitate MFM analysis. The main advantage was that, since it is more difficult to saturate the videotape magnetization at a short wavelength, the field above this videotape was close to sinusoidal, even at the scan height of the MFM. The response of the MFM was therefore also sinusoidal. In addition, a distance covering several wavelengths could be scanned, so it was straightforward to measure the amplitude of the recorded pattern at a fixed height above the surface. The results are shown in Figure 3.5.

This demonstrates that the magnetization is robust to fields of 500 G, which are much higher than the maximum 75 G to which the magnetic mirror of the atom chip will be exposed. Fields of over 1 kG are required to substantially decrease the amplitude of the recorded pattern.

The magnetic anisotropy of the videotape was also demonstrated, as applying a 3 kG field orthogonal to the direction of the recording has a much weaker effect on the magnetization — the magnetic field amplitude above the surface is only reduced by a factor of 2 in this case, compared to complete demagnetization when this field is applied along the weak magnetic axis.

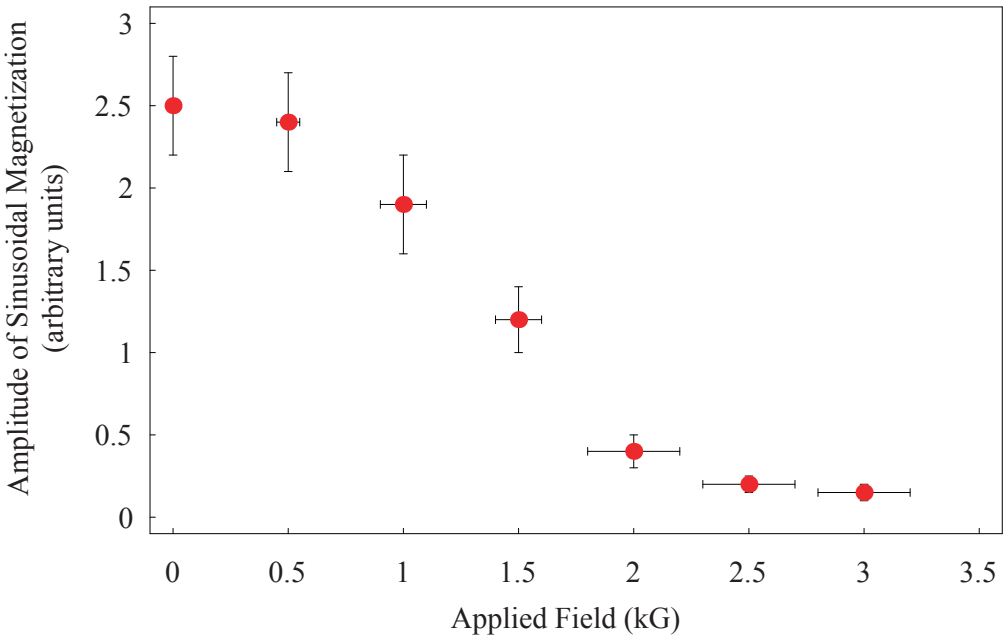

Figure 3.5 *Demagnetizing the recorded videotape. Pieces of videotape recorded with a 10 μm sine wave were exposed to magnetic fields of different strengths, parallel to the recording direction. The magnetic field amplitude was then obtained from an MFM scan at a fixed height above the videotape surface. The graph shows that the recorded pattern is robust to magnetic fields of up to 0.5 kG. Complete demagnetization of the videotape requires fields in excess of 2 kG.*

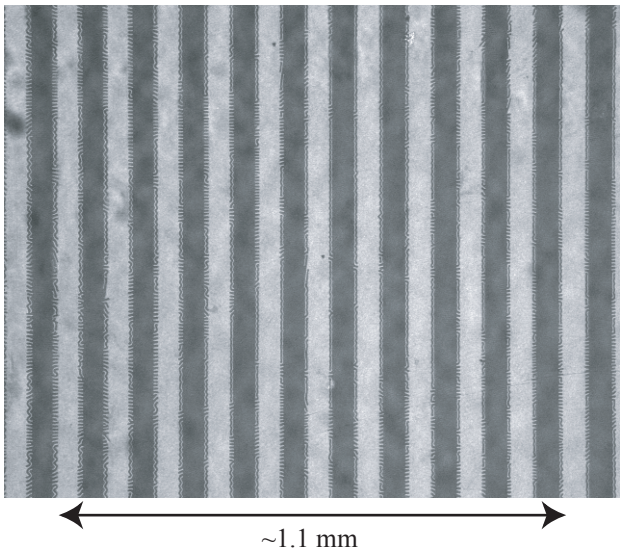

Figure 3.6 *Polarization microscopy of the videotape magnetization (see text). The alternating light and dark stripes indicate the local direction of the videotape magnetization. The image is calibrated by comparison with an accurate* $10\,\mu$*m grid. The wavelength is measured to be* $106 \pm 2\,\mu$*m.*

Polarization microscopy

The wavelength of the recorded magnetization is an important parameter for the calculation of the surface field of the magnetic mirror and the gradients of the magnetic traps formed above it. It is difficult to control this wavelength accurately during the recording process: it depends on the velocity of the videotape past the recording heads and therefore varies along the length of the tape. In order to measure accurately the wavelength recorded on the magnetic mirror, the videotape was examined under a polarization microscope. A glass substrate coated with a thin film of doped garnet (Nd:Lu:Bi) [87] is placed over the recorded videotape and illuminated with polarized light. The field from the videotape magnetizes the thin film: the latter has a saturation field of about 50 G, so is fully saturated by the videotape surface field. The film induces Faraday-rotation of the polarization of the reflected light, which is imaged through a second polarizer by the microscope. The sense of the rotation depends on the direction of the magnetization, so the direction of the local magnetic field is observed as very distinct light and dark stripes, as shown in Figure 3.6. The image from the microscope is stored digitally and compared with a calibration image. An accurate $10\,\mu$m grid structure is used to calibrate the image. The measured wavelength is $106 \pm 2\,\mu$m.

3.2.3 Fabrication of the magnetic mirror

The videotape magnetic mirrors previously constructed in this research group were spherically concave, in order to refocus reflected clouds of atoms, whereas for the purpose of atom chips, a flat magnetic mirror is required. Therefore a new technique was developed to produce a flat mirror. The challenge was to make as smooth and flat a mirror as possible on the thinnest possible substrate. The thickness of the substrate limits the final distance between the underlying wires and the trapping region. In order to produce high magnetic field gradients using the minimum currents in the wires, this distance must be kept as small as possible. Irregularities in the surface may distort the magnetic trapping potentials or the reflected MOT beams. Absorption imaging of a trapped cloud close to the surface also requires that the surface is very smooth and flat, as the imaging beam passes at grazing incidence to the surface.

The substrate used was a standard borosilicate glass coverslip, 150 μm thick with area 22 mm $\times$ 22 mm. These coverslips are available in a range of thicknesses and areas and have a flat surface (2–3 μm variation). Thinner coverslips were used initially, but it proved impossible not to break them at some stage during the fabrication procedure. A very fluid, slow-curing, 2-component epoxy glue (BYLAPOX 7285) was used to attach the videotape to the coverslip. This helped to prevent the formation of bubbles or fluctuations in the thickness of the epoxy layer which would lead to unevenness of the mirror surface.

The entire fabrication procedure which follows was carried out in the clean, dust-free environment of a laminar flow box:

- The glue was spread very thinly onto the coverslip and left for a short time for the small bubbles to disperse. Using a microscope, it was possible to remove larger bubbles with a fine needle.

- The videotape was first cleaned with methanol to remove a lubricant which was added to the videotape by the manufacturer to reduce wear on the video-recorder heads. (This lubricant had been found to outgas hydrocarbons in UHV.) The videotape was then slowly rolled onto the epoxy-covered coverslip from one end. As the videotape approached the coverslip, the surface tension between the epoxy and videotape helped to push any remaining bubbles out in front of the videotape.

- Finally the coverslip and videotape assembly was sandwiched between two glass slides, using photographic film (backing-side innermost) as a spacer, and pressed for 24 hours while the epoxy cured (Figure 3.7). The pressure applied

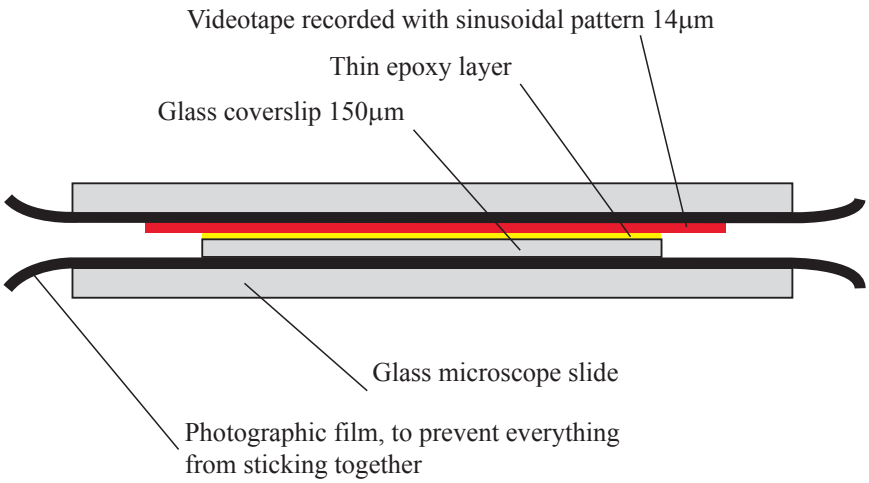

Figure 3.7 *Pressing the magnetic mirror. After gluing the videotape onto the glass coverslip, it is pressed between layers of photographic film, surrounded by glass slides.*

was as high as possible without breaking the coverslip. The photographic film (used first by [88] for this purpose) was crucial as it had a smooth enough surface to press the videotape against and was flexible. This meant it could be later peeled away from the coverslip, as it unavoidably becomes stuck to excess glue at the edges of the coverslip.

- After pressing, a 100 nm layer of gold was evaporated onto the videotape to produce a surface with high optical reflectivity. It was necessary to first evaporate a thin layer (5–10 nm) of chromium, as gold does not adhere well to the videotape. A standard evaporation procedure was used, whereby the gold or chromium was melted on a resistively heated filament in a chamber at 10^{-6} Torr. The magnetic mirror was placed at a distance of 30 cm in the chamber to produce as even a layer as possible.

3.2.4 Interferometry of the magnetic mirror surface

The gold coated magnetic mirror provides the reflective surface required to implement the mirror-MOT. To avoid intensity imbalances between the incident and reflected beams, it is necessary that the surface is smooth and has a high optical reflectivity.

An interferometer set-up was used to detect variations in surface height of the mirror. Images were taken of the fringe pattern arising from magnetic mirrors fabricated on both a rigid glass-slide and on the thin coverslip substrate. The first showed that our fabrication method can produce a surface which is flat to

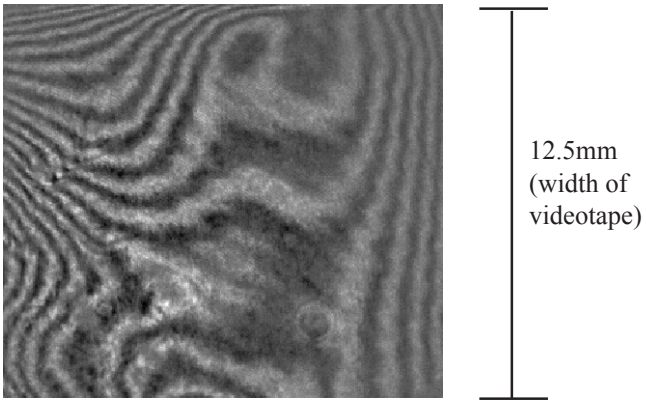

Figure 3.8 *Interferometry of the gold coated magnetic mirror surface, using 633 nm laser light. The number of fringes observed in a given area corresponds to surface height variations over that area, measured in wavelengths of the laser light.*

better than 2λ ($1.3\,\mu$m for the He-Ne wavelength of 633 nm). Interferometry of the magnetic mirror fabricated on the thin coverslip is shown in Figure 3.8. This shows that the mirror is locally smooth — the large central area shows a height variation of only $2\lambda = 1.3\,\mu$m over the entire 12.5 mm width of the videotape. However, it is considerably bowed in one direction, with a height variation of as much as $6\,\mu$m over 0.5 cm. This corresponds to an angular variation of 1 mrad. This problem arises because the coverslips are flexible. It is assumed that the videotape is slightly stretched when glued and pressed onto the coverslip and that the resulting tension curves the mirror. In order to overcome this problem, the magnetic mirror was pressed once more when glued onto the top of the atom chip. Once inside the chamber, it is noticeable that the reflected MOT beams are slightly distorted. However, the number of atoms trapped in the MOT above this surface is not affected: a mirror-MOT was initially realized using a standard high quality mirror, in which a similar number of atoms were trapped for the same laser beam power and detuning.

The optical reflectivity of the gold coated surface was determined by measuring the power in a 780 nm diode laser beam before and after reflection. The reflectivity at $45\,^\circ$ is 95 %. Figure 3.9 is a photograph of the complete atom chip, showing the gold surface.

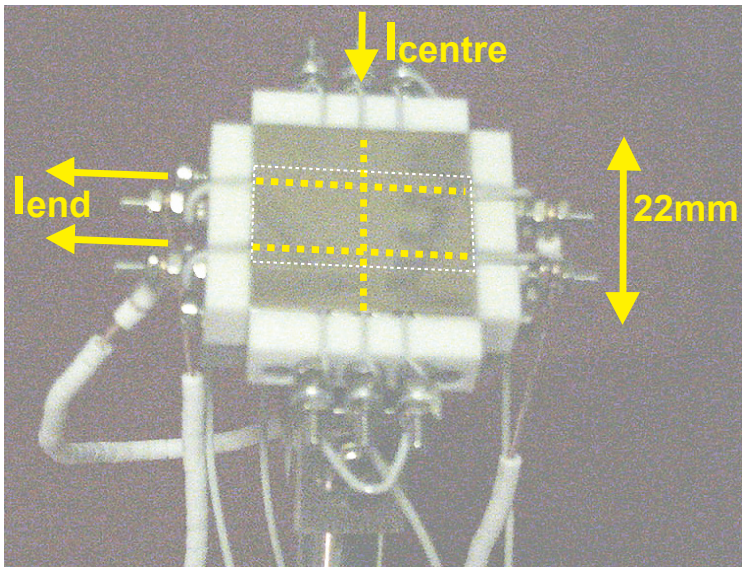

Figure 3.9 *The complete atom chip, showing the gold-coated videotape surface. The videotape covers the area outlined by the white dashed line, such that the stripes of the magnetization are aligned parallel with the centre wire.*

Chapter 4

Experimental Apparatus

This chapter deals with the experimental paraphernalia needed for cooling and trapping atoms. The main components are: a laser system to provide tunable laser light close to the trapping transition of rubidium; optics to prepare and control these beams; an imaging system; an ultra high vacuum system; various coils to generate magnetic fields and electronic control. The experiment is built on a $5' \times 10'$ optical table which floats on compressed air. The vacuum chamber is raised above the table on supports so that laser beams can be directed into it from below.

4.1 Laser system

4.1.1 Overview of the laser system

The ^{87}Rb magneto-optical trap is operated using laser light at two frequencies: the trapping transition ($5S_{1/2}$ F=2 $\rightarrow$ $5P_{3/2}$ F=3) and the repump transition ($5S_{1/2}$ F=1 $\rightarrow$ $5P_{3/2}$ F=2), which are separated by 6.6 GHz. Imaging and optical pumping require separate laser beams at the $5S_{1/2}$ F=2 $\rightarrow$ $5P_{3/2}$ F=3 and $5S_{1/2}$ F=2 $\rightarrow$ $5P_{3/2}$ F=2 transition frequencies respectively. To maximize the MOT atom number and lifetime, it is necessary to maximize the trap beam power and minimize the linewidth and long-term fluctuations of the laser frequency.

The trapping, imaging and optical pumping beams are all derived from a system comprising three diode lasers. A schematic of the system is shown in Figure 4.1. The ***reference*** laser is an external cavity diode laser (ECDL) (Section 4.1.2), locked continuously to the $5S_{1/2}$ F=2 $\rightarrow$ $5P_{3/2}$ F=3 transition. The locking signal is derived from a feature of the Doppler-free polarization spectrum (Section 4.1.4). This provides a stable, narrow (500 kHz) frequency reference. A second ECDL, the ***master*** laser, is offset-locked (Section 4.1.5) to the reference laser: the feedback

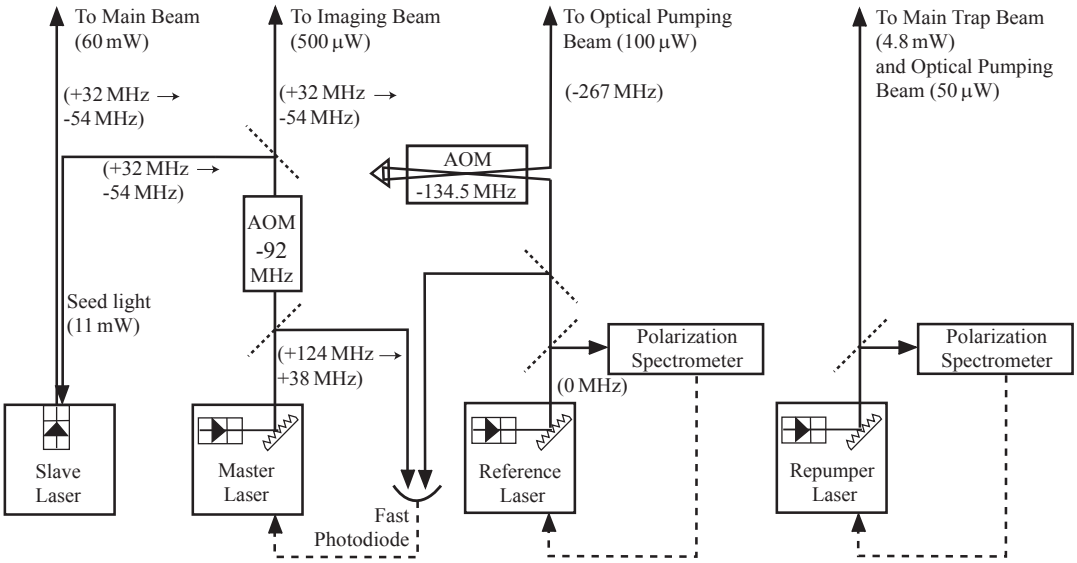

Figure 4.1 *Schematic of the laser system. The dashed lines indicate electronic feedback to the lasers. Detunings are indicated relative to the $5S_{1/2}$ F=2 → $5P_{3/2}$ F=3 transition of ^{87}Rb. The AOM operating at −92 MHz is used as a switch for the slave laser.*

signal is derived from the beat frequency observed when a small fraction of the two laser beams are combined on a fast photodiode. This method allows fast frequency shifting of the master laser, over a range of $\pm^{32}_{54}$ MHz from resonance, without the use of AOMs. A part of the output of the master laser is used for the imaging beam. The rest is used to seed the slave laser (see below). The third, ***slave*** laser is an injection-locked laser, seeded with light from the master laser. This arrangement maximizes the power output from a single diode laser (∼ 60 mW), and all of this output is used for the trapping beams. The ***repump*** light is provided by an independent ECDL, locked to the $5S_{1/2}$ F=1 → $5P_{3/2}$ F=2 transition frequency, using Doppler-free polarization spectroscopy. The optical pumping beam (Section 6.1) is derived from the reference laser light, its frequency shifted by the required −267 MHz using a double-pass AOM. It is combined with a small fraction of the repump laser light.

4.1.2 Lasers

The laser diodes used are Sanyo DL-7140-201, with a nominal wavelength 785 nm and a maximum output power of 70 mW. A bare laser diode will lase with a broad linewidth (∼100 MHz) and have poor tunability. It is common practice to narrow the linewidth by operating the diode in an external cavity with optical feedback

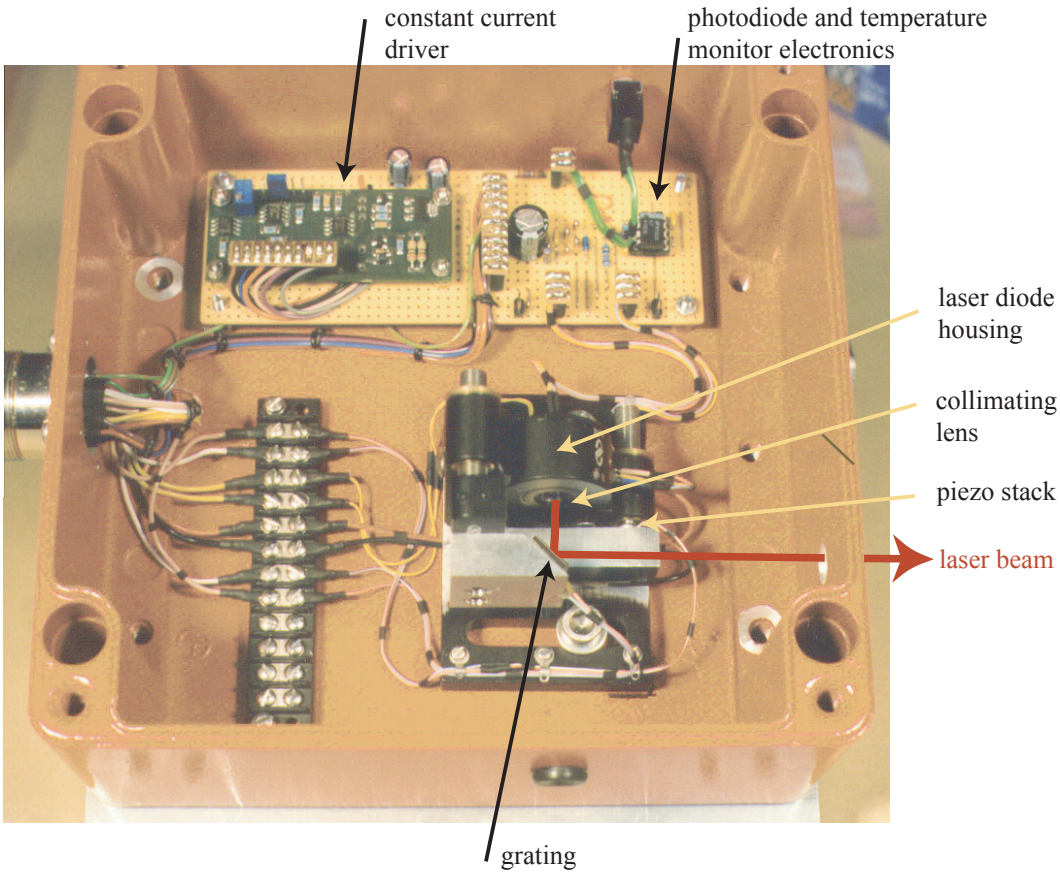

Figure 4.2 *External cavity diode laser. The laser diode is mounted on the fixed part of a standard mirror mount. The grating is mounted to the adjustable part of the mirror mount.* (Photo: P. N. Smith.)

[89]. Given that the D2 line of Rb has a natural linewidth of 6.07 MHz, the laser frequency must be stable to around 1 MHz or below.

The reference, master and repump lasers are all based on a design described in [90]. The back facet of the diode is $> 90\%$ reflective, whereas the front facet of the diode is anti-reflection coated by the manufacturer ($\sim$5% reflective). A Littrow-mounted, blazed diffraction grating completes the external cavity and provides frequency-selective feedback. The laser is constructed on an adapted mirror mount, as shown in Figure 4.2, with the diode and collimating lens housed on the back of the mount and the grating on the part with adjustable tilt. The first-order diffracted light ($\sim$20 % of the power) is reflected back into the laser and the zeroth order is coupled out. This design of laser can in theory have a linewidth below 100 kHz. In our experiment, it is limited by thermal and mechanical instabilities and current fluctuations.

The laser diode cavity has dimensions $\sim 1\,\mu$m horizontally and $\sim 3\,\mu$m vertically.

The beam expands anisotropically before the collimation lens, so the output beam is roughly elliptical (with ratio 3:1 oriented horizontally) and is vertically polarized.

In setting up the laser, coarse frequency tuning is achieved by varying the temperature and current while measuring the output wavelength with a wavemeter. We use a low-noise constant current driver [91] to minimize current fluctuations. Typically, the current is set to ∼60 mA. The temperature is stabilized to ∼16 °C by a Peltier cooler [92]. Fine frequency tuning is achieved by rotating the grating, which varies the length of the external cavity and adjusts the frequency of optical feedback. This can be done manually or by varying the voltage applied to a piezo-stack between the grating mount and its horizontal-tilt adjust screw. The main development to the laser, not described by [90], is the replacement of a high voltage piezoelectric transducer by this piezo stack. These have the advantage of being controlled by low voltage and allow a much greater scan range. The lasers can be scanned single-mode over a range of 2 GHz.

4.1.3 Frequency stabilization

To prevent the central frequency drifting with time, electronic feedback is used to tune and stabilize the laser to an external frequency reference. For the reference and repump lasers, Doppler-free polarization spectroscopy of the ^{87}Rb D2 line (Section 4.1.4) gives a frequency-dependent signal which is used as the error signal for feedback. If the laser frequency drifts, the piezo stack bias voltage and the current through the laser are adjusted to bring it back to the reference frequency. The error signal is separated into a high frequency component, which is fed back to the injection current, and a low frequency component, which is fed back to the piezo stack. The gain of each feedback signal is set as high as possible without exciting resonances in the piezo and laser, thereby minimizing the fluctuations which contribute to laser linewidth. When locked, the reference laser has a linewidth of 460 kHz.

4.1.4 Doppler-free polarization spectroscopy

This method [93, 94] is a simple extension to Doppler-free saturated absorption spectroscopy [95], by which sub-Doppler resolution of hyperfine spectra in obtained. The set-up is shown in Figure 4.3. The pump beam is circularly polarized and the probe beam is linearly polarized at an angle ϕ to the axis of an 'analyser' polarizing beam cube. The reflected and transmitted intensities from the analyser are incident on the two photodiodes and the difference between the two recorded intensities gives the polarization spectroscopy signal. For a polarization angle $\phi = \pi/4$, in the absence of the pump beam, equal intensities are recorded on the two

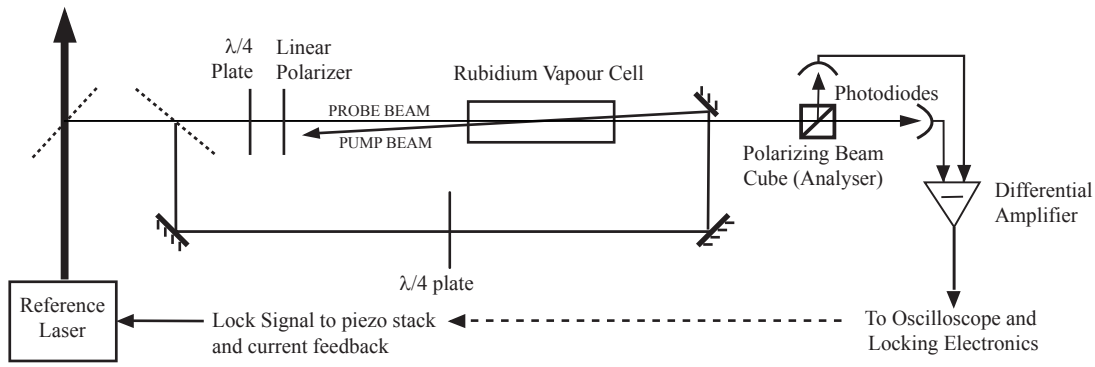

Figure 4.3 *Schematic of the polarization spectrometer set-up.*

photodiodes and the difference signal is zero. The linear polarization of the probe beam can be considered as the sum of two opposite circular polarizations, rotating in the same and opposite sense as the pump beam polarization. In addition to the usual saturation effects, the circularly polarized pump beam induces changes in the absorption coefficient (circular dichroism) and refractive index (gyrotopic birefringence) for the two components, due to the non-uniform optical pumping of the hyperfine sub-levels. The first effect introduces some ellipticity and the second rotates the polarization of the probe beam. This anisotropy is detected as a change in the difference signal. For example, the reference laser transition is $5S_{1/2}$ F=2 $\rightarrow$ $5P_{3/2}$ F=3. If the pump beam is σ^+ polarized, atoms are optically pumped across to the stretched state transition, $m_F = 2 \rightarrow m'_F = 3$. This maximizes the difference in absorption rates for the two circular components of the probe beam and a large difference signal is recorded.

The frequency dependence of the signal depends on the relative orientation of the probe beam polarization and the analyser. If the angle ϕ is very small, the signal is Lorentzian [93]. In this set-up, an angle close to $\phi = \pi/4$ is used. Assuming the birefringence in the cell is small, this gives a difference signal, S:

$$S = |E_0|^2 \, e^{-\alpha L} L \, \Delta\alpha_0 \frac{x}{1+x^2}, \tag{4.1}$$

where $x = \frac{\omega_0 - \omega}{\gamma/2}$, ω_0 is the centre frequency, $\gamma/2$ is the power-broadened transition half-width and $\Delta\alpha_0$ is the absorption difference at ω_0. Equation 4.1 is derived in Appendix C.

The difference signal is therefore dispersion shaped, with a zero-crossing to which we can lock. The polarization spectrum for the $5S_{1/2} \rightarrow 5P_{3/2}$ transition is shown in

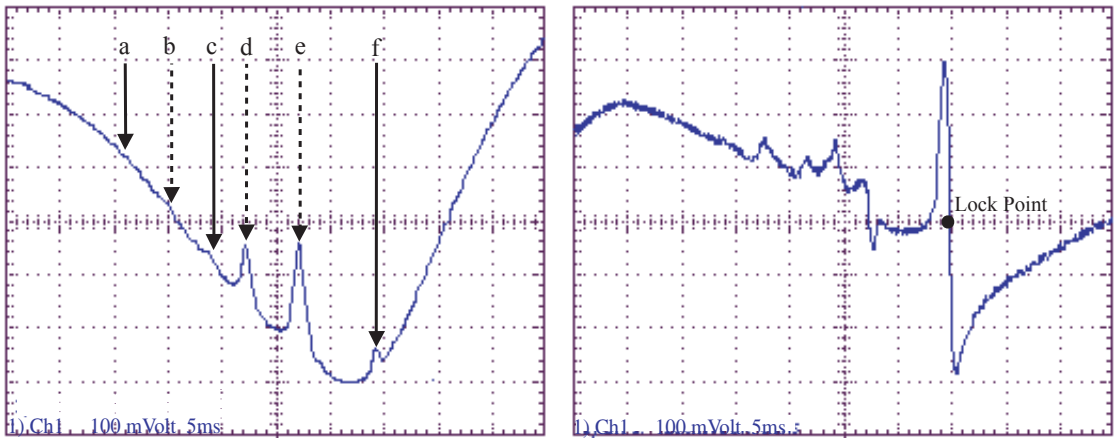

Figure 4.4 *Saturated absorption spectrum (left) and Polarization spectrum (right) of the $5S_{1/2}\,F = 2 \rightarrow 5P_{3/2}\,F' = 3$ transition of ^{87}Rb (same frequency scale). ((a): $F = 2 \rightarrow F' = 1$; (b): crossover $F' = 1, 2$; (c): crossover $F' = 1, 3$; (d): $F = 2 \rightarrow F' = 2$; (e): crossover $F' = 2, 3$; (f): $F = 2 \rightarrow F' = 3$.) The dispersion feature in the polarization spectrum corresponds to feature (f) and is the trapping transition. The frequency scale is approximately 95 MHz div^{-1}.*

Figure 4.4. The left hand image shows the standard saturated absorption image (the sum of the two detected intensities); the right hand image shows the polarization spectrum. There is a strong dispersion signal at the trapping transition (labelled (f) in Figure 4.4). The reference laser is locked to the zero-crossing of this feature. The exact position of the dispersion relative to the transition is dependent on the pump power — for this set-up, the centre of the dispersion feature is typically 3 MHz red-detuned of the transition. This effect can be counteracted by rotating the probe beam polarizer slightly. This shifts the voltage-offset of the signal so that we can lock to any point of the dispersion curve: a range of ~ 6 MHz. The capture range is determined by the frequency shift from the lock point to the next zero crossing in each direction. In Figure 4.4 (right image), the capture range can be seen to extend $\pm^{250}_{40}$ MHz from the lock point. If the voltage offset is shifted by +50 mV or more, the trace no longer crosses zero at frequencies below the lock point, for the range shown. The voltage offset can be achieved by simply rotating the probe beam polarizer, as described above, extending the capture range by over 700 MHz to lower frequencies. When locked to the dispersion feature, the reference laser has a linewidth of 460 kHz over 500 ms and can remain locked for over 12 hours.

The dispersion feature produced by polarization spectroscopy is ideal for locking the lasers. It avoids the problems commonly associated with locking to a saturated absorption feature. Locking to the side of a peak provides a steep slope but the

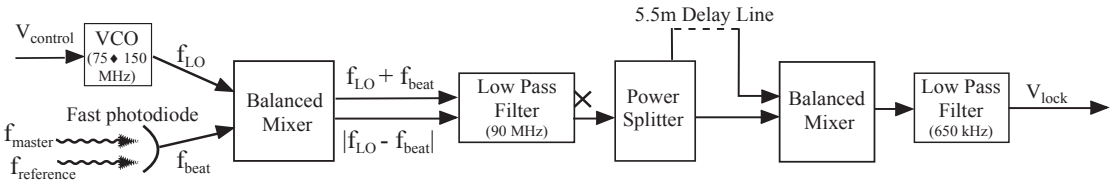

Figure 4.5 *Offset locking scheme.*

lock point drifts with laser intensity or beam alignment. This problem can be overcome by locking to a peak, but this requires modulating the laser frequency in order to generate a dispersion signal, either within the saturated-absorption cell loop using an AOM, or by modulating the laser current directly. The polarization spectroscopy scheme uses the difference of two signals, so does not drift with short-term fluctuations of laser intensity and requires no modulation. In addition, it provides a much larger capture range (though with a similarly narrow lock-feature), increasing the long-term lock stability.

4.1.5 Offset locking

The master laser is frequency-stabilized relative to the reference laser, using an error signal derived from the beat note between the two laser frequencies. This method enables fast frequency shifting of the trapping laser beams within a range of $+32 \rightarrow -54\,\mathrm{MHz}$ relative to the reference laser frequency. A similar scheme is described in [96].

A schematic of the offset-lock is shown in Figure 4.5. The reference and master laser beams are combined and focused onto a fast photodiode (Newport 818-BB-21A, cutoff frequency 1.2 GHz), generating a beat frequency, $f_{beat} = |f_{master} - f_{reference}|$, in the rf range. The VCO has four preset voltage inputs and outputs a local-oscillator frequency, f_{LO}. These two frequencies are sent to a balanced mixer, which generates the sum and difference frequencies, $f_{LO} + f_{beat}$ and $|f_{LO} - f_{beat}|$. The sum frequency is filtered out and the difference frequency is split into two equal-power components, one of which acquires a frequency-dependent phase lag, ϕ, by travelling along a delay line.

The phase lag acquired by a signal of frequency f, after propagating along a delay line of length l, is $\phi = 2\pi l f/v$, where v is the speed of the rf signal. The delay line is a coaxial cable, of length $l = 5.5\,\mathrm{m}$ in which the signal travels at $v = 2c/3$, independent of frequency. Hence,

$$\phi = \frac{3\pi l |f_{LO} - f_{beat}|}{c}. \tag{4.2}$$

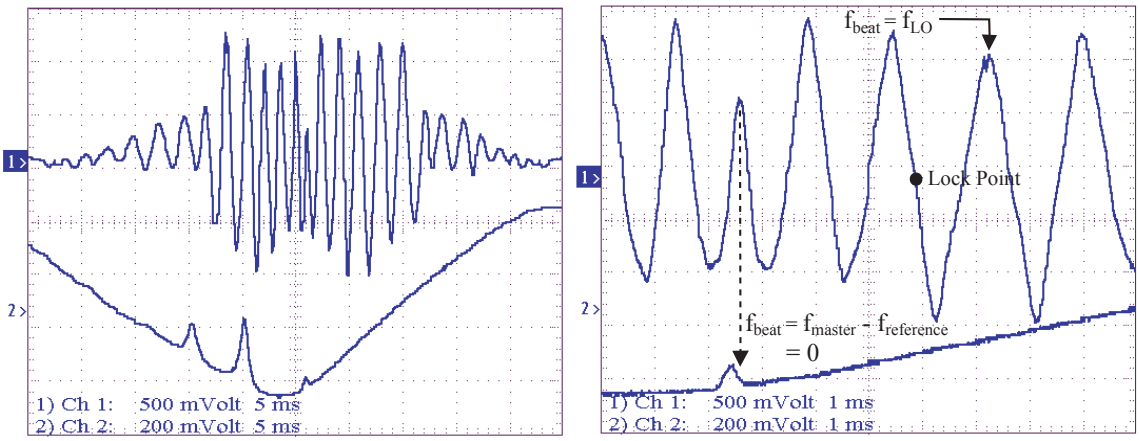

Figure 4.6 *Offset lock signal. The right image is an enlargement of the region close to the lock point. The scanned master laser frequency increases to the right. The reference laser is locked to a slightly higher frequency than the trapping transition, as indicated by the slight offset between the centre of the interference pattern and the saturated absorption feature.*

The two components are then input to a second mixer, which acts as a phase detector. The mixer takes the product of the two input signals, thus if the direct and delayed inputs are described by $\cos(2\pi ft)$ and $\cos(2\pi ft + \phi)$ respectively, the output is:

$$\begin{aligned} V_{mixer} &= \cos(2\pi ft)\cos(2\pi ft + \phi) \\ &= \frac{1}{2}\left(\cos(4\pi ft + \phi) + \cos(\phi)\right). \end{aligned} \tag{4.3}$$

The high frequency component is filtered out, leaving a dc signal proportional to the cosine of the relative phase:

$$\begin{aligned} V_{lock} &= V_0 \cos(\phi) \\ &= V_0 \cos((3\pi l/c)|f_{LO} - f_{beat}|) \\ &= V_0 \cos((3\pi l/c)|f_{LO} - |f_{master} - f_{reference}||). \end{aligned} \tag{4.4}$$

If f_{master} is scanned, the output signal scans over a set of interference fringes, centred on $f_{reference}$, as shown in Figure 4.6. This provides a signal with a set of zero-crossings to which we can lock. From Equation 4.4, it can be seen that the pattern is symmetric about both $f_{master} = f_{reference}$ and $f_{beat} = f_{LO}$. The saturated absorption spectrum provides a check of the exact reference laser frequency, Figure 4.6 (right). The low-pass filter limits the intermediate frequency, such that $|f_{LO} - f_{beat}| < 90\,\text{MHz}$, hence the interference pattern is truncated at these frequencies. The separation of the lock-points, given by $\delta\phi = 2\pi n$, corresponds to frequency

shifts of $\delta f_{master} = (2c/3l)n = 36n\,\mathrm{MHz}$. The absolute frequencies depend on the choice of f_{LO}, such that

$$\begin{aligned} |f_{LO} - f_{beat}| &= ((3\pi/2) \times 36 \pm 36n)\,\mathrm{MHz} \\ &= (25 \pm 36n)\,\mathrm{MHz}, \end{aligned} \tag{4.5}$$

for f_{beat} in the range $0 < f_{beat} < f_{LO}$. Once the master laser is locked to a particular zero-crossing, the local-oscillator frequency can be varied to shift f_{beat} and hence the frequency of the master laser.

The master laser beam passes through an AOM before seeding the injection laser, so that it can be rapidly switched on and off. This AOM operates at $-92\,\mathrm{MHz}$, therefore to produce resonant trap light from the slave laser, the master laser must be blue-detuned by 92 MHz above the reference laser frequency. Given also that f_{LO} is limited to frequencies in the range $64 \rightarrow 150\,\mathrm{MHz}$[1], the master laser is locked to an interference fringe corresponding to $|f_{LO} - f_{beat}| = 25$ MHz. For resonant trap light, $f_{beat} = 92\,\mathrm{MHz}$ and $f_{LO} = 118\,\mathrm{MHz}$. Varying f_{LO} over its full range tunes f_{master} over the range $+38 \rightarrow +124\,\mathrm{MHz}$ relative to the reference frequency. The AOM shifts this frequency range to $-54 \rightarrow +32\,\mathrm{MHz}$ relative to the trapping transition.

The electronic switch between the preset voltages of the VCO (f_{LO}) is sufficiently slow ($100\,\mu\mathrm{s}$) that the laser will remain locked for frequency jumps over its entire range, without re-locking to a different fringe. For the largest frequency jumps (54 MHz), the fast feedback to the laser current will bring the laser frequency to within 5 MHz of its final value within $100\,\mu\mathrm{s}$, after which the slow piezo feedback will bring it to its final value with a time constant of 5 ms.

4.1.6 Injection lock

The master laser beam is split into two beams. One is used for the imaging beam; the remaining 11 mW of light forms the 'seed' beam — this is injected into the slave laser, forcing the slave laser to lase at the same frequency. Since no grating is required for optical feedback, and no AOM is necessary for frequency switching, the maximum possible power is obtained from the slave laser: $\sim$60 mW.

Figure 4.7 shows a schematic of the injection lock optics. A Faraday rotator enables the seed light and injection laser output beam to be transmitted in opposite directions along the same path, while acting as an optical isolator for the slave laser beam at the same time. This device rotates the axis of polarization of a beam in the same sense, regardless of the beam direction. On leaving the laser, the vertically polarized slave beam is rotated 45° by a $\lambda/2$ waveplate. It then passes through

[1] The VCO has a range slightly greater than its specified $75 \rightarrow 150\,\mathrm{MHz}$

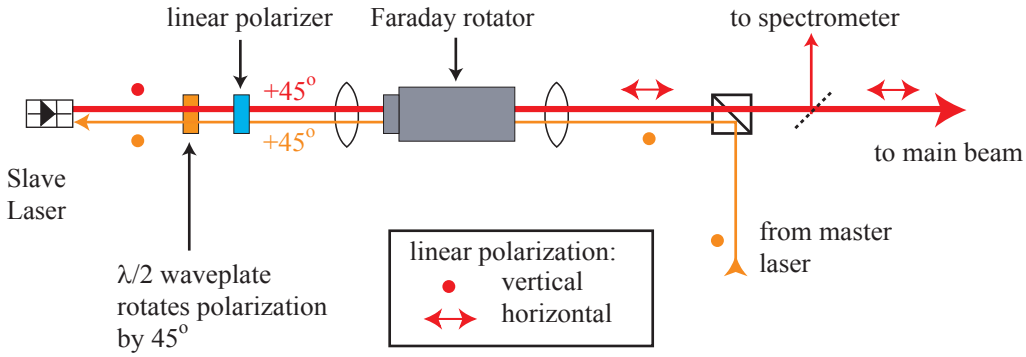

Figure 4.7 *Injection lock schematic. The Faraday rotator acts as an optical isolator for back-reflected light from the main beam (the polarization would be rotated a further 45° on second-pass through the Faraday rotator, so that it would be blocked by the linear polarizer), while allowing seed light from the master to be coupled into the slave laser with the correct polarization.*

a linear polarizer at 45° before being rotated a further 45° to horizontal by the Faraday rotator. It is then transmitted by a subsequent polarizing beam cube. The seed laser is vertically polarized and is coupled in by reflection at this beam cube. Its polarization will be rotated by the Faraday rotator, such that it is transmitted by the linear polarizer and is vertically polarized when it reaches the laser. However, any back-reflected slave laser light will be rotated in the same sense and then blocked by the linear polarizer.

Once the seed beam is well overlapped with the slave laser beam, it is a simple matter of increasing the slave laser current until it lases at the correct frequency. This is monitored using a saturated-absorption spectroscopy cell. The alignment of the seed light with the slave laser beam is critical: fine adjustments are needed to improve the single-mode frequency range. A useful technique for optimizing the alignment is to turn down the slave laser current to just below threshold for lasing. The seed beam alignment is then tweaked until the slave lases and this process is repeated until a minimum threshold current is reached. It is also necessary to adjust the temperature and current to optimize output power and scan range.

The free-running wavelength of the slave laser is 779.466 nm in air. This is sufficiently far from the trapping frequency (780.24 nm) that it is not necessary to have a means of fast switching the slave laser intensity on and off. Instead, the seed light intensity is switched on and off by an AOM — this causes the slave laser to revert to its free-running frequency in a time limited only by the AOM switching

time, $\sim 5\,\mu$s. At this frequency, the scattering rate for Rb from this laser is reduced by a factor of 10^{-8}, compared to the usual trapping frequency of -15 MHz below resonance. A shutter blocks the slave laser beam completely a millisecond or two later.

We find that the slave laser does not always relock to the master frequency after the seed light has been switched off. The optimum current for single-mode operation lies outside the capture range. Fine adjustments to the slave laser temperature can sometimes eradicate this problem; otherwise at the end of each experimental run, it is necessary to increase the current until the laser seeds, and then reduce it back to its optimum value. This can be done by computer control, using the current injection input of the laser current supply. A -5 V step gives a sufficient transient current ($\sim$1 mA) to return the slave laser to the master laser frequency.

4.1.7 Repump laser

The repump laser is essentially of the same design as the reference laser, except that a piezo disc rather than a stack is used to control the grating. The slow frequency part of the feedback signal is directed to the piezo disc via a high voltage amplifier. A polarization spectroscopy set-up is used to lock the repump laser to the $5\mathrm{S}_{1/2}\,F = 1 \rightarrow 5P_{3/2}\,F = 2$ transition. The polarization spectroscopy signal on this transition is much weaker than it is on the trapping transition. This difference is due to the trapping transition being a closed transition, whereas the upper level of the repump transition can decay to either of the hyperfine ground states. However, the difference signal still shows a small peak at the transition, marked (f) in Figure 4.8. We lock to the positive slope of this peak.

4.1.8 Optics

A variety of optics, AOMs and shutters are used to prepare the final beams which enter the vacuum chamber. A schematic of the optical table is shown in Figure 4.9. Periscopes are used to raise the height of the laser beams to $\sim$ 10 cm above the optical table. The lasers are protected by optical isolators against optical feedback from light reflected within the apparatus. This is particularly likely since the MOT laser beams are retro-reflected back towards the laser. The optical isolators are each followed by a $\lambda/2$ waveplate to reverse the 45° polarization rotation produced by the isolators.

All of the slave laser output intensity is used for the MOT trap beams. This is horizontally polarized after the Faraday rotator (see Section 4.1.6) and is combined with vertically polarized repump light at a polarizing beam cube. An anamorphic

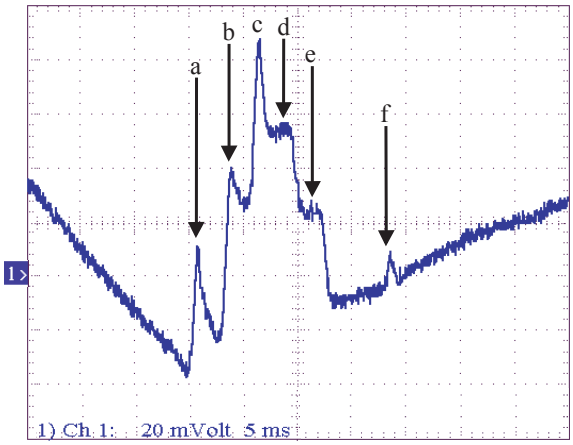

Figure 4.8 *Polarization Spectrum of the* $5S_{1/2}\,F = 1 \rightarrow 5P_{3/2}\,F'$ *transition of* ^{87}Rb. *((a):* $F = 1 \rightarrow F' = 0$*; (b): crossover* $F' = 0, 1$*; (c): crossover* $F' = 0, 2$*; (d):* $F = 1 \rightarrow F' = 1$*; (e): crossover* $F' = 1, 2$*; (f):* $F = 1 \rightarrow F' = 2$.*)*

prism pair is used to expand the beam in a ratio 3:1 from elliptical to circular. The transmission of these prisms is polarization dependent, so the beam polarization is first rotated by a $\lambda/2$ waveplate to maximize transmission. This beam is expanded to 1.5 cm diameter and then split into four beams. Two of these enter the chamber at 45 ° to the atom chip surface, as shown in Figure 2.2 such that each is reflected back along the other. The other two MOT beams counter-propagate horizontally through the centre of the chamber, orthogonal to the page of Figure 2.2. The horizontal beams are parallel to the atom chip surface and are partially clipped by the chip. The beams all cross orthogonally at the geometric centre of the vacuum chamber.

The MOT laser beams must all be circularly polarized σ^- relative to the local quadrupole field vector (see Section 2.1.2). The polarizations are set by $\lambda/4$ waveplates mounted on the vacuum chamber viewports, each with its fast axis at 45° to the linear polarization axis of the laser beam. Relative to the direction of propagation of each laser beam, the sense of circular polarization of the beam which passes through the anti-Helmholtz coil is opposite to that of the other beams (see Figure 2.1). The repump and trap beams were combined with orthogonal linear polarization, therefore the repump light of the MOT beams is circularly polarized in the opposite sense to the trapping light. This is unimportant since the ratio of scattering events involving repump photons is only about 1 in 500, as was estimated in Section 2.1.5.

Good alignment of the MOT beams through the chamber is critical for optimum

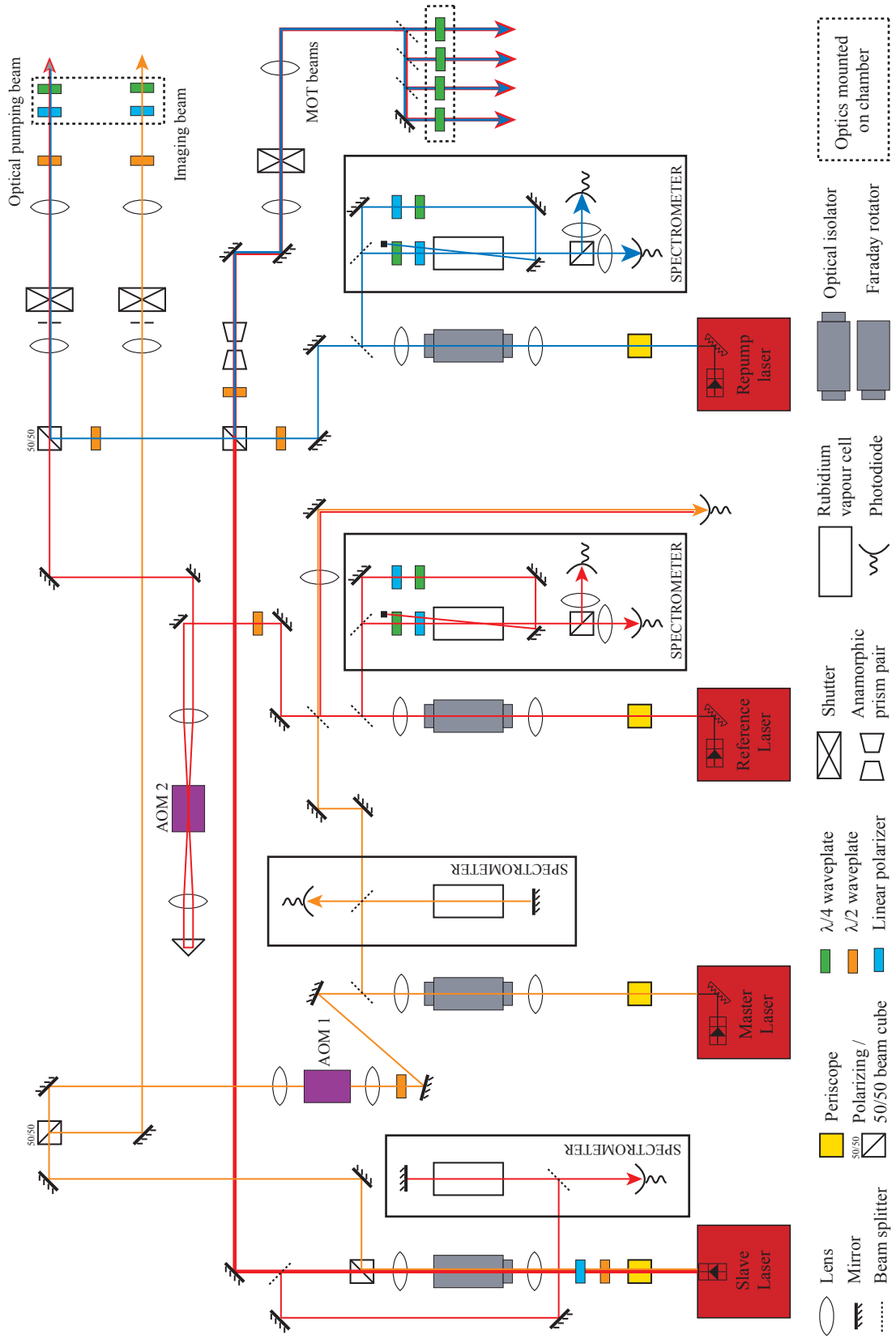

Figure 4.9 *The optics layout.*

performance of the experiment. The horizontal beams can be accurately aligned using apertures on the viewports of the chamber. It is more difficult to align the 45° beams, since the profile of the reflected beams is distorted by a slight bow in the atom chip surface. This makes it difficult to balance the beam intensities of the counter-propagating pairs. Additionally, the reflectivity of the atom chip surface decreases over time due to accumulation of a thin layer of a rubidium compound. This can be removed when the chamber is opened by carefully cleaning the surface with methanol.

Before expansion, the main beam has total power of 30 mW of trap light and 6 mW of repump light. The final beam intensities were measured using a calibrated $1\,\mathrm{cm}^2$ photodiode. The total trapping intensity at the MOT centre (including the reflected beams) is $30\,\mathrm{mWcm}^{-2}$.

Details of the imaging and optical pumping beam optics are given in the relevant sections (see Sections 4.4 and 6.1).

4.1.9 AOMs and shutters

It is necessary to be able to switch the various laser beams on and off with precise timing control and to vary the intensity also. This is achieved using AOMs, together with mechanical shutters. AOMs shift the optical frequency of a laser beam by diffracting the light from an acoustic wave inside an optical crystal [97]. They can also be used for intensity control since the amplitude of the acoustic wave controls the intensity of the diffracted beam. A VCO produces a radio-frequency (rf) signal which passes through a voltage-controlled attenuator before being amplified to create the acoustic wave inside the AOM. The frequency shift is controlled by the voltage to the VCO. Unless the beam is double-passed through the AOM (thereby doubling the frequency shift), the direction of the diffracted beam changes with frequency. Intensity control is achieved by varying the control voltage to the attenuator. In our experiment, this voltage can either be set manually by a potentiometer, or computer controlled by an electronic switch which selects between four preset voltage levels. Diffraction efficiency is maximized (to around 80%) by focusing the laser beam to a waist inside the AOM crystal.

Two AOMs are used in this experiment (see in Figure 4.9). AOM 1 (NEC AM 501) operates as a fast optical switch for the seed light, with a switching time of $5\,\mu$s. This effectively switches the MOT beam intensity on and off, since the slave laser immediately reverts to its free-running wavelength, which is many GHz detuned. A mechanical shutter is used to block the beam completely a few milliseconds later. This method does not allow continuous intensity control, simply on/off. This is a

slight disadvantage, since we would expect to obtain lower MOT or optical molasses temperatures by reducing the intensity of the trapping light. (The temperature of optical molasses scales as I/Δ, as discussed in Section 2.1.4). However, installing an additional AOM in the trap beam for this purpose would have reduced the maximum intensity by $\sim 20\%$. Instead, we rely on the capability to detune the trapping beams to a maximum of -54 MHz, by which we reduce the scattering rate sufficiently to reach reasonable temperatures for these experiments, as will be shown in Chapter 5. AOM 2 (Gooch and Housego M130-1E-US1) is used in a double pass configuration to shift the frequency of the reference laser beam by -267 MHz to the optical pumping transition.

The imaging and optical pumping beam intensities are controlled directly by AOM 1 and AOM 2 respectively. The intensities can each be switched between four preset levels, using two TTL lines under computer control. The shortest reproducible pulse length we use is limited by the timing accuracy of our computer control, about 50 μs. Scattering of light within the AOM crystal prevents total extinction of the first order beam, so when the light is to be turned off, each beam is also blocked by a mechanical shutter. The shutters (Newport 846HP) have a 3 ms switching speed. They are computer-controlled by a TTL edge, which must be triggered 5 ms in advance to account for a delay between trigger edge and shutter response. Vibration from the shutters affects the laser frequency, so Sorbothane sheet was used between the table and shutter mounts to help damp this effect.

A problem encountered using the AOMs is that it takes up to 2 s for the diffracted beam position and intensity to stabilize when the rf power is first switched on after a period greater than 100 ms. This is due to a thermal effect inside the AOM crystal. The problem is solved by switching the AOM rf power back on after the shutters have closed. A fourth shutter was then installed, to block the slave laser beam as close as possible to the laser. Since the AOMs are run continuously when the shutters are closed, the slave laser lases close to the trap frequency at high intensity. Despite considerable shielding, an extra shutter was necessary to prevent scattered light from reaching the vacuum chamber. This had been noticeably reducing the magnetic trap lifetime through excitation followed by decay to untrapped states.

4.2 Vacuum chamber

The vacuum chamber is based on a 6 inch diameter stainless steel sphere. Extending radially are 14 Conflat tubulated flanges, each welded to the sphere and arranged with cubic symmetry, as shown in Figure 4.10. The chamber is oriented such that an

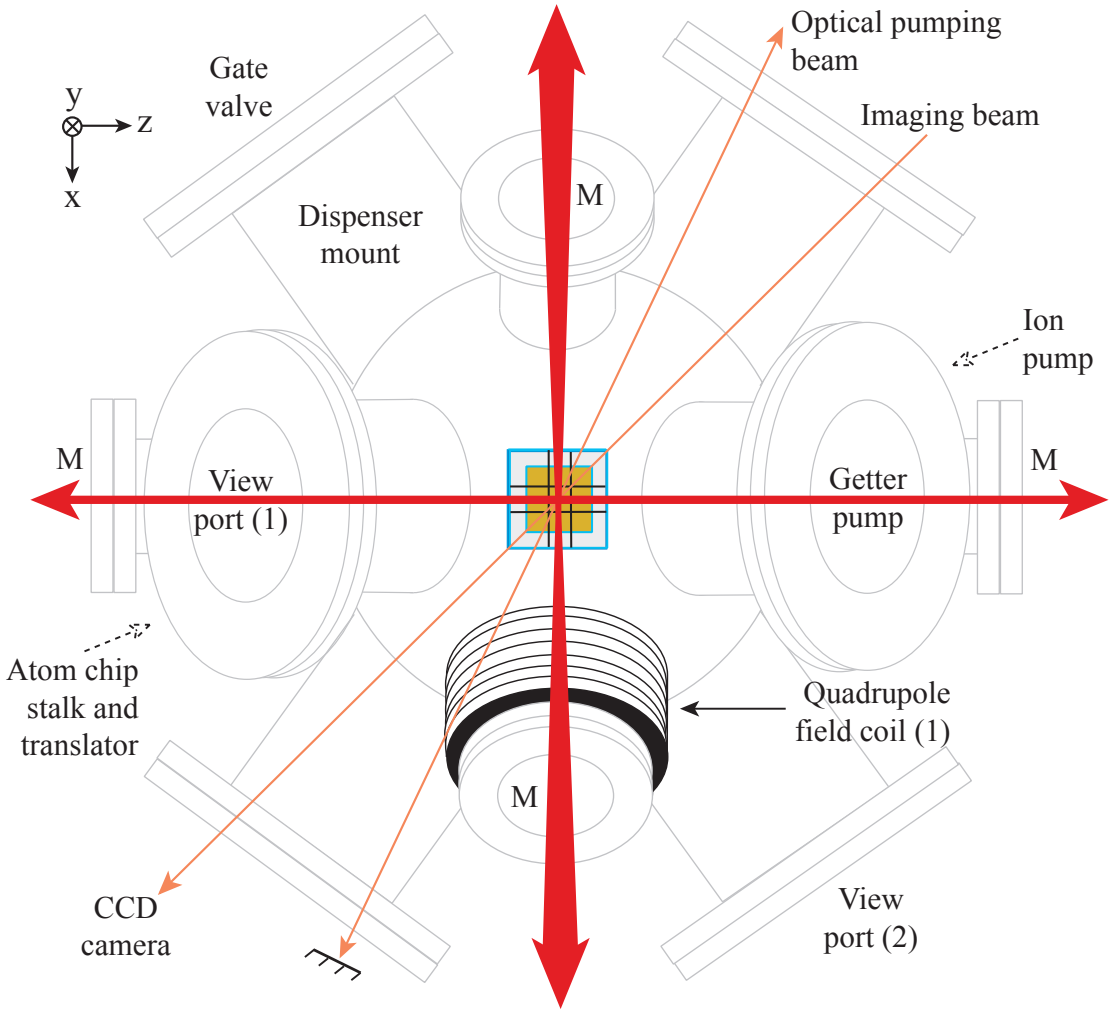

Figure 4.10 *Vacuum chamber, from below. The four MOT beams (red) enter and exit through the ports marked M. There are two more M ports diametrically opposite the upper two, which are no longer used. One of these holds the second quadrupole field coil. The horizontal MOT beams, imaging beam and optical pumping beam all lie in the horizontal x–z plane. In this plane, the angle between the large ports and the M ports is* 54.7°. *Diametrically opposite viewport (1) is the ion pump. The atom chip is mounted on a stalk from the port diametrically opposite the getter pump. The Rb dispenser is mounted across a steel cylinder, which fits inside the labelled port.*

edge of this cube is uppermost. Six of these tubes are $2\frac{3}{4}$ inches long and are located at the cube faces. They are each sealed by a $2\frac{3}{4}$ inch Conflat viewport with anti-reflection coated windows, marked 'M' in Figure 4.10. These are the entry windows for the MOT trapping beams. (Two are now unused, since the mirror-MOT requires only four beams.) The remaining eight tubes are $2\frac{1}{2}$ inches long and are located at the cube vertices. Four of these are sealed by $4\frac{1}{2}$ inch Conflat viewports. Two are the access and exit ports for the imaging and optical pumping beams; the other two can be used for viewing the MOT. Attached to the remaining four ports are the following: an ion-pump, a getter pump, a rubidium dispenser (see Section 4.3) with gate-valve, and the atom chip. The atom chip is mounted at $35\,^\circ$ onto a 23 cm long stalk attached to an xyz translator. The atom chip then hangs upside-down in the chamber with its surface horizontal.

The ion pump (Varian VacIon StarCell body, rebuilt with VacIon triode strip element) pumps at a rate of $60\,\mathrm{l\,s^{-1}}$. It has full wrap-around shields to reduce stray magnetic fields, which are further shielded by mumetal casing. The field component axial to the flange is the most difficult to shield and is the main contributor to stray magnetic field. This component is of the order of 0.5 G but the geometry of the pump causes it to be nearly constant over the volume of the chamber. Therefore it is possible to cancel this field with compensating coils outside of the chamber. The non-evaporable getter pump (SAES Getters GP50 St101) has a high surface area ($830\,\mathrm{cm}^2$) and doubles the rate of pumping for reactive gases. The vacuum pressure can be measured by the ion pump current, but only down to 10^{-9} Torr.

After each opening of the chamber, a careful bakeout procedure is followed, in order to attain the lowest possible pressure. The procedure is described in Appendix D. The final pressure is estimated to be of order 10^{-10} Torr.

4.3 Rb dispenser

Magneto-optical traps are generally loaded in one of two ways: either by capturing atoms directly from the low energy tail of a thermal vapour, or from an optically precooled source (for example, a Zeeman slowed beam [98], a double MOT system [99] or an LVIS [100]) operated in a pulse mode. The first method has the disadvantage that fast loading rates (which require a high partial pressure of rubidium) are incompatible with the stringent UHV requirements of long magnetic trap lifetimes. The pulsed method combines a fast loading rate with a long storage time for atoms, as the source can be switched off once atoms have been loaded. An inexpensive and experimentally simple way to implement pulsed loading is to use an alkali metal

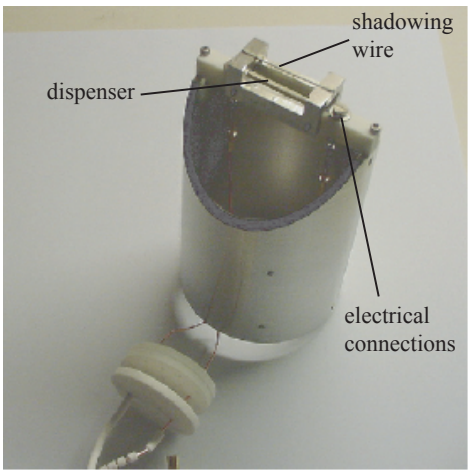

Figure 4.11 *Rubidium dispenser mount. At the top of the image the shadowing wire can be seen. The dispenser itself is mounted on an insulating block of MACOR, approximately 5 mm below this wire. Electrical connections to the dispenser are made via bare copper wires. The ceramic spacers (at the bottom of the picture) prevent them contacting the chamber.*

dispenser [101, 102].

The dispenser we use (SAES Getters RB/NF/3.4/25FT10+10)[103] contains rubidium chromate (Rb_2CrO_4) and a reducing agent, held within a nichrome metal container of trapezoidal cross-section. When resistively heated by a dc current supply, the reduction reaction is initiated above a threshold temperature of several hundred $^\circ$C. The rubidium metal vapour is emitted through a narrow slit on the front of the container. This slit is partially obstructed by a thin metal wire inside the metal package, to prevent escape of loose particles. The activation procedure for the dispenser is included in Appendix D.

Figure 4.3 shows the rubidium dispenser mounted on an insulating MACOR block with electrical connections. A 0.5 mm wire is positioned 5 mm in front of the dispenser; this serves to shadow the MOT from direct flux of hot rubidium atoms. This circular mount is inserted into a $4\frac{1}{2}$ inch port of the vacuum chamber, such that the dispenser rests horizontally, 3 cm from the MOT centre.

In daily operation, a current of 2.5 A is continuously run through the dispenser in order to keep its temperature close to the threshold temperature. To fill the MOT, a current of 8.5 A is pulsed through the dispenser for 10 s. The rubidium background pressure rises swiftly during this time, with a subsequent rapid increase in the fill rate of the MOT. After the current pulse, the dispenser cools quickly and switches

off. The rubidium partial pressure drops as atoms are adsorbed onto the walls of the chamber and removed by the pumps. The pressure takes about 6 s to recover fully, over which time we observe a gradual decrease in the MOT loss rate. Further details of the MOT loading procedure are given in Section 5.1.1.

4.4 Imaging system

All the data concerning clouds of atoms was collected by imaging them through a side viewport onto a CCD camera (Princeton Instruments RTE/CCD-768-k). This allows us to calculate the spatial density distribution of the atoms. Two methods are used: fluorescence imaging and absorption imaging. In the first, we simply collect the scattered light from the atom cloud in the presence of the MOT beams, as shown in Figure 4.12(a). In the second, a short pulse of light from the imaging beam passes through the atom cloud and is imaged onto the CCD array, as shown in Figure 4.12(b). The shadow of the cloud is recorded in the image. The camera and imaging lens positions remain the same for both imaging methods. Both fluorescence imaging and absorption imaging are destructive techniques: illuminating the atoms increases the cloud temperature and therefore only one image can be taken per experiment cycle. In this experiment, fluorescence imaging is used only to image the MOT: under these conditions, a series of fluorescence images can be collected in a single experimental cycle (for example, to measure the lifetime of the MOT), as this imaging process does not disturb the operation of the MOT.

A 1 inch diameter, 10 cm focal length achromat lens is used to image the atom cloud onto the CCD with unit magnification, $M = 1$. According to the Rayleigh criterion, the resolution limit in the plane of the atom cloud is $1.22\lambda f/D$, where $D = 2.54\,\text{cm}$ is the diameter of the imaging lens, $f = 10\,\text{cm}$ is the focal length and $\lambda = 780\,\text{nm}$ is the wavelength of the light. This gives a resolution of $7.5\,\mu\text{m}$.

The camera we use has a CCD chip of size $4.6\,\text{mm} \times 6.9\,\text{mm}$, which contains 512×768 pixels of size $9\mu\text{m} \times 9\,\mu\text{m}$. The camera is rotated by an angle of $30\,^\circ$ (see Figure 4.13 below), so in the object plane this corresponds to a field of view of $4.6\,\text{mm} \times 6.0\,\text{mm}$ and an effective pixel size of $9\mu\text{m} \times 7.8\,\mu\text{m}$. This is the theoretical limit on our resolution.

4.4.1 Calibration of the Princeton Instruments camera sensitivity

The camera is fitted with a mechanical shutter which can be triggered by an external TTL signal. From previous experiments [104], it was found that the shutter is not fully open until 7 ms after the trigger pulse. Therefore the camera is triggered 7 ms

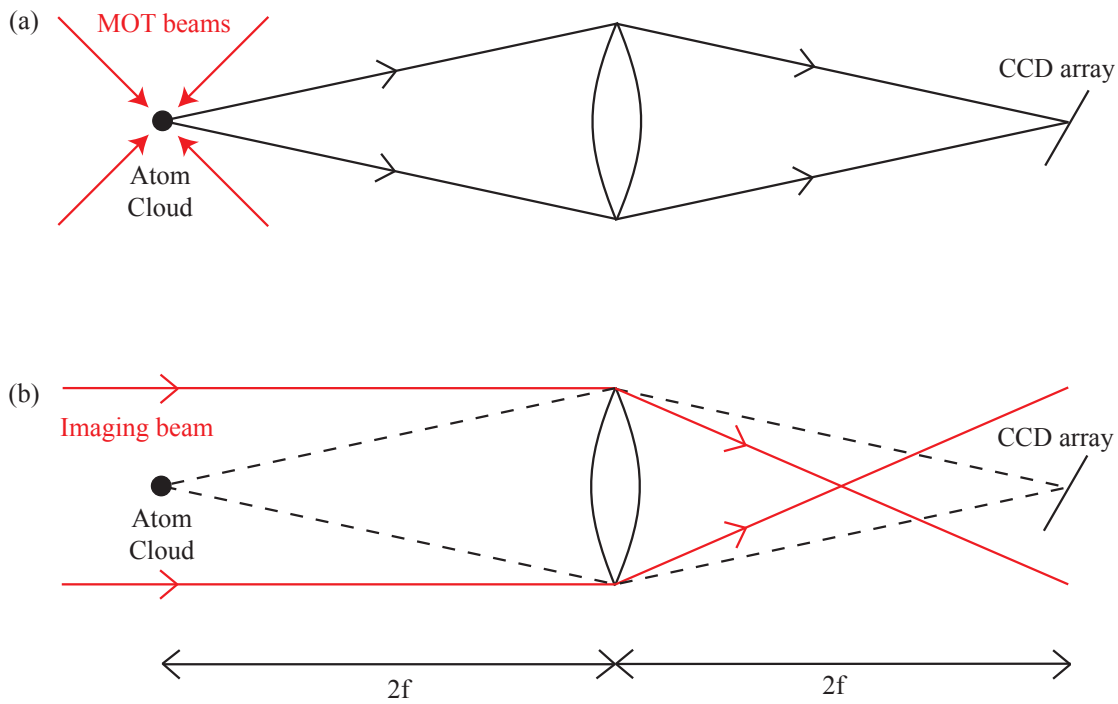

Figure 4.12 *Imaging system. (a) Fluorescence imaging: light emitted by the trapped atoms is imaged by the lens onto the CCD array. (b) Absorption imaging: a collimated beam passes through the atom cloud. A lens images the shadow formed by the atom cloud onto the CCD array.*

before an image is taken.

To calibrate the signal recorded on the chip, 650 nm light from a LED was imaged by a commercial zoom lens onto the CCD, for different shutter exposure times. This signal was integrated over the area of the image and plotted against programmed exposure time to calculate a total signal per millisecond exposure time. An independent measure of the power reaching the CCD was made using a calibrated photodiode. The measured calibration is $6.4 \times 10^{16}\, N_{P.I.}\, \mathrm{J}^{-1}$, where $N_{P.I.}$ is the integrated count using the units in which the Princeton Instruments camera software records the signal. This is within 1 % of the sensitivity calculated using the manufacturers specifications for this wavelength: $S(650\,\mathrm{nm}) = 0.019$ counts per photon. The specifications state equal sensitivity at 650 nm as for the 780 nm light used in this experiment, therefore $S(780\,\mathrm{nm}) = 0.019$ counts per photon.

The camera software adds a short 'compensation time' to the shutter opening time in order to compensate for the time during which the shutter is only partially open. From the previous experiment, we found that the effective exposure time is 2 ms longer than that programmed in the camera control software.

4.4.2 Imaging the MOT fluorescence

This method of imaging simply collects the light scattered from the atoms when illuminated by the MOT beams and forms an image on the camera CCD as shown in Figure 4.12(a). In addition to directly imaging the trapped cloud in the MOT, it is often useful to perform experiments where atoms are recaptured into the MOT to be imaged.

Atoms trapped in the MOT scatter light at a rate:

$$R(I,\nu) = \frac{\Gamma}{2}\frac{I/I_{Sat}}{1 + I/I_{Sat} + (2\Delta/\Gamma)^2}. \tag{4.6}$$

The atoms radiate isotropically: the fraction of this light collected by the imaging lens is equal to $\Omega/4\pi \approx r_{lens}^2/4d_{lens}^2$, where Ω is the solid angle which the MOT subtends at the imaging lens (radius r_{lens}, at a distance d_{lens}). To calculate the number of atoms present in the atom cloud we simply sum the number of counts over the area of the image. The number of atoms is given by:

$$N_{Atoms} = \frac{\sum_{image} N_{P.I.}}{R \times \tau_{exp} \times S \times \Omega/4\pi}, \tag{4.7}$$

where τ_{exp} is the effective camera exposure time, and $\Omega/4\pi \approx r_{lens}^2/4d_{lens}^2$ is the fraction of solid angle which the MOT subtends at the collection lens. r_{lens} and d_{lens} are the radius of the collection lens and its distance from the atom cloud respectively.

The value of I_{Sat} used in this calculation is $1.67\,\mathrm{mWcm^{-2}}$, the value for the stretched state transition $|F, m_F\rangle = |2, 2\rangle \rightarrow |F', m'_F\rangle = |3, 3\rangle$. In the MOT, the atoms are distributed over all possible m_F levels and experience light of all polarizations. Obtaining an effective saturation intensity for this multilevel system is not trivial. Assuming a uniform population of m_F sub-levels and averaging over the relative transition strengths for all transitions yields $I_{Sat}(\text{effective}) = 15/7 \times 1.67\,\mathrm{mWcm^{-2}}$. However, this is not in agreement with experiment [105, 106]. In [106], it is shown that for the $F = 2$ to $F' = 3$ transition of ^{87}Rb, the effective saturation intensity decreases from $4.2\mathrm{mWcm^{-2}}$ at a detuning of 6.5 MHz to close to the stretched state value at detunings greater than -12 MHz. This is understood to result from strong optical pumping effects which tend to populate the larger $|m_F|$ levels [105]. In the experiments described within this thesis, the MOT is operated at a detuning of -15 MHz and we use the saturation intensity of the stretched state in calculations of the MOT number.

Fluorescence imaging has several further limitations as a technique for giving accurate information about atom number and cloud profile. The MOT beams are not spatially filtered, nor is the atom chip a perfect mirror: therefore it is difficult to know the exact intensity at any point of the MOT. In addition, the solid angle subtended by the MOT at the lens is cut off by the atom chip, by an amount which varies with height above the chip. Combined, these two effects lead to uncertainties in calculations based upon the image intensity. Absorption imaging is not plagued by these problems, so can give more accurate information about the density distribution of an atom cloud.

4.4.3 Absorption imaging

In this method, a weak imaging beam is shone through the cloud of atoms. The atoms scatter this light according to Equation 4.6. The absorbed light has a well-defined direction whereas the spontaneously re-radiated light is randomly distributed over all possible directions. Because the cloud can be optically thick, this method can have very good statistical sensitivity.

The imaging beam used for absorption imaging is derived from the master laser and is tuned to the $F = 2 \rightarrow F' = 3$ transition. It is spatially filtered by a 500 μm pinhole and expanded to 1.5 cm diameter to give uniform illumination over the region of interest. Immediately before entering the chamber it passes through a linear polarizer and $\lambda/4$ waveplate, oriented so as to circularly (σ^+) polarize the beam. Normally the atoms are released from the trap before imaging and a small (1.7 G) bias field is applied along the direction of the imaging beam. Atoms are then

pumped relatively quickly into the $|F, m_F\rangle = |2, 2\rangle$ ground state, from which there is only one possible transition: $|F, m_F\rangle = |2, 2\rangle \rightarrow |F', m'_F\rangle = |3, 3\rangle$. This is the transition for which the scattering rate is a maximum and $I_{Sat} = 1.67\,\mathrm{mW\,cm^{-2}}$.

For an imaging beam of intensity I_0 (where $I_0 \ll I_{Sat}$), travelling along the x' axis, the atom cloud absorbs light according to the Lambert-Beer law, such that the intensity distribution after passing through the cloud is :

$$I(y', z') = I_0(y', z') \exp(-\sigma_L \int n(x', y', z')\,\mathrm{d}x'), \tag{4.8}$$

where $n(x', y', z')$ is the atomic number density and σ_L is the photon absorption cross-section:

$$\sigma_L = h\nu \frac{\Gamma}{2} \frac{1/I_{Sat}}{1 + I/I_{Sat} + (2\Delta/\Gamma)^2}. \tag{4.9}$$

To extract quantitative information about the atom cloud, the ratio $I(y', z')/I_0(y', z')$ is required. This is obtained by taking a sequence of three images: first, an absorption image I1 is taken of the atom cloud; a second image I2, using the same imaging intensity and pulse length is taken after the atom cloud has fallen out of the field of view of the camera; finally a background image, I3, is taken without the atom cloud or the imaging beam. The images are processed using the Princeton Instruments camera software to give a single image, (I1 − I3)/(I2 − I3). By taking the natural log of this image, we obtain a final image with intensity distribution:

$$\ln(I(y', z')/I_0(y', z')) = -\sigma_L \int n(x', y', z')\,\mathrm{d}x' = -\text{Optical density}. \tag{4.10}$$

The total number of atoms, N, can be calculated by summing this final image intensity over the area of the atom cloud:

$$N = -\sum_{image} (\ln(I(y', z')/I_0(y', z')) \times (\text{area represented by pixel in image plane}) \times \frac{1}{\sigma_L}. \tag{4.11}$$

Equivalently, a fit to the profiles can be used to determine the total atom number. The clouds we image are often well described by a Gaussian distribution:

$$n(x, y, z) = n_0 \exp\left(-\left(\frac{x^2}{2\sigma_x^2} + \frac{y^2}{2\sigma_y^2} + \frac{z^2}{2\sigma_z^2}\right)\right), \tag{4.12}$$

where

$$n_0 = \frac{N}{(2\pi)^{3/2}\,\sigma_x \sigma_y \sigma_z} \tag{4.13}$$

is the peak density and σ_i is the standard deviation of the cloud. The imaging beam effectively integrates the cloud density along the x' direction, giving a '2D' atomic

density, $\int n(x', y', z')\mathrm{d}x'$. Gaussian fits to the profiles of Equation 4.10 yield values for the peak '2D' atom density and for $\sigma_{y'}$ and $\sigma_{z'}$. The total number of atoms is given by:

$$N = \max\left(\int n(x', y', z')\mathrm{d}x'\right) \times 2\pi\sigma_{y'}\sigma_{z'}. \tag{4.14}$$

The intensity and pulse length of the imaging beam are chosen to give a good signal to noise ratio, while minimizing the diffusion of the cloud caused by light scattering. The absorption signal is proportional to the number of photons scattered per atom, $N_p = R(I, \nu)\tau_{pulse}$, where τ_{pulse} is the length of the imaging pulse. Each scattered photon imparts a momentum mv_{recoil} to each atom, where m is the atomic mass and the recoil velocity, v_{recoil}, is $5.9\,\mathrm{ms}^{-1}$. Successive scattering events result in the atom following a random walk in three-dimensional momentum space. After scattering N_p photons, the rms momentum imparted transverse to the line of sight is therefore $\sqrt{N_p/3}\,mv_{recoil}$. Integrating over the length of the imaging pulse gives a transverse displacement:

$$\int_0^{\tau_{pulse}} \sqrt{R(I, \nu)\tau/3}\, v_{recoil}\,\mathrm{d}\tau = \frac{2}{3\sqrt{3}}\, v_{recoil}\,\sqrt{R(I, \nu)}\,\tau_{pulse}^{3/2}. \tag{4.15}$$

To maximize the absorption signal ($\propto R(I, \nu)\tau_{pulse}$) while minimizing diffusion ($\propto R(I, \nu)^{1/2}\,\tau^{3/2}$) it is therefore preferable to use a high imaging intensity and a short pulse length. In our experiment, we use the shortest reliable pulse length generated by the computer control program, $50\,\mu$s. An intensity of $0.6\,\mathrm{mWcm}^{-2}$ is chosen so that the total energy in the imaging pulse is just below that required to saturate the CCD array. (The full well depth of the camera is specified as 85,000 electrons and the quantum efficiency is 40% at 780 nm — i.e. up to 34,000 photons can be recorded per pixel.) This gives the greatest dynamic range for the absorption signal. Each atom scatters about 50 photons during imaging. The transverse atom displacement is $1\,\mu$m, much smaller than the limit of resolution.

Sometimes, it is useful to image the atoms without turning off the magnetic trap, for example to measure its position. In this case, the imaging beam cannot be circularly polarized with respect to the local magnetic field because the field direction varies with position in the trap. Each atom then sees a different polarization depending on its location within the trap and the resultant scattering rate is reduced. This can lead to strange distortions of the image due to the optical activity of the cloud. In addition, if the temperature of the cloud is greater than the natural linewidth, the magnetic trapping potential tunes the atoms in and out of resonance. In this way, different imaging beam detunings give rise to images with different profiles [107].

The absorption images show interference fringes, mainly due to multiple reflections between the surfaces of the vacuum chamber windows. These are removed when the first absorption image I1 is divided by image I2, so long as the fringes have not shifted. Therefore, any vibration of the camera or beams must be damped, particularly that due to the camera shutter. Layers of Sorbothane are used to isolate the camera and other mechanical shutters from the optical table. Even with these precautions, it is still necessary to make the time interval between the two images as short as possible. In our experiment, this is limited to 100 ms by the read out time of the camera. (This time can be reduced by using a CCD chip which is divided into two areas. Only one half is exposed: the recorded signal is then shifted onto the shielded half for storage, before the second image is taken. The two images are then read out together. The time taken for charge transfer across the chip is shorter than the whole image read out time by a factor equal to the number of lines of pixels.)

Inside the camera, the CCD is positioned in vacuum behind a thin window. Multiple reflections of the imaging beam from this window lead to strong interference fringes in the image. These do not divide out well, since vibrations due to the shutter cause them to shift between images. Rotating the camera through 30 ° as shown in Figure 4.13 removes this effect.

4.4.4 Transformation of coordinates

We are interested mainly in long thin magnetically trapped clouds which are roughly cylindrical along the z-axis as shown in Figure 4.13. The imaging beam passes through the chamber at $\theta = 45°$ to this axis. Furthermore, the camera is rotated to $\theta' = 30°$ relative to the imaging beam. Therefore, a transformation of coordinates is necessary to relate the CCD image to the physical cloud. Using the coordinate representation of Figure 4.13, the transformation from the 2D frame of the camera ($y''z''$), via the imaging frame ($x'y'z'$), to the frame of the magnetic trap (xyz) is given by:

$$z' = -z'' \cos\theta', \qquad y' = y'',$$
$$x = x' \cos\theta + z' \sin\theta, \qquad y = y', \qquad z = -x' \sin\theta + z' \cos\theta. \tag{4.16}$$

The two dimensional projection of a Gaussian atomic density distribution into the imaging plane ($y'z'$) is also Gaussian, with modified width parameters [106]:

$$\sigma_{y'} = \sigma_y \qquad \sigma_{z'} = \sqrt{\sigma_z^2 \cos^2\theta + \sigma_x^2 \sin^2\theta}. \tag{4.17}$$

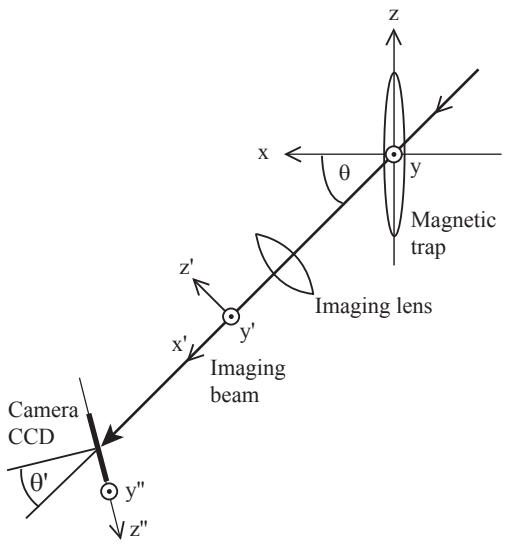

Figure 4.13 *Transformation of coordinates from magnetic trap to imaging plane. The imaging beam passes through the atom cloud at an angle $\theta = 45°$ to the z-axis of the magnetic trap. The camera is rotated through $\theta' = 30°$ relative to the imaging beam, to avoid interference due to multiple reflections within the camera.*

Approximating the distribution to be cylindrically symmetric about the z-axis, i.e. $\sigma_x = \sigma_y$, we obtain the axial width of the trapped cloud:

$$\sigma_z = \frac{\sqrt{\sigma_{z'}^2 - \sigma_{y'}^2 \sin^2\theta}}{\cos\theta}. \tag{4.18}$$

Finally, we have expressions for the cloud widths in terms of the CCD images:

$$\sigma_z = \frac{\sqrt{\sigma_{z''}^2 \cos^2\theta' - \sigma_{y''}^2 sin^2\theta}}{\cos\theta}$$
$$\sigma_y = \sigma_{y''}. \tag{4.19}$$

These transformations allow the peak density to be obtained from Equation 4.13.

4.5 Magnetic fields and current control

Many pairs of magnetic field coils are employed throughout the experiment, in particular, to provide the MOT field gradient and the bias field which produces the magnetic tube traps in conjunction with the atom chip.

4.5.1 External bias fields

All the external bias fields are created using pairs of circular or rectangular 'Helmholtz' coils. These carry current in the same sense and produce a uniform axial field at

their midpoint.

The field arising from a pair of coils is calculated from the Biot-Savart Law:

$$\mathrm{d}\mathbf{B} = \frac{\mu_0 I}{4\pi} \frac{\mathrm{d}\mathbf{l} \times (\mathbf{r} - \mathbf{r}')}{|\mathbf{r} - \mathbf{r}'|^3} \tag{4.20}$$

where $\mathrm{d}\mathbf{B}$ is the magnetic field generated at the point $\mathbf{r}$ by a current element at $\mathbf{r}'$ with current I and length $\mathrm{d}\mathbf{l}$.

Consider a rectangular pair of coils, with sides of length a and b, and separation c, with the axis of the coils along $\hat{\mathbf{z}}$. Integrating along each edge of the rectangular coils and summing all the contributions leads to an expression for the resultant magnetic field. In units of Gauss and centimetres, the axial field at the mid-point is given by:

$$\mathbf{B} = \frac{8NI}{5} \frac{ab(a^2 + b^2 + 2c^2)}{(a^2 + b^2)(b^2 + c^2)\sqrt{a^2 + b^2 + c^2}} \hat{\mathbf{z}}. \tag{4.21}$$

Circular coils of diameter d cm and separation s cm give an axial field (in Gauss) described exactly by:

$$\mathbf{B} = \frac{2\pi N I d^2}{5} \left(\frac{1}{(d^2 + 4z^2)^{3/2}} + \frac{1}{(d^2 + 4(s - z)^2)^{3/2}} \right) \hat{\mathbf{z}}. \tag{4.22}$$

For both square and circular coils, there is a condition for which the second derivative of the field w.r.t. z is zero. For square coils, this is $c = 0.5445a$; for circular coils this is $s = d/2$. The field is then spatially uniform to fourth order at the centre, since the field must necessarily be symmetric. This is the true 'Helmholtz' arrangement. In practice, the layout of the experiment requires the coil separation to differ from these ideal values — see Table 4.1 for specific values. This limits the volume over which the field can be considered uniform, but this is not significant over the region in which atoms are trapped.

The vacuum chamber is surrounded by a cuboid formed from three pairs of rectangular coils which serve to cancel the magnetic field of the Earth and other stray fields. Before closing the chamber, a magnetometer was used to measure the field at the centre of the chamber while adjusting the currents in these coils to correctly cancel all components of the field to zero. Each pair of coils is overwound with a second set, which can independently be used to apply additional bias fields up to a maximum of 1.2 G.

The bias field for the magnetic traps is generated by a double pair of rectangular coils. These are wound on open frames so as not to generate eddy currents when the fields are switched rapidly. A separate power supply is connected to each pair in order to provide sufficient current to produce the high bias fields (up to 50 G)

required for the microtraps. The two currents are regulated by separate circuits (Section 4.5.3) but determined by a single control voltage, i.e. the currents are always related by a constant factor. For the purpose of calibrating the bias field, the coils can therefore be treated as a single pair.

Two pairs of small circular coils are wound onto ports of the vacuum chamber. The first pair (wound on the viewports through which the horizontal MOT beams enter) provides a field along the z-axis which is used to cancel the field at the centre of the magnetic tube traps (see Section 2.3.4). The second pair is wound onto the ports through which the optical pumping and imaging beams pass. This field defines the quantization axis for imaging, parallel to the direction of propagation of the light.

Details of all the magnetic field coils are summarized in Table 4.1. The calibration stated for the axial cancelling field was obtained using a radio-frequency technique to measure the minimum field of the magnetic trap — this will be described in Section 6.7. The discrepancy between calculation and measurement suggests that either this is not a reliable technique, or that the contributions to the axial field are not well understood.

4.5.2 Quadrupole field

The quadrupole field for the MOT is produced by a pair of circular 'anti-Helmholtz' coils. These carry current in opposite directions such that the magnetic field increases linearly from zero at the centre. The MOT coils have 480 turns and are wound on water cooled formers, designed to fit over two of the MOT beam entry ports as shown in Figure 4.10. When the coils are separated by a distance $\sqrt{3}d/2$, where d is the diameter of the coils, this yields a quadrupole field linear in z to fifth order at the midpoint. Due to the physical constraints of our chamber, the coils we use have a diameter of 9 cm and a separation of 17 cm. The magnetic field grows very nearly linearly with displacement from the origin — the deviation from linear is less than 10% over the range ± 2 cm from the MOT centre. This region is much greater than the 1 mm diameter of the MOT cloud. For a current of 4 A, the resulting gradient is $15\,\mathrm{G\,cm^{-1}}$ along the axis of the coils and $7.5\,\mathrm{G\,cm^{-1}}$ orthogonally.

		Dimensions	Separation	Turns	Calculated field	Calibration
Bias field, B_{bias}	(1)	33 cm × 33 cm	25.5 cm	45	1.7 G A^{-1}	
	(2)	33 cm × 33 cm	25.5 cm	101	3.65 G A^{-1}	
Earth's field cancellation	(x)	60 cm × 59.5 cm	43.5 cm	15	330 mG cm^{-1}	346 mG A^{-1}
/Additional bias fields	(y)	43.5 cm × 62.5 cm	66 cm	15	185 mG cm^{-1}	210 mG A^{-1}
	(z)	43.5 cm × 62.5 cm	62.5 cm	15	200 mG cm^{-1}	195 mG A^{-1}
Axial bias field (to cancel field of end wires)		8 cm diameter	16 cm	100	2.8 G A^{-1}	3.83 G A $^{-1}$
Quantization field (for imaging)		7 cm diameter	15 cm	6	0.16 G A^{-1}	
Quadrupole field (MOT) (typical current = 4 A)		9 cm diameter	17 cm	480	15 G cm^{-1} 7.5 G cm^{-1}	

Table 4.1 *Summary of magnetic field coils. The main bias field, B_{bias}, is produced by a two similar pairs of coils. The Earth's magnetic field cancellation coils and additional x, y and z bias coils are wound on the same formers, with 15 turns each. The calibration of the xyz bias coils was made using a gaussmeter at the centre of the vacuum chamber before it was closed. The calibration of the axial bias field coils was made using the technique described in Section 6.7*

.

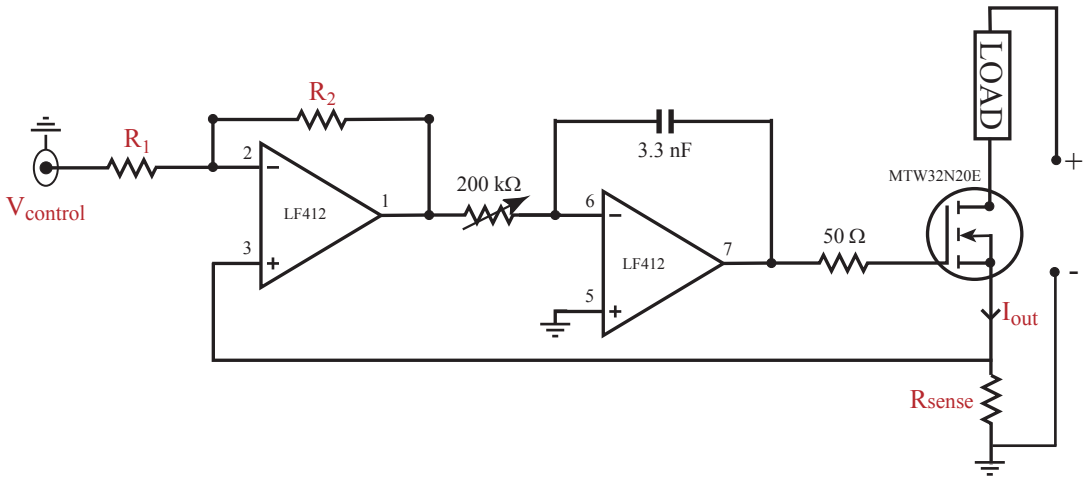

Figure 4.14 *Current control circuit. R_{sense} is 0.1 Ω for the wire currents of the atom chip, 0.5 Ω for the bias field coils.*

4.5.3 Current control

The currents in the atom chip wires and bias field coils must be ramped smoothly in time to compress and shift the magnetic traps. These currents must also have minimal noise, particularly at frequencies close to the trap frequencies, since this leads to heating of the trapped atom cloud and additional atom loss rates.

The currents are supplied by Isotech switch-mode power supplies[2], regulated by the FET circuits shown in Figure 4.14. The sense resistor must have a small value (typically 0.1 Ω) in order not to limit the maximum current output of the power supplies. The control voltage, $V_{control}$, is typically between 0 and 10 V. I_{out} is fixed relative to $V_{control}$ by R_1 and R_2 to allow the required output current range.

The currents in the end wires and the axial field cancelling coils are controlled by preset input voltages to the FET circuit. For each, two TTL lines from the computer are used to select between four preset voltages (for circuit diagram, see Figure E.1 in Appendix E). The additional pairs of x, y, z bias coils are controlled using identical FET circuits but with only one current setting, using a single on/off TTL line.

The currents in the centre wire and main bias field coils must follow more complex patterns, including ramps, which are beyond the capabilities of our present computer control software. Two function generators are used (Stanford Research Systems DS345) which can be programmed with arbitrary waveforms. Up to 16,384 points

[2]ISO-TECH IPS 1820D (18 V, 20 A)/3610 (36 V, 10 A)/IP606D (60 V, 6 A); ripple and noise specified at < 5 mV rms in constant voltage mode.

can be stored: for a 16 s waveform, this gives a timing resolution of 1 ms. The function generators have an output voltage range of ±5 V. To make use of the full voltage range, 5 V is added to this output before it is input to the FET control circuit (Figure E.1).

If the control voltage $V_{control}$ drops even slightly negative, the gate voltage of the FET will be driven by the integrator to −15 V. In this case, when the input voltages are switched on, it can take several milliseconds for the integrator to bring the gate voltage back up to the range where the FET will switch on, particularly if the initial set current is low. To prevent this situation, a small voltage (0.5 mV) is added to each of the input voltages before the FET circuit (see Figure E.1), so that $V_{control}$ is always slightly positive. With this modification, the FET circuit is always active, regulating a small current, $\sim$ 0.1 mA even when 'off'. The circuit then responds immediately to the control voltage.

A large current range is required for each circuit — the power supplies must therefore be set to a sufficiently high voltage to supply the maximum current when required. The FETs must therefore be capable of dissipating high power when the circuits are run at intermediate currents. The FETs we use are MTW 32N20E, with a maximum rating of 32 A/180 W at 25 °C. To provide further heatsinking, the FET circuits themselves are built on a water-cooled copper heatsink.

The final point to note is that the bias coils are an inductive load, which prevents fast switching of large currents. The currents in the atom chip wires can be switched on and off in $\sim$ 100 μs. In contrast, the bias field currents have a rise time of 2.5 ms. This can be improved by setting the power supplies at a voltage higher than required, which allows a higher current to flow at early times, when the coils have a high back emf. This however leads to overshoot of the final current, which is corrected at the response time of the current control circuit, $\sim$ 100μs. In this experiment, we avoid switching the bias field on and off rapidly — the slow switching time is not a problem when the fields are ramped over several tens of milliseconds.

4.5.4 Radio-frequency field

The rf antenna used for evaporative cooling is formed by the two additional wires of the atom chip. These are parallel with the centre wire and separated by 8 mm. They are connected internally in series, such that current flows in a loop. An oscillating current is driven in these wires by a function generator, connected to the vacuum chamber feedthrough by a length of coaxial cable and a 2.7 Ω sense resistor. The function generator used (Stanford Research Systems DS345) has internal linear and exponential frequency sweeps, which are used to ramp the rf signal between

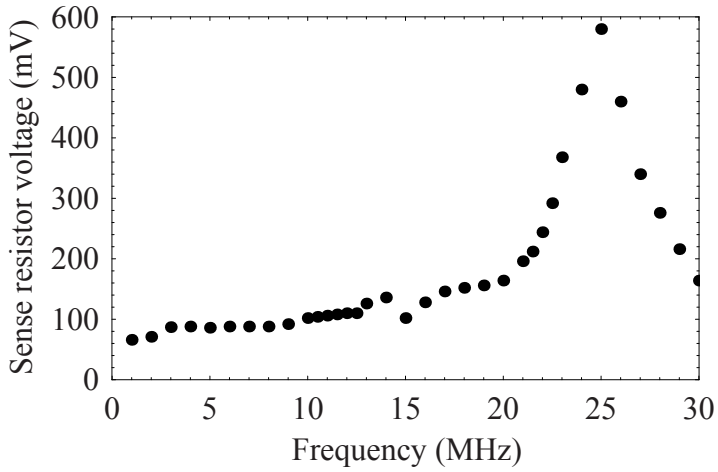

Figure 4.15 *Current in the rf circuit measured as voltage amplitude across the sense resistor versus frequency of the fixed drive voltage.*

two frequencies at a programmable rate. The amplitude of the output voltage is controllable via an external input, so that it can be switched off during the trap loading stages and switched on only when the rf ramp is triggered.

We initially measured a resonance of the rf loop at a frequency of 11.5 MHz, with a Q-factor of 8. At this point the circuit included a 2.5 m length of coaxial cable, having a capacitance 100 pF m^{-1}. Since $f = 1/2\pi\sqrt{LC}$ for an LC circuit, the resonance can be shifted to higher frequencies by decreasing the capacitance of the circuit. Simply shortening the coaxial cable to the absolute minimum (0.5 m) shifted the resonance from 11.5 MHz to 24 MHz. Figure 4.15 shows the resonance at 24 MHz. The range of frequencies used for evaporative cooling is from 20 MHz down to a few kHz. The response of the circuit is now approximately flat over this range, as shown in Figure 4.15. The magnitude of the oscillating field is calculated to be of the order of 40 mG in the trapping region.

4.6 Computer control of the experiment

We use a 386 IBM PC running a Pascal program[3] to control the TTL outputs of a 32-bit data acquisition boards (Amplicon PC214E). When an experimental sequence is run, the computer drives a time-varying pattern of TTL voltages for these outputs. The 32 TTL lines are fed (via a 50 Ω line driver buffer circuit) to various electronic circuits which control the offset-lock frequency, shutters, AOMs, atom chip currents

[3]The control program was written by Ben Sauer, University of Sussex.

and magnetic fields and trigger the function generator waveforms and the Princeton camera data acquisition cycle. The shortest pulse length we use is $50\,\mu$s, which is repeatable within $\pm 2\mu$s. Table 4.2 shows the function of each output.

	Line	Function
A1	0	Imaging beam shutter: {Open, Closed}
	1	Princeton Instruments camera trigger
	2	MOT/Imaging beam detuning:
	3	{−18 MHz, −34 MHz, −45 MHz, 0 MHz}
	4	Quadrupole field: {Off, On}
	5	MOT beam shutter: {Open, Closed}
	6	Imaging beam/seed light intensity:
	7	{Off, $\frac{1}{4}$, $\frac{1}{2}$, Full}
B1	0	Rb dispenser current:
	1	{0 A, 5 A, 2.5 A, 8.5 A}
	2	Bias field B_{bias}: {Off, On}
	3	Centre wire current I_{centre}: {Off, On}
	4	End wire current I_{end}:
	5	{0 A, 10 A, 15 A, 20 A}
	6	Axial field cancelling coils:
	7	{0 A, 0.5 A, 0.75 A, 1 A}
A2	0	Function generator trigger
	1	Optical pumping beam shutter: {Open, Closed}
	2	Imaging/optical pumping quantization field: {Off, On}
	3	Optical pumping AOM: {Off, On}
	4	rf function generator trigger (for evaporative cooling ramp)
	5	x-Bias field: {Off, On}
	6	z-Bias field: {Off, On}
	7	Slave laser beam shutter {Closed, Open}
B2		Unused

Table 4.2 *Functions of computer controlled TTL outputs. For convenience, the 32 lines are grouped in blocks of 8. The values in brackets indicate the settings corresponding to the TTL outputs {0,1} (for a function controlled by a single TTL line) or {00,01,10,11} (double TTL line), where 0≡Lo and 1≡Hi.*

Chapter 5

MOTS, MOTS, MOTS

This chapter describes the operating conditions for the mirror-MOT and compressed MOT. The mirror-MOT enables atoms to be trapped and cooled directly above the atom chip surface. Compressing the MOT increases its density and enables it to be mode-matched into the long, thin magnetic trap formed by the centre wire and bias field. The final section of this chapter describes an earlier experiment in which we loaded atoms directly from a mirror-MOT into an array of microMOTs formed above the videotape surface.

5.1 Mirror-MOT

The principles of the mirror-MOT and the experimental set-up have been described in Section 2.1.3 and in the previous chapter. Here, we discuss the optimization and characterization of the MOT loading process.

5.1.1 Loading the mirror-MOT

The mirror-MOT is loaded by pulsing a current in the rubidium dispenser. The loading rate of the MOT (assuming atomic density dependent losses [53, 108] are negligible) is described by:

$$\frac{\mathrm{d}N}{\mathrm{d}t} = R - N/\tau \tag{5.1}$$

$$= \alpha\Phi - N(\beta\Phi + \gamma), \tag{5.2}$$

where N is the number of trapped atoms and Φ is the flux of rubidium into the trapping region. The first term, R, describes the rate of capture of rubidium atoms, with α being a capture cross-section for atoms entering the trapping region. The

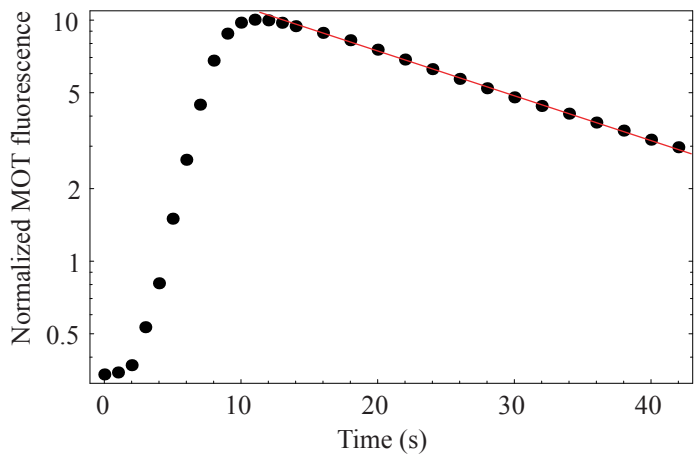

Figure 5.1 *Fill and decay curve of mirror-MOT atom number. The dispenser is pulsed on at 8.5 A from 0 to 10 s. The maximum MOT fluorescence corresponds to* 7.6×10^7 *atoms in the MOT. A* $1/e$ *lifetime of 23.4 s is deduced from the exponential fit to the decay.*

lifetime τ, for loss of atoms from the MOT, is due to two processes: $\beta\Phi$ is the loss rate due to collisions with fast rubidium atoms and γ is the loss rate due to collisions with other background gases. The equilibrium number of trapped atoms for a particular flux rate of rubidium is:

$$N_{equ} = \frac{\alpha\Phi}{\beta\Phi + \gamma}. \tag{5.3}$$

When the dispenser current pulse is switched on at 8.5 A, the dispenser heats up over several seconds, with the emitted rubidium flux increasing with temperature. The overall effect is to rapidly increase the partial pressure of rubidium in the vacuum chamber. Once the flux of rubidium has increased sufficiently, we can neglect the effect of other background gases in Equation 5.1 and we see that $N_{equ} = \alpha/\beta$. This is the rubidium dominated regime, where N_{equ} is independent of the flux of rubidium. Once in this regime, the effect of further increasing the rubidium flux is simply to increase the loading rate, but not the final number of atoms in the MOT. Since it takes a finite time for the pumps to reduce the pressure to its initial background level after the dispenser is switched off, it is advantageous to run the dispenser at a lower current for a longer time when filling the MOT. A 10 s pulse at 8.5 A for 10 s is sufficient to fill the MOT.

Figure 5.1 shows the MOT fill and decay curve for a dispenser pulse length of 10 s. This measurement was made by imaging the MOT fluorescence at regular intervals during and after the dispenser pulse. It shows the fill rate increasing rapidly during the 10 s dispenser pulse as the temperature of the dispenser increases. The MOT

continues to fill for a second immediately after the dispenser is switched off. The maximum atom number is 7.6×10^7. Once the dispenser is switched off, $\Phi = 0$ and the MOT atom number decays with a loss rate dependent on the background gas pressure: $\mathrm{d}N/\mathrm{d}t = -\gamma N$. Hence, the atom number decays exponentially as $e^{-\gamma t}$. The decay curve is fitted by an exponential, from which a lifetime of 23.4 s is deduced. This is typical for this experiment, although the lifetime depends also on the quality of the MOT beam alignment and can vary by up to ± 5 s.

In practice, the rubidium flux in the chamber does not switch off immediately with the dispenser current. It takes several seconds for the dispenser to cool to below threshold and for the rubidium vapour pressure in the chamber to be reduced by pumping. The time taken for the rubidium pressure to return to its background level can be measured by monitoring the fluorescence of the rubidium vapour in the laser beams. The quadrupole field is switched off so that atoms are no longer collected in the MOT and the trapping beams are tuned to resonance to maximize the fluorescence signal. The dispenser is then pulsed and the fluorescence due to rubidium vapour in the MOT beams is measured by imaging at regular intervals. This is shown in Figure 5.2: it takes approximately 7 s for the vapour pressure to return to its original level after a 10 s dispenser pulse. This is an important consideration for the magnetic trapping stage of the experiment, since the magnetic trap lifetime is very sensitive to background pressure variations. In an experimental cycle, the MOT is therefore operated for a further 12 s after the dispenser pulse

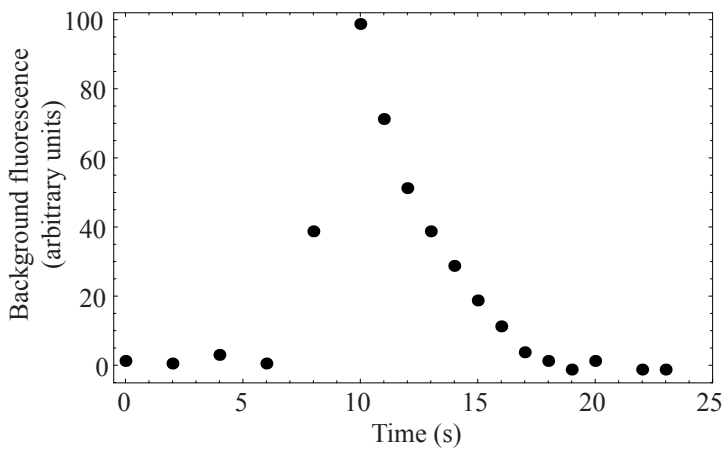

Figure 5.2 *Rise and decay of rubidium partial pressure during dispenser pulse. With the quadrupole field switched off, the fluorescence due to rubidium vapour in the trapping beams is imaged, to give an indication of the relative rubidium flux in the trapping region. The rubidium dispenser is pulsed at 8 A from 0 to 10 s.*

before transferring the atoms to the magnetic trap. In this time, the MOT atom number decays to 5×10^7.

The laser detuning was optimized experimentally: the peak atom number was obtained at -15 MHz. For a fixed total beam power, the MOT atom number scales approximately linearly with beam diameter [58]. In this experiment, the MOT beams are expanded to 15 mm before entering the chamber. There is no gain in increasing the diameter beyond this value as the 45° beams already fill the reflective area (a square of side 22 mm) of the atom chip.

In an earlier mirror-MOT set-up[1], the mirror-MOT exhibited a strong dependence on height above the atom chip surface. A shift in position from 2 mm to 5.5 mm above the surface resulted in a lifetime increase from 10 s to 100 s. At the same time, the MOT atom number showed a factor of 2 variation, peaking at 8×10^6 at a height of 3.5 mm. This variation was not consistent with any feasible model: the cloud had a FWHM of 0.6 mm and was sufficiently far from the mirror that losses to the surface or from reflected fluorescence would be negligible compared to the observed variations. The present experimental set-up shows a much less dramatic variation of lifetime and atom number with height. It could be that the height dependence observed in the smaller mirror-MOT was due to spatial fluctuations in the relative beam intensities or to a simple mismatch in position between the quadrupole field centre and the midpoint of the MOT beam intersection. Now, with a higher MOT beam intensity and a larger beam diameter, the MOT lifetime would be less sensitive to small fluctuations. A bias field of 0.7 G is applied along the x direction to raise the mirror-MOT from 2 mm to 3 mm above the surface during loading — this improves the MOT lifetime by up to a factor of two.

5.1.2 MOT temperature measurement

The temperature of the cloud at the end of the MOT cycle is measured by ballistic expansion. The magnetic quadrupole field and laser beams of the MOT are switched off and the cloud falls freely under gravity. An absorption image of the cloud is taken after a preset time delay, from which a profile of the cloud can be obtained. This is repeated a number of times for different time delays. A simple model is used to extract the temperature from the variation of the width of the cloud with time as it falls freely.

We assume a Maxwell-Boltzmann distribution of velocities within the atom

[1] A different laser system was used, giving MOT beams with 6 mm FWHM and total peak intensity $12\,\mathrm{mW\,cm^{-2}}$ at their intersection.

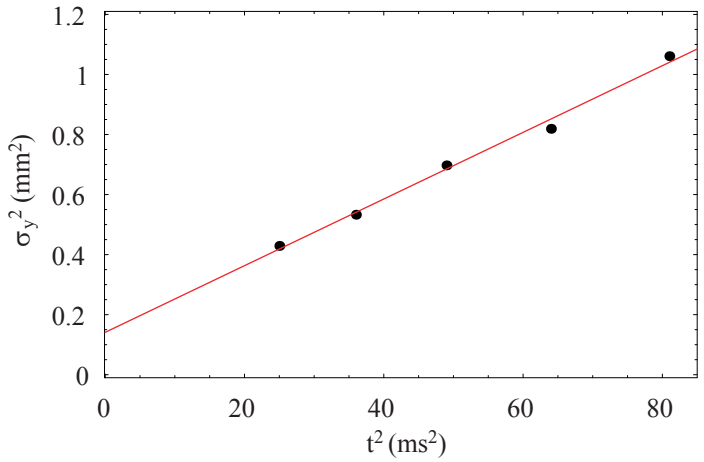

Figure 5.3 *Temperature measurement of the mirror-MOT. The linear fit of σ_y^2 to t^2 gives the temperature ($113 \pm 5\,\mu K$) and initial width (0.38 mm) of the cloud, from Equation 5.7.*

cloud. In one dimension, this is described by:

$$P(v_x) \propto \exp\left(\frac{-mv_x^2}{2k_BT}\right), \tag{5.4}$$

where m is the atomic mass and v_x is the velocity component in the x direction. Using the substitution $x = v_x t$, the probability of an atom which starts at $x = 0$ at $t = 0$ being at a position x, at a later time t, is given by:

$$P(x,t) \propto \exp\left(-\frac{mx^2}{2k_BTt^2}\right). \tag{5.5}$$

A point source of atoms would therefore expand under free-fall, to a Gaussian cloud with a variance of:

$$\sigma_x(t)^2 = \frac{k_BTt^2}{m}. \tag{5.6}$$

However, the atom clouds released from the MOT cannot be approximated as a point source. The initial distribution of the atoms in the MOT is approximately Gaussian, with standard deviation σ_{x0}. The spatial distribution of atoms after t seconds of expansion is therefore a convolution of two Gaussians. This convolution produces a third Gaussian, the width of which is obtained by summing the initial two widths in quadrature [109]. Hence the variation of the cloud width with time is given by:

$$\sigma_x^2(t) = \sigma_{x0}^2 + \frac{k_BTt^2}{m} \tag{5.7}$$

A plot of σ_y^2 against t^2 is shown in Figure 5.3 for the mirror-MOT. From this, a temperature of 113±5 μK is obtained, with an initial width $\sigma_{y0} = 0.38$ mm. This is in good agreement with the measured standard deviation of the MOT of 0.4 mm. Note that the corresponding full-width at half-maximum (FWHM) is 0.95 mm. Along the z-axis, the MOT is much broader, with $\sigma_{z0} = 0.95$ mm (FWHM=2.2 mm). This is due to the fact that the horizontal MOT beams are considerably weaker than the 45° beams and also that the magnetic field gradient is not isotropic. The peak density of the MOT (from Equation 4.13) is 8.6×10^9 atoms cm^{-3}. This implies a phase-space density of 4.7×10^{-8}.

5.2 Compressed MOT

The compressed MOT (CMOT) is a long thin MOT with roughly the same shape as the magnetic traps of the atom chip. This minimizes loss of phase-space density when the atom cloud is transferred to the magnetic trap, which will eventually allow efficient evaporative cooling of the trapped cloud (see Section 6.10).

It was shown in Section 2.3.2 that combination of bias field, B_{bias}, and centre wire current, I_{centre}, produce a long, thin 2D magnetic guide (parallel to the z-axis), around which the magnetic field has a quadrupolar cross-section. If the correct direction of bias field is chosen, the orientation of this 2D quadrupole field matches that of the external, 3D quadrupole field of the mirror-MOT in the $x - -y$ plane. If the 2D quadrupole is superimposed on the 3D quadrupole field of the mirror-MOT, the result is to increase the field gradient in the radial direction, leaving the axial field gradient unchanged.

The compressed MOT increases the density of the atom cloud and distorts the shape of the cloud, making it cigar-shaped. It also shifts the cloud closer to the surface, where the fields due to the wires are strong enough to confine it magnetically when the light is switched off.

5.2.1 Regimes of compressed MOTs

The behaviour of the CMOT is considerably different from that of the mirror-MOT. Several groups have previously studied spherical MOTs at high field gradient and high density [105, 110, 111, 112]. The properties of our CMOT follow similar trends, and are discussed in the thesis of Wenzel Salzmann [113], in which simple models for the spherical MOT are adapted and compared with experimental results obtained in this research group. The important considerations for this experiment are outlined here.

In a low-density MOT such as the mirror-MOT, the size of the trapped cloud is determined by the thermal motion of the atoms. The root mean square radius is given by the equipartition theorem: $r_{rms} = \sqrt{k_B T/\kappa}$, where κ is the spring constant of the trap. As more atoms are loaded into the trap at a given temperature, the size of the cloud stays approximately constant while the density increases [105].

When a MOT is compressed to high density, the collective behaviour of the trapped atoms becomes important. In particular, due to the increase in optical density, forces due attenuation of the laser beams and radiation trapping become significant. The first of these is due to the attenuation of the MOT laser beams as they pass through the trapped cloud. For an atom positioned at the edge of the cloud, a laser beam directed towards the centre of the trap has a higher intensity than the counterpropagating beam which has passed through the atom cloud. This intensity imbalance gives rise to a compressing force [114]. The second force is due to the reabsorption of scattered photons within the trapped cloud (radiation trapping) [115, 116, 105]. This creates an effective repulsive force between the trapped atoms, which grows rapidly with atom density once the cloud is optically thick. The size of the MOT in this regime is governed by the balance between these two forces and the trapping force. Experimentally, it is found that the radiation trapping force limits the density which can be attained in a MOT. In this regime, the radius of the cloud is expected to increase smoothly with atom number [110]. The geometry of our CMOT allows a higher atomic density to be reached than in a spherical compressed MOT, by reducing the number of times a photon must scatter before it can escape from the cloud. The radiation trapping force is also greatly reduced by detuning the light to reduce the scattering rate.

If a MOT is compressed enough, it can exhibit a two-component distribution. Close to the centre of the MOT, the force gradient is high due to the influence of polarization gradient cooling (Section 2.1.4). Further from the centre, the confinement is weaker as the magnetic field Zeeman shifts the trapping transition further out of resonance. As more atoms are added to a MOT, the cloud radius increases until the central, strongly confining region is full. Further atoms then spill out into the weakly confining volume and spread out to a much larger radius [105]. It is not useful to compress the CMOT to this point since atoms in the outer region will not be transferred efficiently to the magnetic trap.

5.2.2 Compressing the mirror-MOT

After filling the mirror-MOT, the centre wire current and the bias field are ramped linearly from zero to their final values, typically $I_{centre} = 15\,\mathrm{A}$ and $B_{bias} = 22\,\mathrm{G}$,

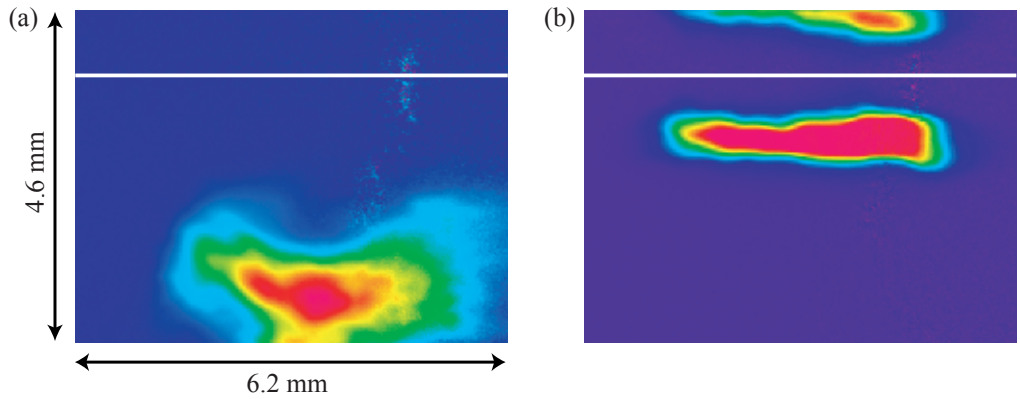

Figure 5.4 *Images of the fluorescence of the mirror-MOT (a) and CMOT (b). The distances of the atom cloud centres from the atom chip surface (indicated as white line) are 3 mm and 0.8 mm respectively. A partial reflection of the CMOT can be seen due to the reflective gold surface.*

in 20 ms. This compresses the MOT radially and shifts its position towards the atom chip surface in a continuous manner. The radial field gradient is increased to 160 G cm^{-1} and the height of the trap shifted to 0.77 mm above the surface. Fluorescence images of the mirror-MOT and CMOT are shown in Figure 5.4. Axial (z) and radial (y) profiles of the CMOT are shown in Figure 5.5. The profiles can be fitted fairly well by Gaussians, as shown. Deviations from a Gaussian distribution occur due to spatial variations in the light field. This is particularly noticeable in the axial profile, which exhibits several peaks. The standard deviations of the CMOT cloud are 0.128 mm radially and 1.16 mm axially. This ratio, 1:10, approximately follows the field gradient ratio, 1:15. This anisotropic MOT shape is clearly more appropriate for matching into a long, thin magnetic trap. Using Equation 4.13, we obtain a peak density of this CMOT of 1.4×10^{11} cm^{-3}, which is a factor of 16 higher than that of the mirror-MOT.

CMOT Lifetime

When a MOT reaches sufficiently high density, two-body collisions in the presence of light can lead to significant loss [53]. This loss mechanism is observed in our CMOT as a deviation from exponential of the decay curve, as shown in Figure 5.6 at short times. The colliding ground state atoms can absorb a photon and go to an excited diatomic molecular state. The subsequently emitted photon can be strongly red-shifted, with the excess energy being given to the two atoms which then escape.

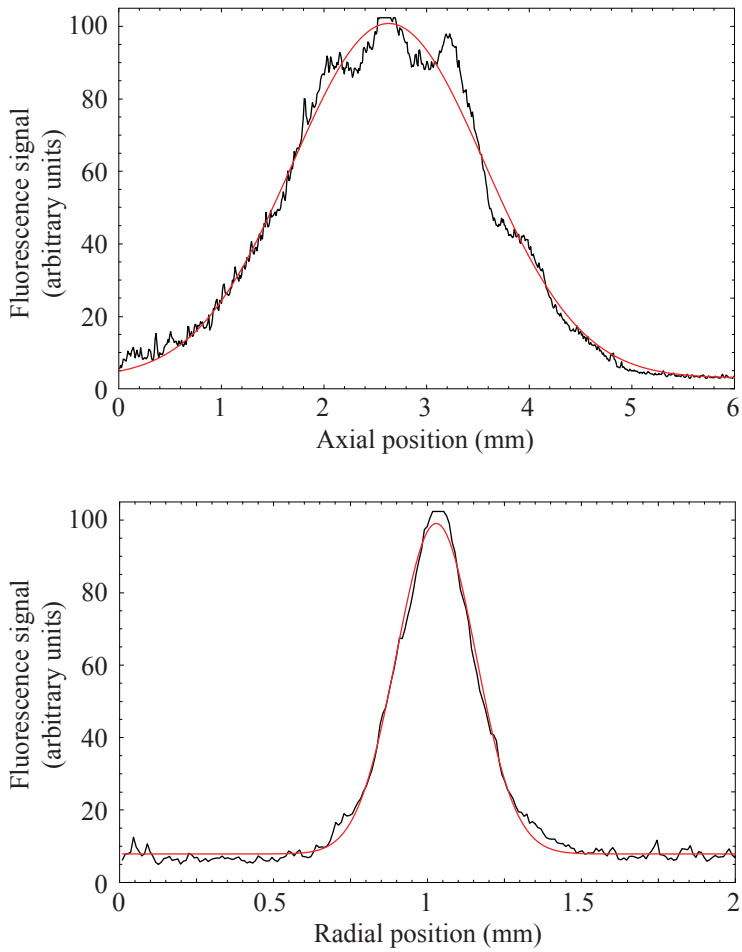

Figure 5.5 *Axial (left) and radial (right) profiles of the compressed MOT. The radial field gradient is 160 G cm^{-1} and the laser beam detuning is −15 MHz. Gaussian fits to the profiles give standard deviations of the cloud of 1.16 mm axially and 0.128 mm radially.*

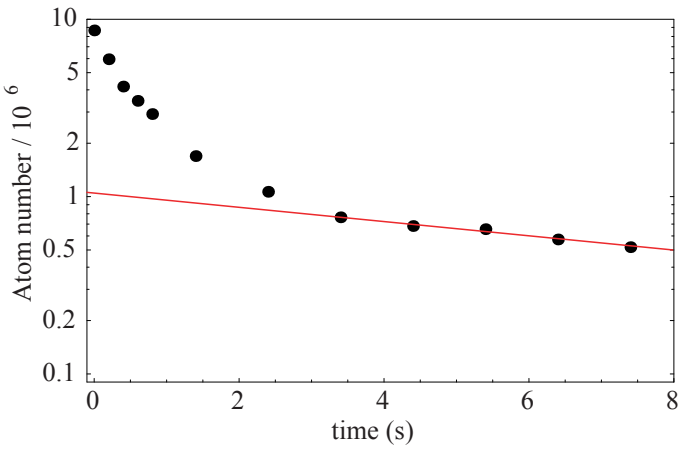

Figure 5.6 *CMOT decay curve, for a radial field gradient of 60 G cm^{-1}. The initial density is 1×10^{11} cm^{-3}. An exponential curve is fitted to the last five points, giving a lifetime of 10.5 s.*

The loss rate is described by:

$$\frac{\mathrm{d}n}{\mathrm{d}t} = -\gamma n - \beta n^2, \tag{5.8}$$

where n is the atom number density.

Wallace *et al* [117] give values of β versus laser intensity which indicate $\beta \sim 3 \times 10^{-12}\,\mathrm{cm}^3\,\mathrm{s}^{-1}$ for our CMOT. At our initial density, the decay rate is expected to be of order $1\,\mathrm{s}^{-1}$. In fact, we measure roughly three times that during the first 500 ms after compressing the MOT. It is possible that our initial decay rate is higher because of intensity imbalances and spatial variations in the trapping beams. Both [117] and [118] observe this strong dependence of loss rate on alignment.

The lifetime and position of the CMOT are particularly sensitive to the alignment of the horizontal laser beams. This is because the CMOT is cylindrical, with its long axis parallel to the horizontal beams. The horizontal beams are therefore attenuated along the length of the CMOT. For this reason it is important that the horizontal beams are not implemented by a single, retro-reflected beam, but by two separate beams.

Detuning the CMOT

In optimizing the parameters of the CMOT, the main goal is to create an atom cloud which is as dense and as cold as possible. This maximizes the number of atoms which can be transferred to the magnetic trap. Both density and temperature are optimized by detuning the trapping beams further from resonance.

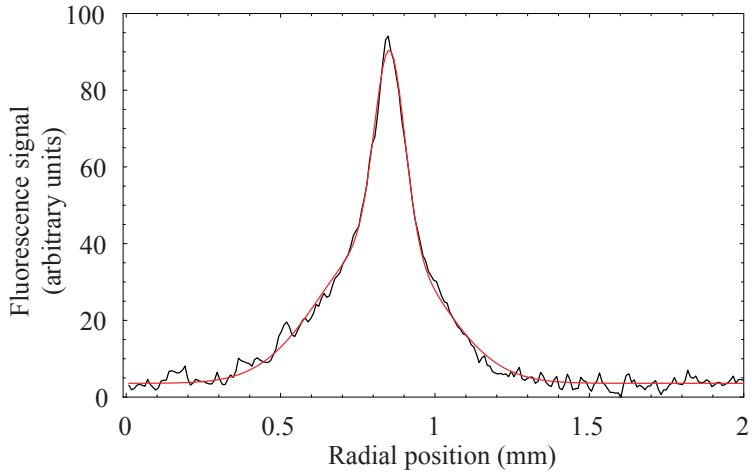

Figure 5.7 *Radial profile of the CMOT after detuning to −54 MHz. The fit is the sum of two Gaussians.*

Immediately after ramping up the centre wire current and bias field, the trapping beams are detuned to −32 MHz for 4 ms and then to −54 MHz for 1 ms. This reduces the rescattering force, allowing the atom cloud to collapse in on itself to a higher density. Figure 5.7 shows the new radial profile after detuning (c.f. Figure 5.5). The total atom number is unchanged, but the shape of the profile is no longer Gaussian — detuning the lasers has brought the CMOT into the two-component regime. The fit to the profile is the sum of two Gaussian distributions: a narrow Gaussian with FWHM 0.12 mm and a broader Gaussian with FWHM 0.47 mm. Approximately half the atoms are contained in the central region, with a total peak density of $1.7 \times 10^{11}\,\mathrm{cm}^{-3}$. Further compression does not increase the peak density, but reduces the number of atoms in the central feature. (Petrich *et al* [111] report a maximum density for ^{85}Rb of $2 \times 10^{11}\,\mathrm{cm}^{-3}$ at a detuning of −32 MHz for a total atom number similar to our MOT.) This technique can only produce transient increases in density, as the rate of arrival of atoms at the centre during detuning is soon outweighed by increase in density-dependent losses. For this reason, the detuning time is kept to a minimum.

Temperature of the CMOT

Increasing the trapping beam detuning cools the cloud, since $T \propto I/\Delta$. Temperature measurements for the CMOT are shown in Figure 5.8 for two different detunings. At −40 MHz ($-6.6\,\Gamma$) the radial temperature is $82\,\mu$K; at −54 MHz ($-9\,\Gamma$), the temperature is only $47\,\mu$K.

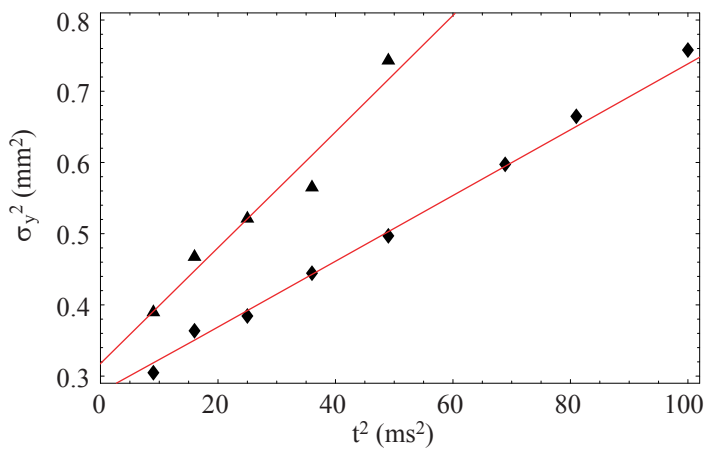

Figure 5.8 *Temperature measurement of CMOT by ballistic expansion after detuning to −40 MHz (triangles) and −54 MHz (diamonds) for 1 ms. The fitted temperatures are 82 μK and 47 μK respectively.*

	Mirror-MOT	CMOT
Detuning, Γ	-15 MHz	-54 MHz
Atom Number, N	5×10^7	5×10^7
Temperature, T_{radial}	113 μK	47 μK
Radial $1/\sqrt{e}$ width, σ_r	380 μm	51 μm (central region)
		200 μm (outer region)
Axial $1/\sqrt{e}$ width, σ_z	1.16 mm	1.02 mm
Peak density, n_0	8.6×10^9 cm^{-3}	1.7×10^{11} cm^{-3}
Phase-space density	4.7×10^{-8}	3.4×10^{-6}

Table 5.1 *Parameters of the mirror-MOT and CMOT.*

The CMOT parameters were optimized largely by trial and error, to maximize the number of atoms transferred to the magnetic trap. The length of time for which the lasers are detuned is set at 1 ms. There is a trade-off between sufficient cooling and density enhancement, against atom loss due to density-dependent effects. The maximum efficiency we have achieved for transfer of atoms to the magnetic trap is 40%. This process will be described in the next chapter. Table 5.1 summarizes the parameters for the optimized conditions of the mirror-MOT and CMOT. The phase-space density is defined as PSD $= n_0 \lambda_{deB}^3$, where the atomic de Broglie wavelength at temperature T is $\lambda_{deB} = h/\sqrt{2\pi m k_B T}$.

5.3 Microscopic surface MOTs

One of the initial experiments using the gold-coated magnetized videotape of this thesis was to load atoms into the microtraps using magneto-optical forces. It was shown in Figure 2.8, Section 2.3.1 that if a bias field, B_{bias} is applied to the field of the magnetic mirror in the correct direction, the quadrupole magnetic field lines of the tubes match those of the external quadrupole field. The field lines are then correlated with the circular polarizations of the reflected MOT beams so as to make each tube work as a cylindrical 2D MOT. Axially, the tubes provide no confinement, although the horizontal MOT beams still give rise to optical molasses cooling.

It was found that the loading efficiency into the tubes and the lifetime were both too low for this to be a feasible loading scheme. However, this was the first observation of 2D MOTs on this scale and a summary of our observations is presented here. These experiments were carried out prior to improvements to the laser system and vacuum, so the initial atom numbers collected in the mirror-MOT are significantly lower than those described in the rest of this thesis.

The optimum loading method was as follows: first, atoms were collected in the mirror-MOT (typically 2×10^7); the external quadrupole field was then switched off and the MOT beams detuned to $-30\,\mathrm{MHz}$, allowing the atoms to fall towards the surface; a bias field of $0.7\,\mathrm{G}$ was switched on $5\,\mathrm{ms}$ later to create the tube MOTs. Since the atoms were cooled and slowed in optical molasses as they fell from the mirror-MOT, the tube MOTs filled continuously from the atoms cloud over about $100\,\mathrm{ms}$. A weak quadrupole field, $10\,\mathrm{G\,cm^{-1}}$ oriented along the axis of the tubes, was then switched on to provide a stronger MOT force along the tube axes.

Figure 5.9 shows an image of the fluorescence of the tubes viewed at grazing incidence to the mirror, at an angle of $54°$ to the axis of the tubes. The upper line is the array of tubes, one behind the other; the lower line is a reflection of the fluorescence in the gold surface. The stripes above the trapped atoms are due to interference between the MOT laser beams, which can be seen as fluorescence from the tenuous cloud of cold atoms above the mirror. The separation of the atoms and their reflection is $194\,\mu\mathrm{m}$, implying that the surface MOTs are formed $97\,\mu\mathrm{m}$ above the videotape surface. For a bias field of $0.7\,\mathrm{G}$, the calculated height of the tubes above the mirror is $\ln(B_1/B_0)/k = 97.4\mu\mathrm{m}$, which is completely consistent with the measurement.

Figure 5.10(a) shows the same array viewed from above. Here the tubes are partially obscured by the haze due to the atom cloud above the mirror. Integrating the image in the z direction yields a smooth, broad profile due to the cloud, modulated by the surface MOT intensity distribution. A smooth curve is fitted to the cloud

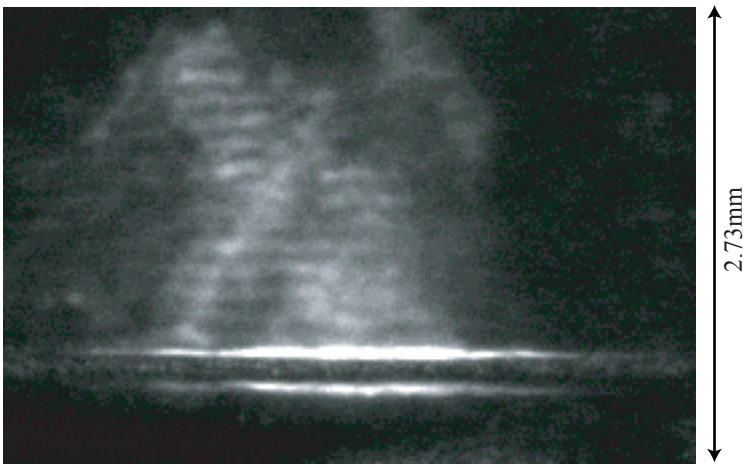

Figure 5.9 *Image of the fluorescence from an array of surface MOTs from the side. The upper line is the array; the lower line is its reflection in the gold surface (see text).*

and then subtracted. The residuals, due to the surface MOTs, are shown in Figure 5.10(b). Figure 5.10(c) shows the positions of the microscopic MOTs. From the slope of this plot, the mean separation of the tubes is calculated to be $110 \pm 5\mu$m. The uncertainty here is due to the camera calibration.

From these images, we estimate that the radius of the surface MOT tubes is only $10\,\mu$m, placing these among the smallest MOTs to date (see also [119]). The field gradient of these surface MOTs is $411\,\mathrm{G\,cm^{-1}}$, which is a factor of 40 larger than the field gradient of the mirror-MOT, while the size is approximately 50 times less. This suggests that the temperature of the microscopic MOTs is not significantly higher than that of the mirror-MOT.

The rate at which these surface MOTs decay depends on the detuning of the laser beams. At $-10\,$MHz detuning (the usual mirror-MOT detuning for the laser intensity of this set-up), a lifetime of $\sim 30\,$ms is observed. At $-30\,$MHz detuning, this lifetime increased to $\sim 150\,$ms. The maximum number of atoms loaded into the microtraps was 1×10^6: a loading efficiency of 5%.

The array of microMOTs described in this section is not used for the work contained in the rest of this thesis. However, it remains an interesting possibility to load an array of magnetic microtraps by capturing atoms in this way into an array of microMOTs

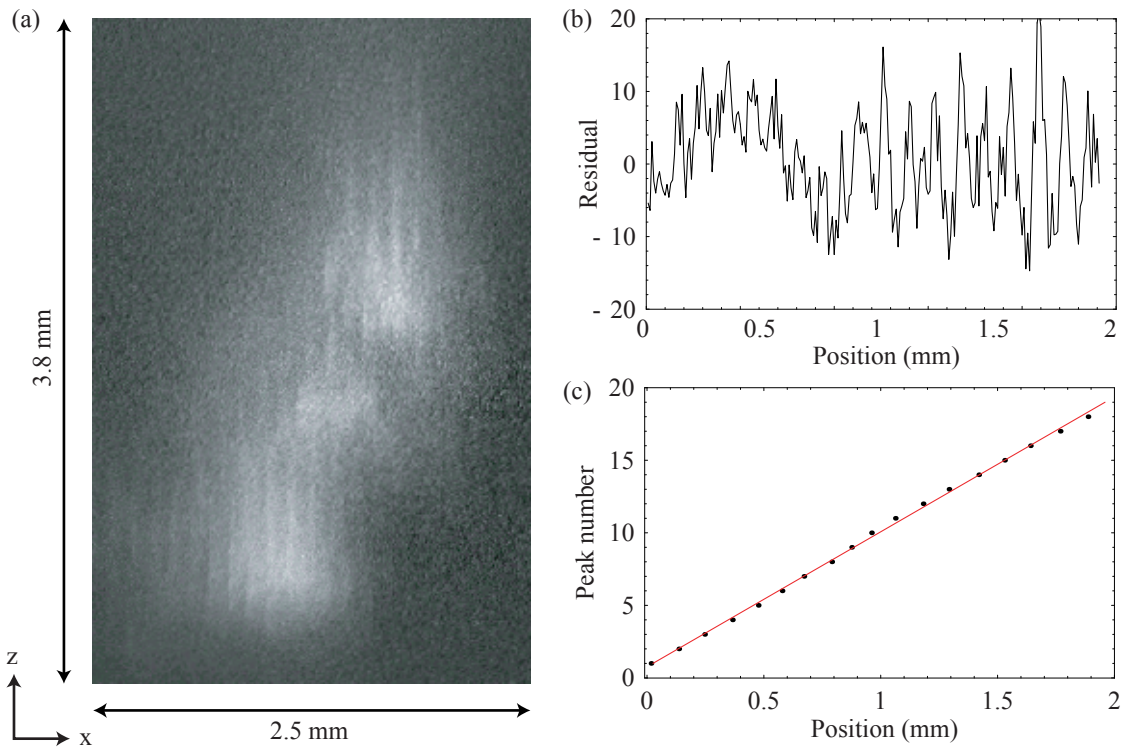

Figure 5.10 *(a) Image of the fluorescence from an array of surface MOTs from above. The stripes are partially obscured by a cloud of atoms above the surface. (b) Profile of the microMOT array, integrated along z, after the broad cloud has been subtracted. (c) shows a fit of peak position to number, from which the wavelength of the videotape is deduced.*

Chapter 6

Magnetic Trapping

The first part of this chapter describes the sequence of events by which a cloud of atoms is transferred from the CMOT to the wire trap and hence to the microtraps formed above the videotape. Later, we present lifetimes of the trapped atoms cloud at different distances to the surface and at different trap frequencies.

6.1 Optical pumping

In Section 2.2.2 it was shown that only atoms in substates $|F, m_F\rangle = |2, 2\rangle$, $|2, 1\rangle$, $|2, 0\rangle$, $|1, -1\rangle$ of the rubidium groundstate can be trapped in a magnetic field minimum and, of these, the trapping force (proportional to m_F) is strongest for the $|F, m_F\rangle = |2, 2\rangle$ state. However, after the atom cloud has been prepared and cooled in the mirror-MOT, the atomic population is distributed over all the magnetic substates of the $5\mathrm{P}_{3/2}$ $F = 2$ hyperfine level. In particular, the MOT leaves atoms mainly in the $m_F \leq 0$ states. In order to trap the maximum possible number of atoms, the atoms are optically pumped into the $|F, m_F\rangle = |2, 2\rangle$ state.

Optical pumping is carried out by driving a transition between states F and F' with light which is σ^+ polarized with respect to the quantization axis — in this case, the quantization axis is defined by an applied magnetic field. We use the $5\mathrm{S}_{1/2}$ $F = 2 \rightarrow 5\mathrm{P}_{3/2}$ $F' = 2$ transition (see Figure 2.3), for which the relevant magnetic sublevels are shown in Figure 6.1. Since σ^+ light is used, only $\Delta m_F = +1$ transitions are allowed. Hence an atom in the state $|F = 2, m_F\rangle$ will be pumped into the level $|F' = 2, m_F + 1\rangle$ when it absorbs a photon. It can then decay by spontaneous emission via any transition which satisfies the selection rules: $\Delta F = 0, \pm 1$ and $\Delta m_F = 0, \pm 1$. From the level $|F' = 2, m_F + 1\rangle$, an atom can decay to the states $|(F = 1, 2), m_F\rangle, |(F = 1, 2), m_F + 1\rangle, |(F = 1, 2), m_F + 2\rangle$. Thus after

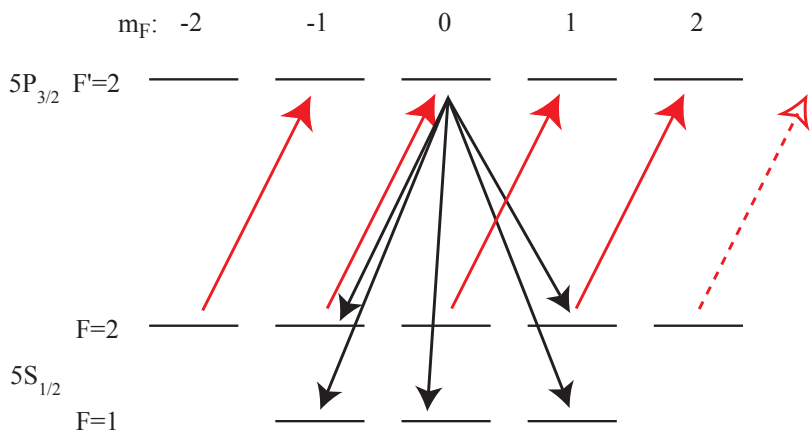

Figure 6.1 *Optical pumping transition. The solid red arrows indicate σ^+ transitions driven by the optical pumping beam. Spontaneous decay can occur to levels linked by $\Delta F = 0, \pm 1$ and $\Delta m_F = 0, \pm 1$, as shown for the $m'_F = 0$ state. 50% of atoms excited to $F' = 2$ decay to the $F = 1$ level and are recycled by repump laser light. Atoms which are optically pumped into the $F = 2, m_F = +2$ dark state no longer interact with the optical pumping light.*

each absorption and emission cycle, the atomic population will be distributed over states with a higher average m_F. The fraction (50%) which decay to the $F = 1$ state no longer interact with the optical pumping light and so repump laser light is overlapped with the optical pumping beam to drive the transition back to $F' = 2$.

Once an atom is pumped into the $|F, m_F\rangle = |2, 2\rangle$ state it is in a *dark state* and no longer interacts with the optical pumping light. In this way it possible to optically pump even clouds which are initially optically dense. More importantly, this prevents unnecessary heating of the atom cloud, since each photon scattered imparts a recoil momentum, $\hbar\mathbf{k}$: this is the real advantage of using the $F = 2 \rightarrow F' = 2$ transition, rather than the experimentally more amenable $F = 2 \rightarrow F' = 3$. The degree of polarization that can be achieved is limited by the purity of the polarization of the light relative to the magnetic field axis, since the wrong polarization pumps atoms out of the dark state. In that limit, the optical pumping efficiency cannot be increased by lengthening the optical pumping pulse: this only contributes to heating the cloud. The experimental set-up for optical pumping is shown in Figure 6.2. The optical pumping transition frequency is 267 MHz red-detuned of the trapping transition and is accessed by frequency shifting light from the reference laser, using a double-pass AOM operating at -133.5 MHz. This beam is combined with repump laser light at a 50/50 beam cube. After spatial filtering, the beam is expanded to 1 cm diameter. The beam undergoes several reflections

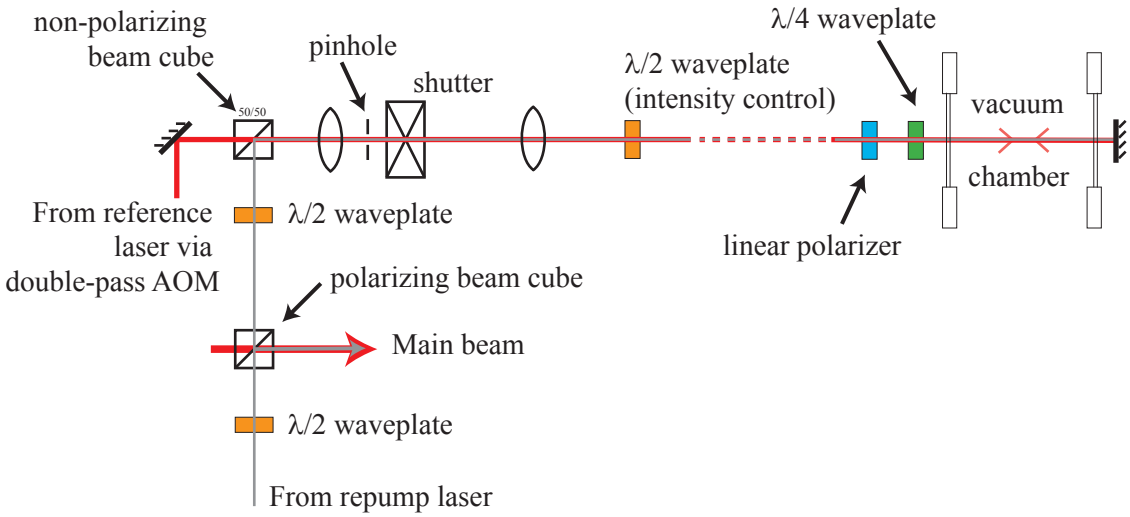

Figure 6.2 *Optical pumping beam optics. The relative intensity of repump light in the optical pumping arm is selected by the $\lambda/2$ waveplate near the bottom of the figure. A second $\lambda/2$ waveplate ensures that the beams have the same linear polarization when combined. The dashed line represents the beam path, via several mirrors, to the vacuum chamber.*

at skew angles before reaching the vacuum chamber, which do not preserve the polarization of the beam. The circularly polarizing optics (linear polarizer followed by $\lambda/4$ waveplate) are therefore mounted on the chamber. A $\lambda/2$ waveplate is located before these optics to adjust the intensity of the light in the final beam which enters the chamber. The optical pumping beam is retro-reflected to minimize the radiation pressure force on the atom cloud.

The pulse length required for optical pumping can be estimated by considering that, for a population of atoms in the state $|F, m_F\rangle = |2, -2\rangle$, virtually all the atoms will be optically pumped to the $|F, m_F\rangle = |2, 2\rangle$ state after scattering 20 photons. At saturation the scattering rate is $\Gamma/4 = 1.5 \times 10^6\,\mathrm{s}^{-1}$. Therefore, a suitable optical pumping time for a single atom is $1\,\mu$s. We must however consider the thickness of the cloud through which the optical pumping beam passes: a typical cloud prepared in a CMOT is a cylinder of length 2.5 mm and diameter 0.3 mm, with density $n_0 = 1.7 \times 10^{11}\,\mathrm{cm}^{-3}$. Due to the geometry of the chamber, the optical pumping beam crosses the atom cloud at approximately 67° to the long axis of the cloud. It therefore traverses $\sim$ 0.33 mm thickness of cloud. The absorption cross-section for rubidium (Equation 4.9), averaged over the optical pumping and repumping transitions is $\sigma_L \sim 7 \times 10^{-10}\,\mathrm{cm}^2$, yielding a penetration depth of the

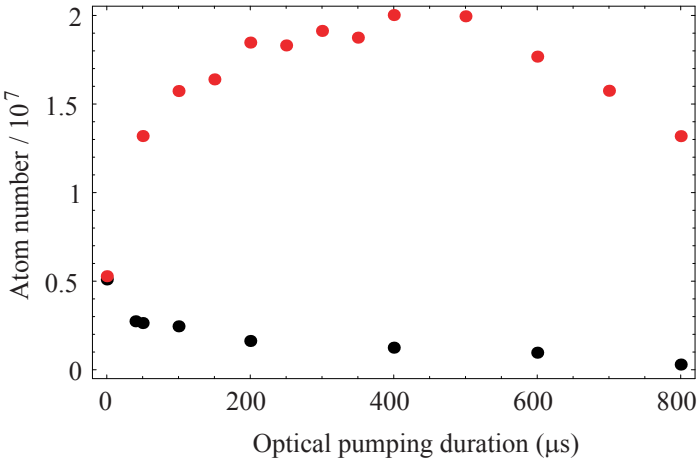

Figure 6.3 *Number of atoms transferred to the magnetic trap as a function of optical pumping duration. The red dots indicate optical pumping with σ^+ light; the black dots with σ^- light. The latter pumps the atom cloud into untrapped states. The atom number was determined by absorption imaging, 1 s after switching the magnetic trap on.*

order of $(n\sigma_L)^{-1} = 1\,\mu$m. The time needed to optically pump the entire cloud is therefore about 300 times that for a single atom, or $\sim 300\,\mu$s.

Figure 6.3 shows the number of atoms transferred to the magnetic trap as a function of optical pumping pulse length. This shows that the number of magnetically trapped atoms is increased by a factor of four by applying a 0.4 ms optical pumping pulse. For longer pulse lengths, the number of trapped atoms decreases due to heating the cloud, or possibly due to a decrease in matching efficiency, due to expansion of the cloud. The intensities of both the repump and $F = 2 \rightarrow F' = 2$ light in the optical pumping beam was $200\,\mu\text{Wcm}^{-2}$. The $F = 2 \rightarrow F' = 2$ pulse is controlled by the AOM. The repump light is controlled only by the shutter, which has a minimum open time of 5 ms. If the circular polarization of the optical pumping beam is reversed, atoms are pumped into the untrapped $|F, m_F\rangle = |2, -2\rangle$ state. The number of atoms transferred to the magnetic trap then decreases with the optical pumping pulse length. This effect is also shown in Figure 6.3.

Ideally, optical pumping would use the axial field (generated by the end wires) as the quantization axis. This would minimize the subsequent rotation of the local magnetic field as the magnetic trap was switched back on. In order to apply an optical pumping field along this direction of the pumping beam, it would be necessary to switch off the laser beams, centre wire current and bias field used to generated the CMOT, then to switch on the quantization field and apply the optical pumping pulse, before switching the magnetic trapping fields back on. The problem

associated with this is that the bias field cannot be switched on instantaneously — it has a rise time of 2.5 ms. The minimum time for this process would be ~ 3 ms, during which time the cloud would expand (to $\sim 200\,\mu$m), and fall under gravity ($\sim 50\,\mu$m).

Instead, we leave the bias field on at, $B_{bias} = 23$ G, during the optical pumping process. We also switch on a 20 A current in the end wires to give an axial field B_z of about 7 G at the centre of the cloud. This rotates the total field by 18°. The optical pumping beam is aligned at 23° to the x-axis (due to limited optical access), which brings it within 5° of the quantization field. The optical pumping sequence is summarized by Figure 6.4. The centre wire current, anti-Helmholtz coils and trapping beams are all switched off simultaneously at $t = 0$. The optical pumping pulse and end wire current are switched on at the same instant. At the end of the optical pumping pulse, the centre wire current is switched back on to form the magnetic trap. The anti-Helmholtz coils switch off over 700 μs.

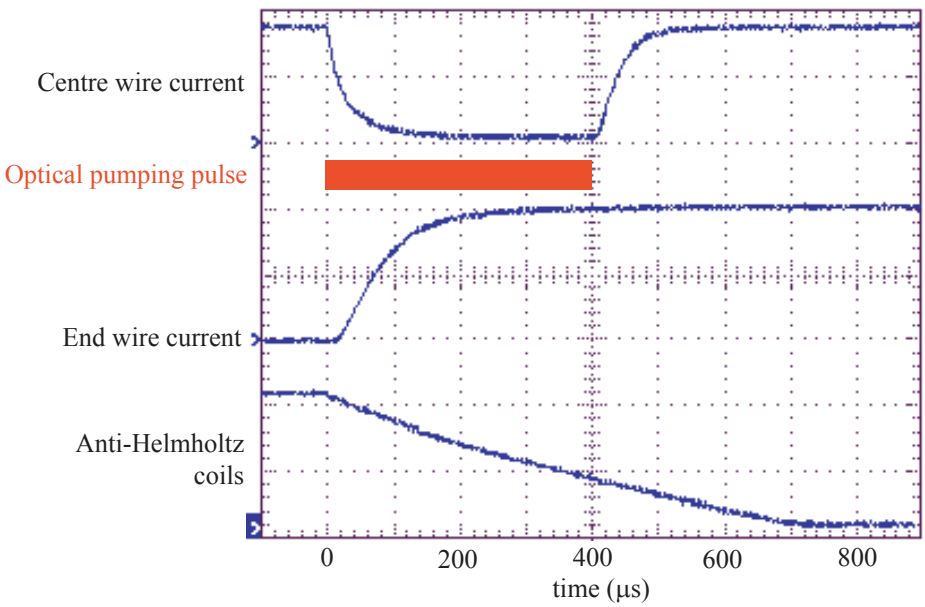

Figure 6.4 *Optical pumping sequence. Switching times of the centre wire currents ($15 \to 0 \to 15$ A), end wire current ($0 \to 20$ A) and quadrupole field ($10 \to 0$ G cm^{-1}) are shown graphically. The duration of the optical pumping pulse is 400 μs and the MOT laser beams are switched off at $t = 0$ (AOM switching time < 5 ms).*

Since we optically pump in a strong magnetic field (23 G), the optical pumping frequency is shifted from resonance. The Zeeman shift of the σ^+ transition frequency

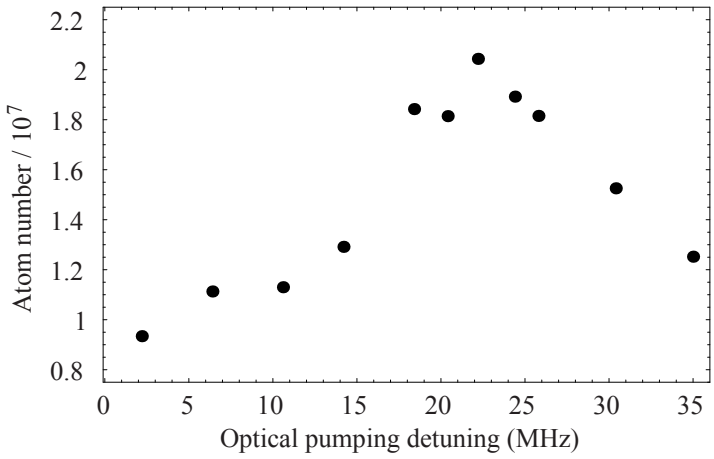

Figure 6.5 *Optimization of optical pumping frequency. The number of atoms stored in the magnetic trap, 1 s after optical pumping is plotted against optical pumping frequency.*

depends on m_F:

$$\begin{aligned}\Delta(g_F m_F \mu_B B/h) &= (g'_F m'_F - g_F m_F)\mu_B B/h \\ &= \left(\frac{2}{3}(m_F+1) - \frac{1}{2}m_F\right)\mu_B B/h \\ &= (\frac{2}{3} + \frac{m_F}{6})\mu_B B/h \end{aligned} \tag{6.1}$$

Thus, for the states $m_F = -2, -1, 0, +1$, the atomic transition frequency is blue-detuned by 10.7, 16.1, 21.5, 26.8 MHz respectively. Figure 6.5 shows the dependence of optical pumping on frequency. We measure an optimum detuning of +19 MHz from the zero field transition frequency.

To summarize, we are able to switch off the trapping potential for the absolute minimum necessary time (the length of the optical pumping pulse) with the disadvantage of optically pumping at a small angle to the quantization axis. In principle, we would expect this to limit the efficiency of optical pumping, since it introduces a ($\sin(5°) = 0.09$) component of π light to the optical pumping beam, so that atoms can be pumped out of the 'dark state'. In practice, we see a four-fold increase in magnetic trap atom number when the atom cloud is optically pumped for 0.4 ms, as shown in Figure 6.3.

6.2 Matching the atom cloud from the CMOT to the magnetic trap

After the atom cloud has been optically pumped into the $|F, m_F\rangle = |2, 2\rangle$ state, the centre wire current is switched back on to form a magnetic trap. It is important for the magnetic trap to be matched to the shape and size of the atom cloud at the end of the optical pumping process. This ensures that the cloud's size is conserved and therefore, that there is no heating during the transfer. The matching condition can be derived by considering the distribution of a cloud of given temperature, T, in a magnetic trap of frequency ω_i. The mean potential energy of an atom, U_i, in the ith dimension, is related to the temperature through $U_i = k_B T/2$. In a harmonic trap, $U_i = \frac{1}{2}\kappa_i \overline{x_i^2} = \frac{1}{2}\kappa_i \sigma_i^2$. Equating the two expressions and substituting $m\omega_i^2$ for κ_i gives:

$$\omega_i = \frac{1}{\sigma_i}\sqrt{\frac{k_B T}{m}}. \tag{6.2}$$

This determines the trap frequency required to match to a cloud of given temperature and width. If this condition is not met, breathing modes of the cloud will be excited after transfer, with a subsequent loss of phase-space density. The σ-widths of the CMOT before optical pumping are 1.02 mm axially and 0.2 mm radially, therefore matching requires respective magnetic trap frequencies of $2\pi \times 10$ Hz and $2\pi \times 53$ Hz.

The simplest way to transfer a cloud of atoms from the CMOT to a magnetic trap is simply to switch off the MOT laser beams, while maintaining the constant values of $B_{bias} = 23$ G and $I_{centre} = 15$ A. This magnetic trap has trap frequencies of $2\pi \times 15$ Hz and $2\pi \times 90$ Hz, the values of which were obtained by the measurements described in the next section. It turns out that these trap frequencies are similar to those required by the matching condition. Varying the bias field or centre wire current during transfer to the magnetic trap (to match the magnetic trap more closely to the CMOT) gave no significant improvement to the atom number or temperature of the cloud after transfer. We therefore continue to use these parameters for the initial magnetic trap into which we load atoms. The depth of this magnetic trap (limited by the axial potential) is 12.5 G, which corresponds to a temperature of 840 μK, or 17 times the measured CMOT temperature.

Accurate measurements of the number of atoms in the magnetic trap are obtained by absorption imaging with the trapping potential switched off and a magnetic field applied along the imaging beam direction (see Section 4.4.3). We find that the number of atoms transferred to the magnetic trap is 2×10^7, or 40% of the CMOT number. This transfer efficiency is typical of this type of experiment: [42] and [35] both report transfers of 40–50% between MOT and magnetic trap, even for total

atom numbers a factor of ten higher and lower respectively

6.3 Slosh-prevention and measurement of trap frequencies

Loading atoms into the magnetic trap off-centre will result in the cloud sloshing back and forth in the trap — this additional kinetic energy will cause heating of the cloud as it rethermalizes. It is therefore important to overlap the magnetic trap centre with the centre of the atom cloud.

The CMOT and the magnetic trap into which it is transferred are generated by the same centre wire current and bias field (15 A, 23 G). The two traps are therefore well overlapped in the x direction, but not perfectly in y or z. The reason for the lack of overlap in the z direction is that the CMOT position along this axis is determined by the external quadrupole field and the alignment of the horizontal laser beams, and is not necessarily at the axial centre of the atom chip. The mismatch in height (y) between the CMOT and the magnetic trap occurs because the CMOT height depends on the overall trapping potential due to the anti-Helmholtz coils and the wire and bias fields. The magnetic trap height depends on the wire and bias fields alone. The CMOT position is therefore shifted slightly away from the atom chip, relative to the magnetic trap position. (The atom chip position is adjusted so that the quadrupole field is well-aligned with the centre wire in the x direction.) Without any correction for these effects, the atom cloud oscillates about the centre of the magnetic trap, as shown in Figures 6.6 and 6.7. These oscillation curves were obtained by imaging the cloud in the magnetic trap at different times after loading and measuring the position of the cloud centre as a function of time. Elastic collisions between trapped atoms redistribute the kinetic energy between the axial and radial degrees of freedom, thus the oscillations are damped as the cloud rethermalizes. Also, when the atom cloud extends out of the harmonic region of the trapping potential, atoms in the wings of the distribution oscillate at a different frequency from those close to the trap centre, and again the oscillation is damped.

6.3.1 Axial trap frequency

The axial oscillations shown in Figure 6.6 can be fitted to a decaying sine wave, $A\sin(\omega_z t + \phi)e^{-t/\tau}$, giving an axial trap frequency of $\omega_z = 2\pi \times (15.35 \pm 0.03)$ Hz. This is in excellent agreement with the calculated axial frequency for the parameters of our atom chip for a magnetic trap at this height (see Section 2.3.4). Since this frequency is reliably established, the axial cloud length is a good way to determine the temperature of cold clouds, as will be discussed in Section 6.10.2. The amplitude

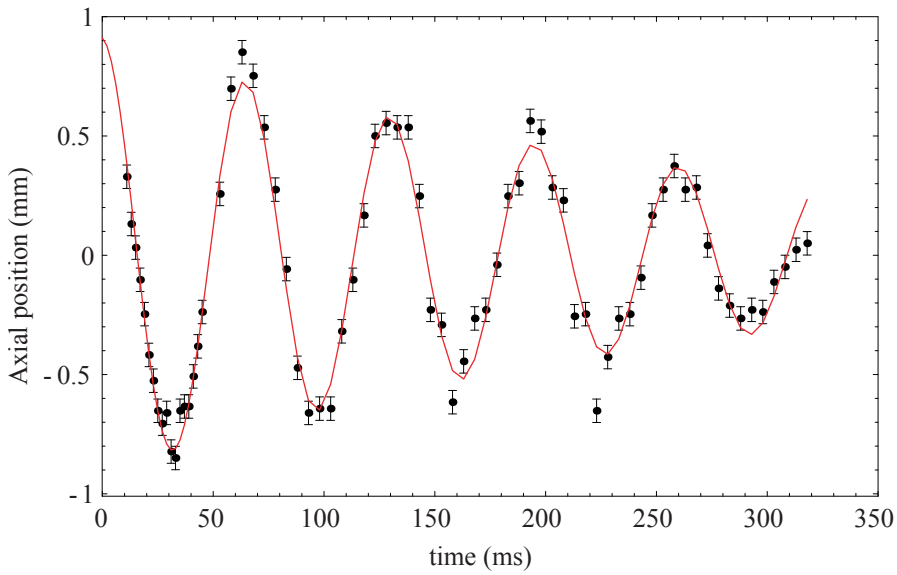

Figure 6.6 *Axial oscillations in the magnetic trap. The magnetic trap is switched on at $t = 0$. The oscillations are fitted by the equation $\Delta z = A\sin(\omega_z t + \phi)e^{-t/\tau}$, giving $\omega_z = 2\pi \times 15.35\,Hz$. The initial amplitude is 0.9 mm and decays with a $1/e$ lifetime $\tau = 0.29\,s$.*

of the axial oscillations in Figure 6.6 is 0.9 mm — small compared with the 2.5 mm FWHM of the cloud. The long decay time (0.29 s) is not surprising, since the trap should be rather harmonic over this central region. Fits to the amplitude measured at 500 ms and 1.4 s show the decay time increasing to ~ 0.5 s, indicating that the oscillations become more harmonic as the amplitude decreases.

The phase of the oscillations indicates that they result from loading the trap off-centre, rather than from imparting a velocity to the cloud during the transfer from the CMOT to the magnetic trap. To minimize axial sloshing, an additional small bias field is applied along the z-axis during the CMOT phase. This controls the axial position of the CMOT so that it can be aligned with the magnetic trap. In this way, the axial oscillation amplitude is reduced to 225 μm.

6.3.2 Radial trap frequency

The radial oscillations (Figure 6.7) decay much faster than the axial oscillations, with a $1/e$ time of 12 ms. This is not surprising because the trapping potential deviates by 10% from being harmonic at a radius of 0.14 mm. The cloud is much broader than this (CMOT FWHM = 0.47 mm) and so the oscillations decay rapidly due to the anharmonicity of the trap. Since fewer oscillations can be observed, the

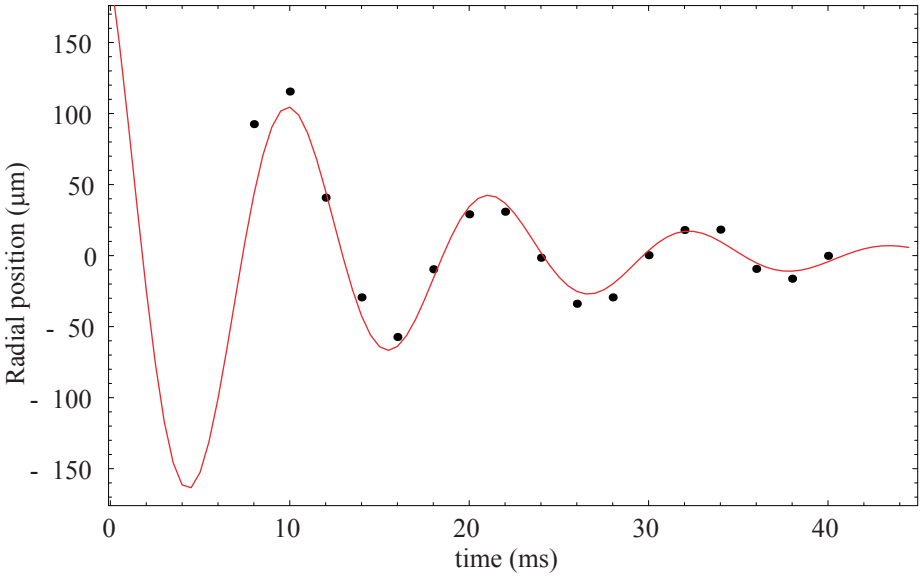

Figure 6.7 *Radial oscillations in the magnetic trap. The magnetic trap is switched on at $t = 0$. The oscillations are fitted by the equation $\Delta y = A\sin(\omega_r t + \phi)e^{-t/\tau}$, giving $\omega_z = 2\pi \times 90$ Hz. The initial amplitude is 235 μm and decays with a $1/e$ lifetime $\tau = 12$ ms.*

measured trap frequency is less reliable. The measured frequency of 90 ± 2 Hz implies an axial bias field approximately 4.5 G, which is 3 G lower than that expected. This suggests that the end wires lie closer to the atom chip surface than expected, or that the magnetic field is somehow suppressed. This discrepancy has still not been resolved.

The phase of the radial oscillations indicates that they also result from loading the trap off-centre, rather than from imparting a velocity to the cloud during the transfer from the CMOT to the magnetic trap. To account for the shift in height between the CMOT and the magnetic trap, the centre wire current is adjusted when the anti-Helmholtz field is switched off. These two parameters are optimized experimentally to minimize the amplitude of oscillations. In this way, the radial oscillation amplitude is reduced to 125 μm.

Elastic collisions between trapped atoms lead to rethermalization of the oscillating cloud at a higher temperature. We can estimate the temperature rise of the cloud by equating the increase in thermal energy of the cloud to the initial oscillation energy:

$$\Delta T = \frac{1}{2k_B} m\omega^2 x^2 \tag{6.3}$$

The temperature rise due to the residual axial oscillations is only 2.4 μK but the radial oscillation energy corresponds to 30 μK. This can be seen in the temperature

of the cloud measured (by ballistic expansion) after the oscillations are damped away. This is 80 μK: 30 μK higher than the temperature of the CMOT.

In Section 2.3.5, it was shown that the end wire field leads to a rotation of the axis of the magnetic trap. For the parameters of our CMOT/magnetic trap, the magnetic trap is rotated from the x-axis, such that its ends are displaced by $\pm 80\mu$m. This may be the ultimate limit on the efficiency with which atoms can be matched from the CMOT into the magnetic trap, and on the minimization of trap oscillations.

6.3.3 Elastic collision rate

The elastic collision rate in an isotropic gas is defined as:

$$\gamma_{el} = n\sigma_{el}\langle v_{rel}\rangle, \tag{6.4}$$

where σ_{el} is the elastic collision cross-section, n is the atomic density and $\langle v_{rel}\rangle$ is the mean relative velocity between atoms. For a non-uniform spatial distribution of atoms, this expression must be averaged over the cloud:

$$\langle\gamma_{el}\rangle = \langle n\rangle\sigma_{el}\langle v_{rel}\rangle. \tag{6.5}$$

The mean density of a Gaussian cloud of peak density n_0 is:

$$\begin{aligned}\langle n\rangle &= \frac{1}{N}\int\left(n_0\ e^{-(r^2/2\sigma_r^2)}\ e^{-(z^2/2\sigma_z^2)}\right)^2 2\pi r\,\mathrm{d}r\,\mathrm{d}z \\ &= \frac{n_0}{2\sqrt{2}},\end{aligned} \tag{6.6}$$

where the peak density, n_0 is defined by Equation 4.13. For $\langle v_{rel}\rangle$ we use the rms relative velocity: $\langle v_{rel}\rangle = \sqrt{6k_BT/m}$. Substituting for n_0 and $\langle v_{rel}\rangle$ in Equation 6.5, the elastic collision rate becomes:

$$\langle\gamma_{el}\rangle = \frac{N}{2(2\pi)^{3/2}}\sqrt{\frac{3k_BT}{m}}\,\frac{\sigma_{el}}{\sigma_x\sigma_y\sigma_z} \tag{6.7}$$

$$= \frac{\sqrt{3}N}{2(2\pi)^{3/2}}\,\frac{m\omega_r^2\omega_z}{k_BT}\,\sigma_{el}. \tag{6.8}$$

At low temperatures ($T < 30\,\mu$K), collisions are dominated by elastic s-wave scattering, for which the cross-section is given by [120]:

$$\sigma_{el} = \frac{8\pi a^2}{1+k^2a^2}, \tag{6.9}$$

where $k = 2\pi/\lambda_{dB}$, $\lambda_{deB} = h/\sqrt{2\pi m k_BT}$ is the thermal de Broglie wavelength and $a = (5.53 \pm 0.13)$ nm is the scattering length [121]. Below 30 μK we neglect the

term k^2a^2 in the denominator and $\sigma_{el} \Rightarrow 8\pi a^2 = 7.7 \times 10^{-12}\,\mathrm{cm}^2$. Above $30\,\mu$K, this theory predicts a $1/T$ dependence of the collision cross-section. However, Burke *et al* [121] have calculated a full derivation of the Rb scattering cross-sections for various hyperfine states and temperatures. This predicts a total elastic cross-section between ^{87}Rb atoms in the $|2,2\rangle$ ground state which is approximately constant for temperatures $0 < T < 300\,\mu$K. Therefore, we use the value $\sigma_{el} = 7.7 \times 10^{-12}\,\mathrm{cm}^2$ over this complete range.

The collision rate for the cloud of Figure 6.6 ($N = 2 \times 10^7$, $T = 136\,\mu$K, $\omega_z = 2\pi \times 15\,\mathrm{Hz}$, $\omega_r = 2\pi \times 90\,\mathrm{Hz}$) is calculated to be $2\,\mathrm{s}^{-1}$ from Equation 6.7. Since this is within a factor of two of the decay rate of the axial oscillations, $1/\tau = 3.45\,\mathrm{s}^{-1}$, it seems likely that collisions are playing a part there.

6.4 Compressing the magnetic trap to load the microtraps

6.4.1 Adiabatic compression

After transferring atoms from the CMOT to the magnetic trap, the bias field B_{bias} is ramped to its maximum value to increase the depth of the trap and bring it closer to the surface. The centre wire current is then ramped down. At about 12 A, the wire trap merges with the videotape microtraps. Further reduction of the wire current passes the atoms completely to the videotape trap. In order to avoid unwanted heating (which gives a loss of phase space density), it is necessary to perform this compression adiabatically. The condition for adiabatic compression is:

$$\frac{\mathrm{d}\omega_i}{\mathrm{d}t} \ll \omega_i^2. \tag{6.10}$$

This sets a limit on the rate at which the bias field and centre wire current should be ramped. If this condition is fulfilled, phase-space density in the trap will be conserved and the temperature of the atom cloud in a harmonic trap will scale as:

$$T_{final} = T_{initial}\frac{\overline{\omega}_{final}}{\overline{\omega}_{initial}}, \tag{6.11}$$

where $\overline{\omega}$ is the geometric mean of the trap frequencies: $\overline{\omega} = (\omega_x\omega_y\omega_z)^{1/3}$. In contrast, a sudden change of trapping frequency will increase the temperature to:

$$T_{final} = \frac{T_{initial}}{2}\left(1 + \frac{\omega_{final}^2}{\omega_{initial}^2}\right). \tag{6.12}$$

This is obtained by considering the change in potential energy, $U_{final} = U_{initial}\frac{\omega_{final}}{\omega_{initial}}$, due to a sudden change in trap frequency. The new total energy is redistributed between potential and kinetic energy K, until $U_{final} = K_{final} = 3k_BT_{final}/2$.

By limiting the maximum rate of change of bias field and centre wire current to less than $2\,\mathrm{G\,ms^{-1}}$ and $1\,\mathrm{A\,ms^{-1}}$ respectively, the adiabatic condition will be met over the whole range of operating conditions of the magnetic trap. The entire ramp from ($I_{centre} = 15\,\mathrm{A}, B_{bias} = 23\,\mathrm{G}$) to ($I_{centre} = 15\,\mathrm{A}, B_{bias} = 42\,\mathrm{G}$) to ($I_{centre} = 0\,\mathrm{A}, B_{bias} = 23\,\mathrm{G}$) must be carried out in a time longer than 30 ms. Since the lifetime of the magnetic trap is of the order of 5 s (see below), this condition is easily fulfilled.

A further consideration is that the compression is anisotropic and must therefore be slow compared to the elastic collision rate. If this condition is not met, the cloud acquires an anisotropic temperature during compression and there is a loss of phase-space density as the cloud subsequently equilibriates. Equation 6.11 must then be considered separately for each dimension and the overall equilibrium temperature increase is given by:

$$T_{final} = \frac{T_i}{3}\left(\frac{\omega_{x\ final}}{\omega_{x\ initial}} + \frac{\omega_{y\ final}}{\omega_{y\ initial}} + \frac{\omega_{z\ final}}{\omega_{z\ initial}}\right). \tag{6.13}$$

An experiment was performed in which the wire trap was ramped from 15 A, 22.75 G ($\omega_r = 2\pi \times 90\,\mathrm{Hz}$) to 15 A, 42 G ($\omega_r = 2\pi \times 480\,\mathrm{Hz}$) in 500 ms. The atoms were held in the tight trap for 500 ms and then ramped back to the original trap in the same time period. The temperature measured after this was $85.7\,\mu\mathrm{K}$, an increase of only $5\,\mu\mathrm{K}$ from the initial temperature. For comparison, had the trap frequency been jumped suddenly between these two values the temperature would have increased to $230\,\mu\mathrm{K}$.

6.4.2 Loading the microtraps

The number of microtraps into which atoms are loaded depends on the temperature of the cloud and on the exact position and alignment of the centre wire with respect to the videotape magnetization. Figure 6.8 shows the evolution of the magnetic traps with bias field and centre wire current. The column of plots (b) shows magnetic traps for the same conditions as (a) except that the centre wire is displaced, relative to the magnetic mirror, by half a wavelength of the videotape recording. The first contour plot is for the parameters of the magnetic trap into which atoms are loaded from the CMOT. At this stage, the magnetic potential barrier between the trap centre and the videotape is in excess of 20 G. The next two plots depict successive increases of the bias field, which bring the magnetic trap close to the surface. The lowest three plots depict successive decreases of the centre wire current, during which the wire trap merges with a small number of the videotape microtraps. The extent of the cloud depends on its temperature. Clouds of $132\,\mu\mathrm{K}$ or less will be confined

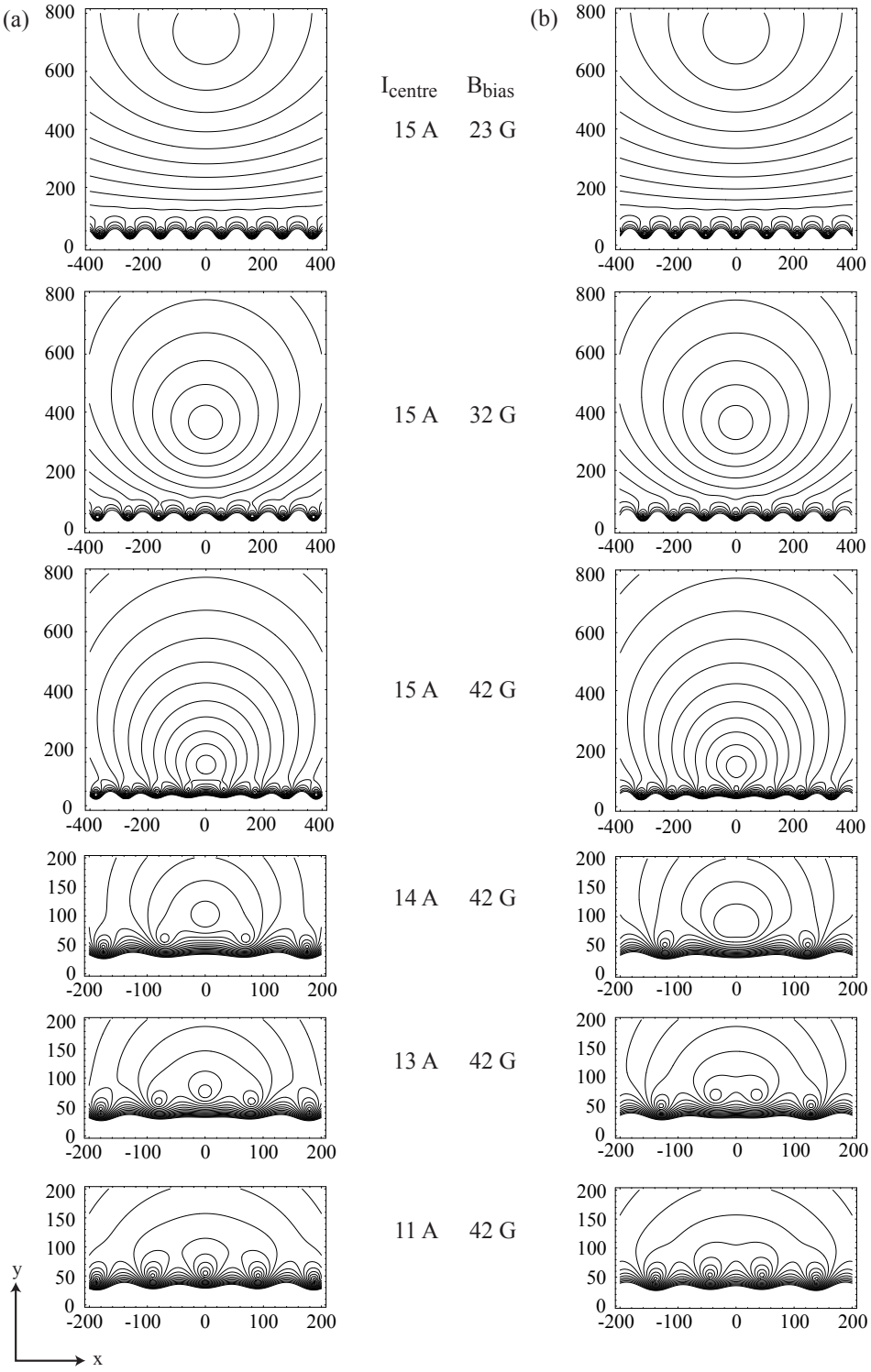

Figure 6.8 *Contour plots of magnetic trapping potentials as bias field and centre wire current are changed to bring the atom cloud close to the surface. Column (a) corresponds to the situation where the wire trap is centred exactly above one of the videotape microtraps. Column (b) corresponds to the situation where the videotape pattern has been shifted by half a wavelength of the recorded magnetization, relative to the centre wire. The surface is located at $y = 0$. The contours correspond to even valued magnetic potentials, from 2 G to 30 G.*

in the region enclosed by the smallest closed contour. In column (a) of Figure 6.8 we see that such a cold cloud will be loaded into just one microtrap. If the position of the centre wire relative to the videotape is displaced by half a wavelength (Figure 6.8(b)), a cold cloud will be split into two separate microtraps as it reaches the surface. Hotter clouds will extend to a larger radius and atoms on the periphery of the cloud will explore several microtraps as the cloud begins to interact with the surface.

6.4.3 Images of the compression sequence

The experimental sequence used to compress the traps from the initial wire trap to the videotape microtraps is as follows: the initial magnetic trap has similar parameters to the CMOT (15 A, 23 G), with small adjustments to prevent oscillations in the trap; the bias field is first ramped to its maximum value of 42 G over 250 ms; the centre wire current is then ramped down to its final value over a further 250 ms. A sequence of images at different stages of compression is shown in Figure 6.9. The images correspond to the magnetic field contour plots shown in Figure 6.8, except that here we are viewing from 45° to the axis of the magnetic traps. The first image of Figure 6.9 is of an atom cloud in a relatively weak magnetic trap, due to the wire and bias field. The radial asymmetry of the magnetic trap is apparent in this first image — the field gradient is weaker to $+y$ of the trap. The clouds become more symmetric as the magnetic field gradient increases. The final image (42 G, 11 A) corresponds to the atom cloud trapped in potentials formed by the videotape magnetic field. At such short distances to the atom chip surface, it becomes very difficult to obtain good quality images of the cloud. However, it is possible to obtain information about the atom number by ramping the current back up to a higher value. In this way, we have observed atom clouds recaptured from traps formed by the videotape and bias field alone, i.e. $I_{centre} = 0$.

6.5 Calibration of the bias field

The bias field, B_{bias}, is produced by currents in two similar, overlapping pairs of square Helmholtz coils, each controlled by a separate FET circuit and power supply. The two circuits share a common voltage input, $V_{control}$, which determines the (unequal) currents in each pair of coils. The field produced by these coils for a given control voltage is calibrated by measuring the relative height of the magnetic trap centre for a fixed centre wire current, I_{centre}, and a range of values of B_{bias}.

For a wire trap, Equation 2.49 gives: $B_{bias} = \mu_0 I_{centre}/2\pi r_0$, where $r_0 = y_0 + d_c$

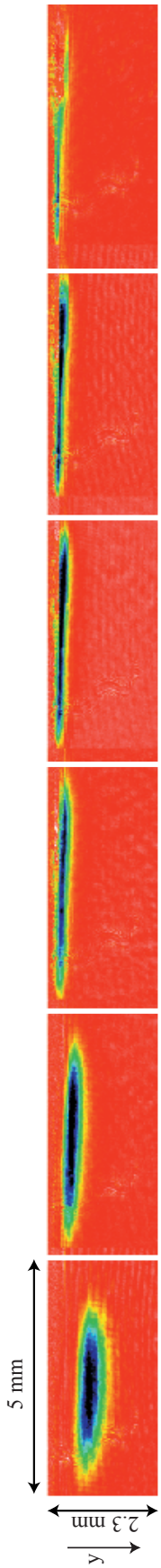

B_{bias} :	23 G	32 G	42 G	42 G	42 G
I_{centre} :	15 A	15 A	15 A	14 A	13 A	11 A
y_0 :	0.73 mm	0.362 mm	0.138 mm	0.102 mm	0.079 mm	0.057 mm
ω_{radial} :	2π x 120 Hz	2π x 260 Hz	2π x 530 Hz	2π x 600 Hz	2π x 1.7 kHz	2π x 4.3 kHz
ω_{axial} :	2π x 15.4 Hz	2π x 15.6 Hz	2π x 15.5 Hz	2π x 15.4 Hz	2π x 15.4 Hz	2π x 15.4 Hz

Figure 6.9 *Absorption images of the magnetic trap at different stages of compression. The images are taken at grazing incidence to the atom chip surface, at an angle of 45° to the axis of the magnetic traps. In the first image, the cloud is at the same height below the surface as the CMOT. In the final image, the magnetic trap is formed by the field of the videotape.*

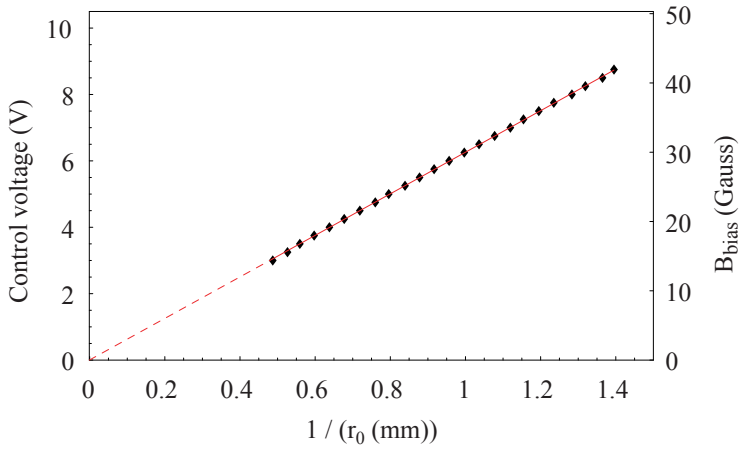

Figure 6.10 *Bias field calibration. Experimental values for $V_{control} = C \times B_{bias}$ plotted against $1/r_0$, for $I_{centre} = 15A$. The constant C is obtained from the gradient of the fit, yielding the values shown for B_{bias} on the right-hand axis. r_0=0 corresponds to the position of the axis of the centre wire.*

is the distance from the trap to the centre wire. (y_0 is the height above the surface and d_c is the depth of the centre wire axis below the surface.) The bias field is proportional to the control voltage of the corresponding FET circuit: $B_{bias} = C \times V_{control}$, where C is a constant.

Figure 6.10 is a plot of $V_{control}$ against the inverse measured trap height, $1/r_0$, for constant $I_{centre} = 15$A. The magnetic trap height was originally measured relative to the CCD chip field of view. The height scale has been shifted until the straight line fit passes through the origin, such that $r_0 = 0$ now refers to the position of the centre wire. Given that $B_{bias} = \mu_0 I_{centre}/2\pi r_0$, the gradient of Figure 6.10 is equal to $\mu_0 I/2\pi C$. This yields the calibration: $B_{bias}(\text{Gauss}) = 4.76\, V_{control}$. This calibration is shown on the right-hand axis of Figure 6.10.

6.6 Calibration of the surface position

To bring the atoms into the region where the magnetic trap is formed by the field of the videotape, the centre wire current must be reduced. Having calibrated the bias field (and the centre wire position relative to the camera field of view), measurements of trap position against wire current enable the position of the magnetic surface to be determined. This measurement will therefore yield a value for d_c, the depth of the centre wire below the surface. This is more reliable than measuring the surface position directly from an image: the front edge of the mirror surface is out of focus

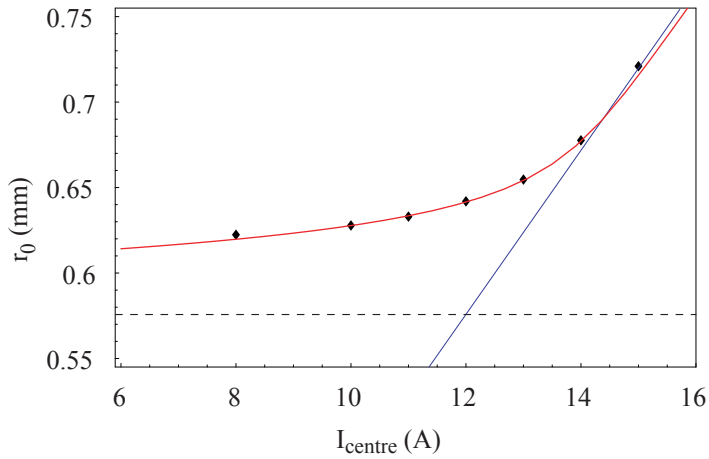

Figure 6.11 *Mirror height calibration. Experimental values for magnetic trap position (relative to centre wire) plotted against I_{centre}, for a constant bias field $B_{bias} = 42\,G$. The straight line (blue) shows the calculated variation of height with current for a wire trap in the absence of the videotape surface, based on Equation 2.49. The curve (red) is a fit to Equation 6.14, for the trap position close to the magnetized videotape surface. The dashed line shows the position of the surface, obtained from the fit.*

and there is diffraction of the absorption imaging beam at the surface, both of which distort the image. Figure 6.11 shows the variation of magnetic trap position, r_0, with centre wire current, for a constant bias field of 42 G. The trap position, r_0, has been adjusted using the previous calibration (Section 6.5) such that $r_0 = 0$ corresponds to the centre wire position. The straight line is calculated using the calibration of Section 6.5 and indicates the expected behaviour of the trap position for a wire trap, i.e. if the magnetized surface were not present. In the region of the videotape field, the magnetic trap zero forms where the effective bias field cancels the videotape field. In this case, the effective bias field is the sum of $B_{bias} = 42\,\mathrm{G}$ and the opposing field due to the centre wire at the measured position of the magnetic trap. Using Equation 2.45:

$$r_0 = \frac{\lambda_M}{2\pi} \ln \left(\frac{B_1}{B_{bias} - \left(\frac{\mu_0 I_{centre}}{2\pi r_0} \right)} \right) + d_c. \tag{6.14}$$

This equation is fitted to the data in Figure 6.11. The fit parameters were the surface height, d_c, and the magnetization wavelength, λ_M, which also determines B_1, the surface field, through Equation 2.42. The fit gives a recorded wavelength of 105 μm, in agreement with the measured value of $106 \pm 2\,\mu$m (Section 4.1.4). The fitted

mirror position, $d_c = 0.576\,\mathrm{mm}$. From the construction of the magnetic mirror, we had expected this value to be approximately $450\,\mu\mathrm{m}$ (the summed thicknesses of the glass coverslip ($150\,\mu\mathrm{m}$), the videotape ($15\,\mu\mathrm{m}$), the centre wire radius ($250\,\mu\mathrm{m}$) and a small allowance for the thickness of the glue). We attribute the difference to a slight bow in the mirror, due to it being stuck more firmly at the edges than at the centre, which can be seen when looking at light reflected from the gold surface.

6.7 Measurement of the residual field

The residual axial field, B_0 determines the radial trap frequency, through Equation 2.59 in the harmonic region of the trap. This field can be measured using an rf technique.

An rf field of frequency ν_{rf} is resonant with the $\Delta m_F = \pm 1$ spin-flipping transition for atoms at a magnetic potential $B = h\nu_{rf}/\mu_B g_F \Delta m_F$. Atoms which interact with the rf field are rapidly transferred to untrapped m_F states and leave the magnetic trap. Since $g_F = 1/2$ for the trapped state, the resonance condition becomes $B(\mathrm{Gauss}) = \nu_{rf}(\mathrm{MHz})/0.7$.

Rf frequencies corresponding to a magnetic field greater than the maximum field of the trap, or smaller than the minimum field, have no effect on the atom number,

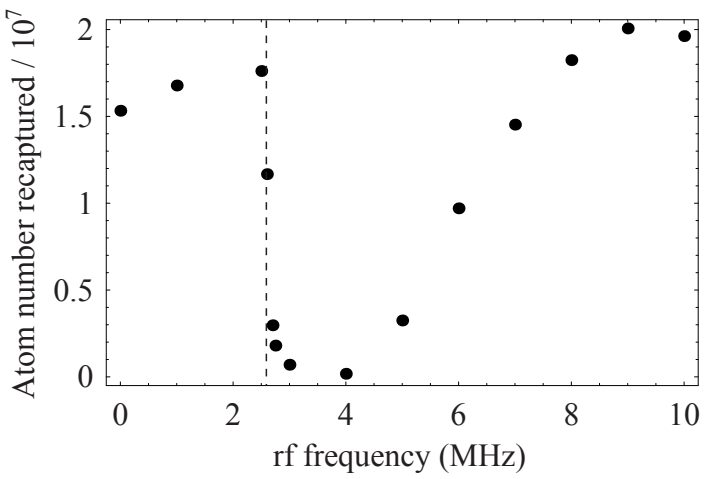

Figure 6.12 *Measurement of the residual magnetic field by rf spectroscopy. An rf pulse is applied for 1 s while the atoms are in the magnetic trap. The atoms are imaged after recapture in the MOT to obtain an atom number. For the data shown, the magnetic trap is 1 mm from the surface, and the end wire current is 20 A. The cut-off frequency is 2.5 MHz, corresponding to a field of 3.6 G.*

since no atoms interact. As the rf frequency is increased from zero, there is a sharp turn-on of atom loss when the rf frequency becomes resonant with the field at the bottom of the trap, as shown in Figure 6.12. The density of atoms is highest in the region of minimum field and so this rf frequency leads to maximum loss rate from the trap. As the rf frequency is increased further, the loss rate decreases. Above 8 MHz, the loss rate is too small to see over the 1 s interval used in the experiment. This measurement is generally repeated for each magnetic trap height, as the residual magnetic field has a height dependence. We note that the turn-on of atom loss is less sharp when this method is used to look at traps with high vibration frequencies.

This method was also used to calibrate the field produced by the axial cancelling field coils. By measuring the residual field for a range of currents, a calibration of $3.83\,\mathrm{G\,A^{-1}}$ was obtained, as stated in Table 4.1.

6.8 Lifetime of the magnetic trap: 3-body loss

The lifetime of the magnetic trap is an important experimental parameter as it ultimately limits the time available for a given experiment. There are several processes which can lead to loss of atoms from the magnetic trap. Elastic collisions between cold, trapped atoms and hot, background atoms gives a loss rate, γ, which is independent of the density of the atom cloud and is proportional to the number of atoms in the trap. It is a good indication of the background pressure in the vacuum chamber. In addition, inelastic collision processes can contribute to decay from the magnetic trap. The most important of these are two-body spin relaxation and three-body recombination. The first occurs when the magnetic dipole interaction during a collision between two trapped atoms leads to a spin flip which releases energy. This is possible if atoms are prepared in a hyperfine state which is not the lowest atomic state, which is the case in this experiment. (The rate is greatly suppressed for atoms trapped in the lower hyperfine level.) For such 2-body processes, the probability per unit time that an atom is expelled from the trap is proportional to $n^2(\mathbf{r})$, where $n(\mathbf{r})$ is the local density of the atom cloud. In the second process, two atoms can form a dimer, generally in an excited vibrational state, with the excess (binding) energy carried away by a third atom (Rb + Rb + Rb $\rightarrow$ Rb_2^* + Rb). Since this energy is generally much larger than the depth of the magnetic trap, all three atoms are lost in the process. The probability per unit time for this process is proportional to $n^3(\mathbf{r})$.

The rate equation for the local density, $n(\mathbf{r})$, is therefore:

$$\frac{\mathrm{d}n(\mathbf{r})}{\mathrm{d}t} = -L_2\, n^2(\mathbf{r}) - L_3\, n^3(\mathbf{r}) - \gamma n(\mathbf{r}), \tag{6.15}$$

where γ is the background loss rate, L_2 is the 2-body loss rate and L_3 is the 3-body loss rate. The total loss rate of atoms is found by integrating this equation over the volume of the cloud:

$$\frac{\mathrm{d}N}{\mathrm{d}t} = -\int L_2\, n^2(\mathbf{r})\, \mathrm{d}^3r - \int L_3\, n^3(\mathbf{r})\, \mathrm{d}^3r - \gamma N, \tag{6.16}$$

where N is the total number of atoms in the cloud. We define a density-weighted average of a function $\eta(\mathbf{r})$ as:

$$\langle \eta(\mathbf{r}) \rangle = \frac{1}{N} \int \eta(\mathbf{r})\, n(\mathbf{r})\, \mathrm{d}^3r. \tag{6.17}$$

This allows us to rewrite Equation 6.16 as:

$$\frac{1}{N}\frac{\mathrm{d}N}{\mathrm{d}t} = -L_2 \langle n \rangle - L_3 \langle n^2 \rangle - \gamma, \tag{6.18}$$

where $\langle n \rangle$ and $\langle n^2 \rangle$ are the mean density and mean square density respectively.

The lifetime of a given magnetic trap is determined by measuring the number of atoms remaining in the trap as a function of trapping time. The imaging process is destructive, so the measurement is repeated for each of several trapping times. Atoms are loaded into the magnetic trap as described above and the trap is then compressed to its final parameters by ramping the bias field and centre wire current over 500 ms. After the trapping time has elapsed, the magnetic trap is ramped back to its initial parameters. The trap is immediately switched off and the atom number is measured by resonant absorption imaging in a uniform field.

The decay curve of the cloud in the initial wire trap ($I = 15\,\mathrm{A}$, $B_{bias} = 22.75\,\mathrm{G}$, $B_0 = 2\,\mathrm{G}$) is shown in Figure 6.13. This decay is shown to fit well to an exponential

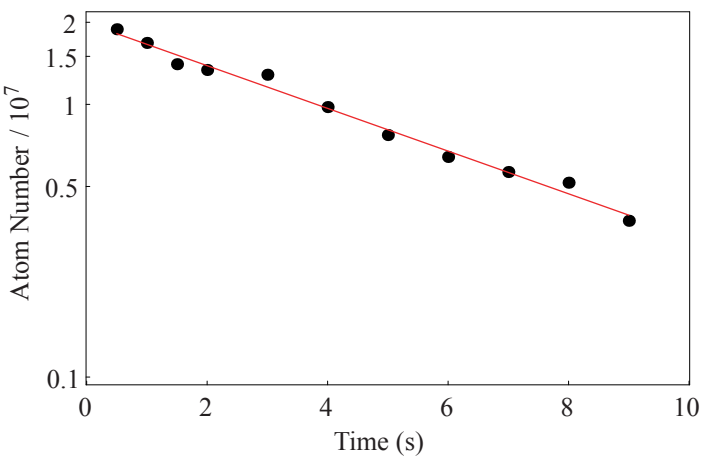

Figure 6.13 *Measurement of the magnetic trap lifetime. ($B_{bias} = 22.75\,G$; $I_{centre} = 15\,A$; $I_{end} = 18.5\,A$.) The exponential fit gives a lifetime of 5.6 s.*

loss, $N(t) = N(0)\exp(-t/\tau)$, indicating that the loss process is independent of density. The lifetime, τ, was measured to be typically 5.5 s. There are various factors which can reduce the magnetic trap lifetime. Stray light which enters the chamber can drastically reduce the magnetic trap lifetime by optical excitation of the atoms. Spontaneous decay results in the majority of atoms returning to an untrapped groundstate and therefore being lost from the trap. Every effort was made to ensure that no scattered laser light from the optical table reached the vacuum chamber, including installing an additional mechanical shutter closer to the slave laser, and shielding the laser beam paths close to the chamber. A second factor which may have reduced the lifetime was residual emission of rubidium from the dispenser when the dispensing pulse was initially switched 'off' (i.e. at 2.5 A). For this reason, the dispenser current was switched off to zero amps, rather than to its 'standby' current of 2.5 A after filling the MOT. This increased the cooling rate of the dispenser such that its emission was reduced in a shorter time. These measures increased the magnetic trap lifetime from ~ 1 s to its present value of 5.5 s.

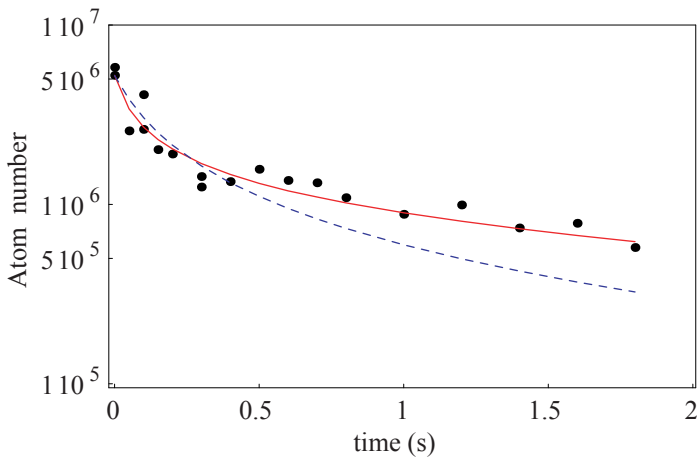

Figure 6.14 *Decay curve for magnetic trap at high density ($B_{bias} = 42$ G, $I_{centre} = 2$ A, I_{end}=20 A, $y_0 = 30.5\,\mu$m). The red solid line is a fit to the experimental data using Equation 6.23 for 3-body loss. This fit implies an initial density of 7.8×10^{14} cm^{-3}. The blue dashed line is the best fit to the 2-body loss solution, Equation 6.22, which clearly does not reproduce the experimental data.*

After compressing the magnetic trap until the atoms were interacting with the field of the videotape ($B_{bias} = 42$ G, $I_{centre} < 11$ A), decay curves such as Figure 6.14 were observed. At short times, the decay process clearly deviates from exponential, indicating that the density-dependent processes included in Equation 6.18 are being observed.

The 2-body loss rate, L_2, is calculated by [122] to be within the range (0.4 –

$0.7) \times 10^{-15}\,\mathrm{cm}^3\,\mathrm{s}^{-1}$ in zero magnetic field[1] and to increase by a factor of three in a field of 1 G.

The 3-body loss rate, L_3, has been accurately measured for Bose-condensed ^{87}Rb atoms, spin-polarized in the $F = m_F = 2$ state by [123], as $(1.8\pm0.5)\times10^{-29}\,\mathrm{cm}^6\,\mathrm{s}^{-1}$. For thermal clouds of atoms, this loss rate is a factor of 3! higher, a result predicted by theory [124] and confirmed experimentally in caesium [125]. This factor arises due to higher order coherences in condensates, which lead to a suppression of density fluctuations. We therefore use the value $L_3 = (1.1 \pm 3) \times 10^{-28}\,\mathrm{cm}^6\,\mathrm{s}^{-1}$, which is in excellent agreement with the theoretical value given in [126].

In order to rewrite the right-hand side of Equation 6.18 in terms of atom number, N, we must first evaluate $\langle n \rangle$ and $\langle n^2 \rangle$. Using Equation 6.17, and the density expression given in Equation 4.12, we obtain:

$$\begin{aligned} < n > &= \frac{1}{N} \int \left(n_0 \; e^{-(r^2/2\sigma_r^2)} \; e^{-(z^2/2\sigma_z^2)} \right)^2 2\pi r \, \mathrm{d}r \, \mathrm{d}z \\ &= \frac{n_0}{2\sqrt{2}}, \end{aligned} \tag{6.19}$$

where $\sigma_r = \sigma_x = \sigma_y$. The mean square density is similarly evaluated, yielding:

$$< n^2 > = \frac{n_0^2}{3\sqrt{3}}. \tag{6.20}$$

The peak density n_0 is given by Equation 4.13: $n_0 = \frac{N}{(2\pi)^{3/2}\sigma_r^2\sigma_z}$. We define the volume of the magnetic trap as $V_0 = (2\pi)^{3/2}\sigma_r^2\sigma_z$. Then the peak density of the Gaussian distribution is $n_0 = N_0/V_0$. We therefore rewrite Equation 6.18 as:

$$\frac{1}{N}\frac{\mathrm{d}N}{\mathrm{d}t} = -\frac{L_2\,N}{2\sqrt{2}\,V_0} - \frac{L_3\,N^2}{3\sqrt{3}\,V_0^2} - \gamma. \tag{6.21}$$

It has not proved possible to find an analytic solution to Equation 6.21 to include both 2-body and 3-body loss mechanisms, but we can solve the equation for either loss mechanism separately. Writing $\frac{L_2}{2\sqrt{2}\,V_0} = C_2$ and setting the boundary condition $N = N_0$ at $t = 0$, we obtain the solution for 2-body loss alone:

$$N(t) = \frac{N_0\gamma}{\gamma\, e^{\gamma t} + C_2 N_0\, e^{\gamma t} - C_2 N_0}. \tag{6.22}$$

Similarly, with $\frac{L_3}{3\sqrt{3}\,V_0^2} = C_3$, we obtain the solution for 3-body loss alone:

$$N(t) = \frac{N_0\sqrt{\gamma}}{\sqrt{\gamma + C_3 N_0^2}\,\sqrt{e^{2\gamma t} - \frac{C_3 N_0^2}{\gamma + C_3 N_0^2}}}. \tag{6.23}$$

[1] a factor of 2 – 4 greater than that given in [121].

I_{centre} (A)	$\omega_r/2\pi$ (kHz)	C_3 ($m^3\,s^{-1}$)	V_0 ($10^{-8}\,cm^3$)	N_0 (10^6)	n_0 (cm^{-3})	T_{fit} (μK)	$T_{adiabatic}$ (mK)
4	29	1.2×10^{-14}	4.17	6.1	1.5×10^{14}	440	3.8
3	31	7×10^{-14}	1.74	7	4×10^{14}	270	3.9
2	34	4.9×10^{-13}	0.66	5.2	8×10^{14}	160	4.2
1	36	2.5×10^{-12}	0.29	6	2×10^{15}	100	4.3

Table 6.1 *Results of fit to 3-body loss. The axial trap frequency is constant at 15 Hz. The radial trap frequencies are calculated for the listed values of I_{centre}, with $B_{bias} = 42\,G$ and $I_{end} = 20\,A$. N_0 is measured directly by absorption imaging; C_3 is determined from the fit; V_0, n_0 and T_{fit} are calculated from N_0 and C_3 as described in the text. $T_{adiabatic}$ is calculated from Equation 6.11, given the initial and final trap frequencies.*

Equations 6.22 and 6.23 are each used to generate a fit to the decay curve shown in Figure 6.14. The 2-body loss equation (Equation 6.22) does not replicate the experimental curve well, whereas the 3-body loss equation (Equation 6.23) does. This clearly shows that the density-dependent loss we observe is due to 3-body loss, which agrees with the observations of [123] for a Rb condensate. The fitted value of C_3 implies an initial peak density of $7.8 \times 10^{14}\,cm^{-3}$.

Several such decay curves were obtained at the same bias field of 42 G, with centre wire currents of 4 A, 3 A, 2 A and 1 A, as listed in Table 6.1. The height of these traps above the surface ranges from 29 μm to 34 μm. The axial trap frequency was fixed at 15 Hz, but the radial trap frequency varied from 29 kHz to 36 kHz, with lower current giving a tighter trap. The fitted values for C_3 give values for the trap volume, V_0. Using this value of V_0, together with the fitted value of N_0, the peak density at $t = 0$ can be obtained: $n_0 = N_0/V_0$. We see that n_0 varies by more than an order of magnitude, reaching a very high value of $2 \times 10^{15}\,cm^{-3}$ when I_{centre}=1 A. Knowledge of the trap frequencies then leads to an estimate of the temperature of the cloud at $t = 0$. Rearranging Equation 6.2 gives:

$$T = \frac{m\overline{\sigma}^2\overline{\omega}^2}{k_B}, \tag{6.24}$$

where $\overline{\sigma}$ and $\overline{\omega}$ represent the geometric mean of these values, i.e. $\overline{\sigma} = (\sigma_r^2\,\sigma_z)^{1/3}$ and $\overline{\omega} = (\omega_r^2\,\omega_z)^{1/3}$. Substituting $V_0 = (2\pi)^{3/2}\,\overline{\sigma}^3$, we obtain:

$$T = \frac{m\,\overline{\omega}^2}{2\pi k_B}(V_0)^{2/3}, \tag{6.25}$$

which leads to cloud temperatures between 400 μK and 100 μK. These temperatures are much lower than those calculated using Equation 6.11 for adiabatic compression,

which are of the order of 4 mK. We believe that this is due to evaporative cooling (see Section 6.10) which should take place due to the finite trap depth. The trap depth is limited by the axial depth, ~ 25 G, which is equivalent to a temperature of 1.7 mK. The temperatures stated in Table 6.1 for adiabatic compression are well in excess of this. We would therefore expect strong cooling due to evaporation of atoms from the ends of the trap.

This method of obtaining the temperatures of the cloud is somewhat indirect. Unfortunately, it is not possible to image clouds which are trapped so close to the surface, so it is difficult to verify these low temperatures directly.

6.9 Lifetime measurements: investigation of surface interactions

It was discussed in the introduction, that the motivation for designing atom chips is to miniaturize trapping potentials for atoms. The advantages of miniaturization are only realized at short distances from the surface, of order the scale of the small features which generate the micropotentials. We expect that as atoms are brought closer to the surface, there will be a region close to the surface in which we will no longer be able to neglect the effects of the surface on the trapped atom cloud.

We have measured the low-density lifetime in magnetic traps at a range of heights above the surface. The lifetime measurements were made as described in Section 6.8. Looking at Figure 6.14, we see that the loss rate tends to a constant value γ at long times, as the atom number decreases. It is from this region of the decay curve that we obtain values for the low-density lifetime.

The results we obtained are presented in Figure 6.15. We have measured magnetic trap lifetimes over a range of heights, from 30 μm to 1 mm. The error bars displayed represent the uncertainty in fitting the low-density lifetime, estimated to be about 10%. Within the error bars of our data, we observe no dependence of the lifetime on distance to the surface. The mean lifetime is 5.5 s, indicated by the solid line in Figure 6.15.

Similar lifetime measurements close to a surface have been made by the group of Claus Zimmermann [38]. In Zimmermann's experiment, the microtraps were formed by adding a uniform bias field to the field above both a microfabricated copper conductor and above a 90 μm diameter copper wire. The data they obtained is reproduced in Figure 6.16 and shows a dramatically different result from our observations: the lifetime was seen to decrease linearly with distance from the wire, from 20 s at 300 μm, to 700 ms at 20 μm. In order to compare their data more closely with ours,

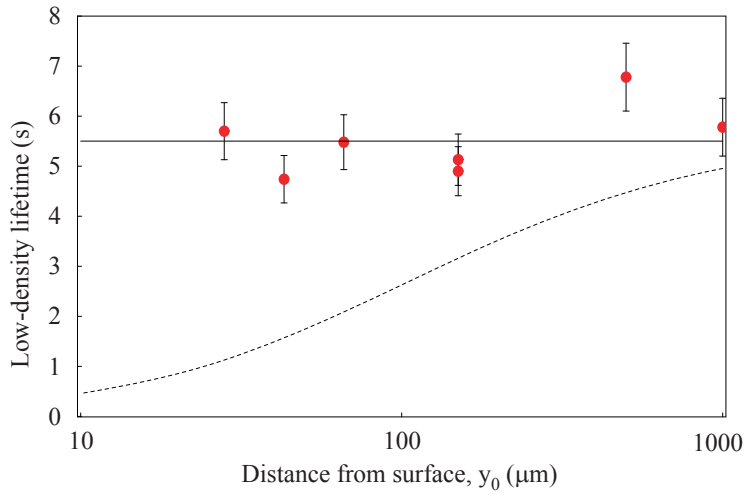

Figure 6.15 *Magnetic trap lifetime variation with height above surface. The plotted lifetimes are obtained at low density, where the 3-body loss rate is negligible. The points represent data from this experiment; the solid line is a mean value for the lifetime, 5.5 s. The dotted line represents lifetime data from an experiment where atoms are trapped in microtraps above a copper wire. This data is adjusted as discussed in the text, to allow for the difference in far-distance lifetimes observed between the experiments.*

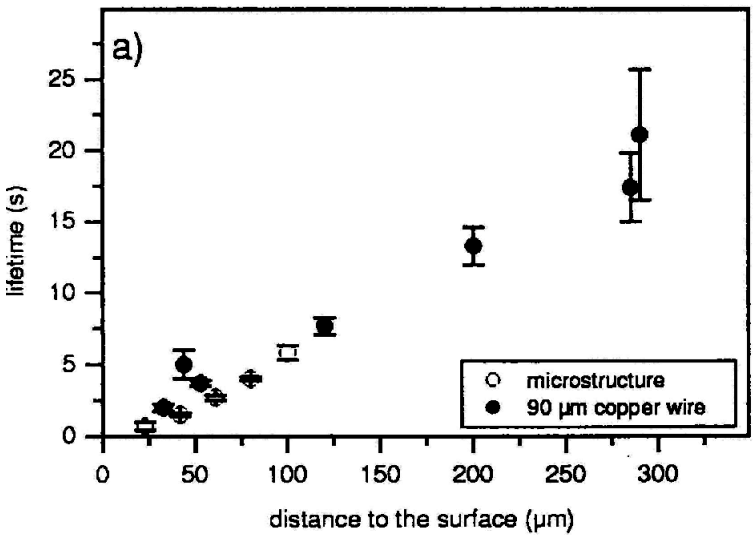

Figure 6.16 *Data published by Fortágh et al [38] for magnetic trap lifetime variation with height above a copper wire. The data was obtained for clouds of atoms at a temperature of 1.5 μK. The lifetime at a distance of 2 mm is 100 s.*

we need to take into account the different lifetimes measured at large distances from the surface, where we can be sure that surface interactions are not important. This difference in far-distance lifetime is due to different background pressures in the two experiments. In Zimmermann's experiment, the lifetime at 2 mm from the surface is 100 s, which is significantly longer than the 5.5 s we measure. To directly compare the two sets of data, we therefore incorporate our shorter background lifetime into their measured data.

In both experiments, we can consider the measured lifetime to result from a background loss rate $\gamma_b = 1/\tau_b$ and a loss rate to the surface $\gamma_s = 1/\tau_s$. The measured lifetime can then be expressed as $\tau = 1/(\gamma_b + \gamma_s)$. In order to say how Zimmermann's wire trap would behave in our vacuum, we therefore adjust their data to incorporate our background lifetime in the following way:

$$\frac{1}{\tau_{copper}} = \frac{1}{\tau_1} + \frac{1}{\tau_2},$$

where τ_1 is the lifetime measured by [38] and τ_2 is our far-distance lifetime, 5.5 s. In this way, the data from [38] has been used to generate the dotted line in Figure 6.15, which shows the behaviour expected for atoms trapped above a copper conductor. Comparing our data with this, we see that the behaviour of trapped clouds of atoms above videotape is very different from that above copper.

Atom loss is expected above a metal because thermally driven currents in the metal produce rf fields that induce spin flips of the atoms [37]. The currents responsible are those within a skin depth of the surface, which is $\sim 100\,\mu$m at the relevant MHz frequencies. These lead to fluctuations in the field above the surface. Our experiments show that this spin flip loss does not occur above the videotape chip. This is an exciting discovery. We believe that the long lifetime is due to the fact that the videotape is a dielectric, in which thermal currents are much smaller. Of course, there is a layer of gold on top of the videotape, however this is only ~ 100 nm thick, and therefore the fluctuating fields are ~ 1000 times smaller than one has above a bulk metal.

It should be noted that the data presented in Figure 6.15 corresponds to a wide range of radial trap frequencies (150 Hz – 22 kHz). To be sure that the trap frequency was not affecting the lifetime measurements, the lifetime was measured at the same height for two very different frequencies. (To increase the trap frequency at a fixed height, I_{centre} and B_{bias} are increased while keeping the ratio I_{centre}/B_{bias} constant.) These measurements are shown in Figure 6.15 at $150\,\mu$m and correspond to frequencies of 800 Hz and 1600 Hz. The difference in measured lifetime is much smaller than the error bar, indicating that the trap frequency plays no role in de-

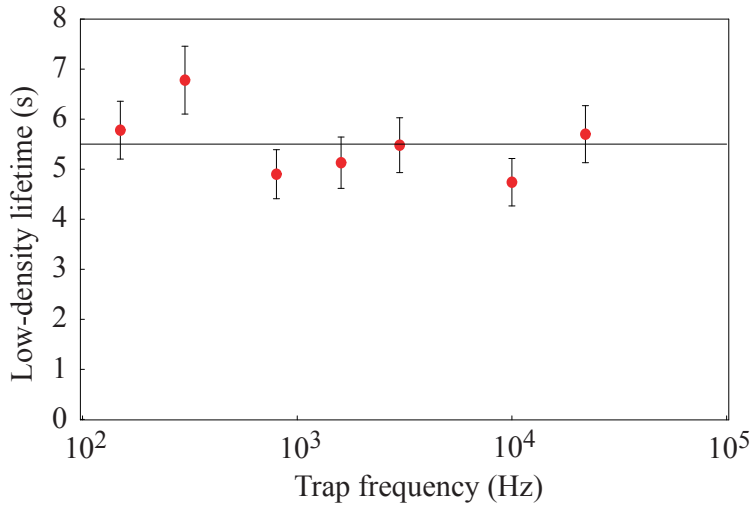

Figure 6.17 *Magnetic trap lifetime variation with trap frequency.*

termining the lifetime here. This same full set of lifetime measurements is plotted against radial trap frequency in Figure 6.17. Again, the data is consistent with a constant value, independent of trap frequency.

6.10 Rf-evaporative cooling

6.10.1 Overview

Now that we have demonstrated that we can load the videotape microtraps, the next step of the experiment is to evaporatively cool the atoms. The ultimate goal of reaching BEC on the atom chip requires more time than was available for this thesis. However, we will show here that we can already evaporatively cool atoms to $10\,\mu$K in the magnetic trap.

Evaporative cooling [127] works by selectively removing atoms which have a higher than average total energy, leaving the rest to rethermalize by elastic collisions. It is the same process we observe as a natural phenomenon, for example as a cup of tea cools — this process is replicated in a magnetic trap. A trapped cloud of atoms in thermal equilibrium is described by the Maxwell-Boltzmann distribution. The mean kinetic energy per atom in any degree of freedom is $k_BT/2$, which is generally much smaller than the depth of the magnetic trap. However, elastic collisions between trapped atoms redistribute the energy such that occasionally a single atom has sufficient kinetic energy to escape from the magnetic trap. In doing so, this atom carries away more than its share of the total energy. The mean energy per atom is reduced and the cloud rethermalizes by elastic collisions to a lower temperature.

This was the mechanism that cooled the atom clouds from 4 mK down to 100 μK in Section 6.8.

The rate of this process can be increased by forced evaporation, in which the effective depth of the trap is lowered in a controlled manner. In order to cool further down to 10 μK, we therefore use an rf field to drive the hottest atoms from the trapped Zeeman substate, $|F = 2, m_F = 2\rangle$, to an untrapped substate, $|F = 2, m_F = 0, -1, -2\rangle$, through a sequence of $\Delta m_F = -1$ transitions, after which they are immediately lost from the trap. The resonance condition for these transitions is:

$$h\nu_{rf} = g_F \mu_B B. \tag{6.26}$$

At fixed rf frequency, ν_{rf}, transitions take place on a surface defined by the magnetic field strength, B, according to Equation 6.26. This evaporation surface is energy selective, since only atoms with sufficient total energy are able to explore this region of the magnetic trap. In a simple model of evaporative cooling, it is assumed that all atoms with total energy $E \geq h(\nu_{rf} - \nu_0)$ are lost from the magnetic trap, where $E_0 = h\nu_0 = m_F g_F \mu_B B_0$ is the potential energy of atoms at the magnetic field minimum. In this way, the rf field effectively limits the trap depth. Rf evaporation works on the same principle as the rf spectroscopy method used in Section 6.7 to determine the minimum field of the magnetic trap. In Figure 6.12, we saw that the greatest loss of atoms occurs when the rf field is tuned to resonance with magnetic fields close to the minimum of the magnetic trap, i.e $h\nu_{rf} \gtrsim m_F g_F \mu_B B_0$. To evaporatively cool, we shall use rf fields tuned to magnetic fields close to the top of the magnetic trap, which produce small loss rates, as shown in Figure 6.12. In this way, only the most energetic atoms are removed from the magnetic trap.

The truncation parameter, η, is introduced to describe the rate of evaporation, such that all atoms with energy $\epsilon = E/k_B T > \eta$ are lost from the trap. As the evaporation progresses, the temperature drops, and the evaporation rate is exponentially suppressed. The rf frequency must therefore be gradually decreased in order to maintain the rate of cooling.

The goal of evaporative cooling is to reach low temperatures with the minimum loss of atoms. In the absence of other loss processes, the efficiency of evaporative cooling depends solely on the choice of truncation parameter: in theory, one could use a very high truncation parameter, and wait a sufficiently long time until all the energy is transferred to a single atom. The loss of this atom from the trap would be accompanied by a huge drop in the temperature of the cloud. In practice, the finite lifetime of the trapped cloud requires that evaporation be carried out more rapidly. This reduces the efficiency of the process: using a lower truncation

parameter reduces the mean energy loss per evaporated atom.

We can write a loss rate for atoms during the evaporation:

$$\frac{1}{N}\frac{\mathrm{d}N}{\mathrm{d}t} = -\gamma_{ev} - \gamma_{loss} \tag{6.27}$$

Here, γ_{ev} represents the loss due to 'good' collisions — that is, elastic collisions between trapped atoms, which lead to evaporation. γ_{loss} is the instantaneous loss rate due to 'bad' collisions. This includes elastic collisions with background gas species and inelastic collisions within the trap. These collisions do not contribute to any net cooling of the cloud.

Evaporative cooling is most efficient for a large ratio of 'good' to 'bad' collisions, proportional to $\gamma_{el}/\gamma_{loss}$. Despite the necessary loss of atoms due to evaporation, there exists a range of initial conditions for $\gamma_{el}/\gamma_{loss}$ and η such that both the collision rate and the phase-space density at the centre of the trap grow exponentially. This regime is known as *runaway* evaporation. If the rf frequency trajectory is not optimized for this, the loss of atoms outweighs the effects of cooling: the collision rate drops exponentially and no further increase in phase-space density is possible. Using the model described in [128], the minimum initial condition required for runaway evaporation is calculated to be $\gamma_{el}/\gamma_{loss} > 150$ [106]. The evaporation of ^{87}Rb in magnetic traps is typically carried out in a time $\sim 10\,\mathrm{s}$, in a trap with lifetime $\sim$1 minute [127], the time scale being set by the initial value of γ_{el}. Such long evaporation times require a background pressure of $\sim 10^{-11}$ Torr. A significant advantage of our miniaturized magnetic trap is that much higher trap frequencies can be reached, which leads to high elastic collision rates (Equation 6.7) and rethermalization times. This is favorable for evaporative cooling, as it can be carried out much faster, thereby permitting shorter lifeimes and hence relaxing the vacuum requirement.

6.10.2 Measuring the temperature of magnetically trapped clouds

Once an atom cloud is trapped in a videotape microtrap, it becomes experimentally very difficult to measure the cloud temperature by ballistic expansion as described in Section 5.1.2. When the bias field and wire currents are switched off to expand the cloud ballistically, the atoms find themselves in the strong exponential field of the magnetic mirror and are accelerated away from the surface, gaining a large kinetic energy, equivalent to the applied bias field. An alternative method could be to switch off only the axially confining magnetic field due to the end wire currents. The rate of axial expansion of the cloud along the magnetic guide could then be

used to calculate the temperature of the cloud. This, too, is difficult for our long clouds, due to the limited field of view of the imaging system.

However, the spatial distribution of atoms in the magnetic trap is determined by the trap frequencies and the cloud temperature, through Equation 6.2. Therefore, if we can measure the size of a magnetically trapped cloud, we can infer its temperature. The length is the most useful dimension here, because the axial trap frequency can be measured accurately (Section 6.3.1) and varies by only $\sim 1\%$ over the range of heights of the magnetic trap (Section 2.3.4).

Unfortunately, this method also fails when the cloud temperature is larger than the natural linewidth of the transition (6.07 MHz$\equiv$ 290μK). In that case, the inhomogeneous trapping potential Zeeman shifts the atoms in the wings of the cloud out of resonance with the imaging beam. An absorption image of such a hot cloud then appears artificially narrow. These Zeeman shifts become small for sufficiently cold clouds, and it is then possible to infer the cloud temperature from the axial profile of a single image of the trapped cloud.

We can estimate the maximum temperature for which this method will be valid, by requiring that atoms at a distance $2\sigma_z$ from the trap centre are Zeeman shifted by less than the natural linewidth of the transition: $\mu_B B_z(2\sigma_z) < h\Gamma$. In the harmonic region of the trap, the axial field varies as:

$$\begin{aligned}\mu_B B_z(z) &= \frac{1}{2} m\omega_z^2 z^2 \\ &= \frac{1}{2} k_B T \frac{z^2}{\sigma_z^2},\end{aligned}$$

where Equation 6.2 was used to substitute for ω_z. The requirement stated above then gives a minimum temperature of 145 μK.

6.10.3 Cooling the atom cloud

The forced evaporative cooling is carried out by driving an oscillating current in the rf antenna (exactly as described in Section 4.5.4). This produces an oscillating magnetic field which is approximately linearly polarized perpendicular to the axial field of the magnetic trap and can drive $\Delta m_F = \pm 1$ transitions. The magnetic trap is loaded as described above, then ramped to $B_{bias} = 42$ G, $I_{centre} = 15$ A. The initial rf frequency is chosen to be 20 MHz, which corresponds roughly to the field over which atoms escape at the ends of the trap. The frequency is then swept down to a final value over a period of 5 s. At the end of the ramp, the cloud is imaged in the trap by absorption imaging and the temperature inferred from the axial width of the cloud.

Figure 6.18 shows images of the cloud obtained after ramping the rf field to successively lower frequencies. The final rf frequency ν_{rf} is given to the right of each image. Figure 6.18 shows that as the final frequency of the rf ramp is reduced, the atom cloud becomes narrower, implying that the temperature of the cloud is dropping, according to Equation 6.2. Prior to evaporative cooling, the clouds we have imaged have been too hot to distinguish different temperatures — hot clouds extend to the region of the magnetic trap where the Zeeman shifts are sufficient to tune the atoms out of resonance with the imaging beam. Now, for the first time, we observe a change in the length of the cloud. We can therefore use the measured length of the clouds to derive the cloud temperatures, as discussed in Section 6.10.2. The calculated temperatures are shown to the right of the images. The minimum temperature reached by this experiment is $10\,\mu$K.

A plot of temperature against final rf frequency is shown in Figure 6.19. The data fits very closely to a straight line. Since the final rf frequency limits the depth of the magnetic trap, the temperature of the cloud is expected to be related to the final rf frequency in this way. Above some temperature, we would expect the temperatures inferred from the measured atom cloud lengths to begin to level off towards some constant value, due to the wings of the cloud being increasingly Zeeman shifted out of resonance with the imaging beam. This is not seen for the values plotted in Figure 6.19, so we conclude that it is valid to measure temperatures up to at least $110\,\mu$K in this way. Figure 6.19 can be used to measure the residual field of the magnetic trap. The temperature of a thermal cloud will only drop to zero when all the atoms are removed from the trap, i.e. when the rf frequency reaches the value where it is resonant with the minimum field of the trap. The extrapolated rf frequency at zero temperature therefore corresponds to the residual magnetic field. For the data presented in Figure 6.19, this is 1.71 MHz, corresponding to a residual axial field of 2.45 G. From this axial field, the radial trap frequency is calculated to be 440 Hz during evaporation. This method of measuring the residual magnetic field is more accurate than that presented in Section 6.7 as the atom cloud is much colder.

We are unable to cool the cloud further as the loss of atom number is too great — the regime of runaway evaporation is not reached during the rf ramp. Immediately after transfer from the CMOT, the atom cloud has a temperature of $80\,\mu$K and is held in a magnetic trap with radial frequency 90 Hz. Before the evaporation commences, the magnetic trap is adiabatically compressed to a radial trap frequency of 440 Hz. This increases the cloud temperature to $\sim 300\,\mu$K (Equation 6.11), giving an elastic collision rate of 21 Hz. The lifetime due to background loss is ~ 5 s, so the initial value of $\gamma_{el}/\gamma_{loss}$ is therefore only ~ 100, just slightly smaller than the value

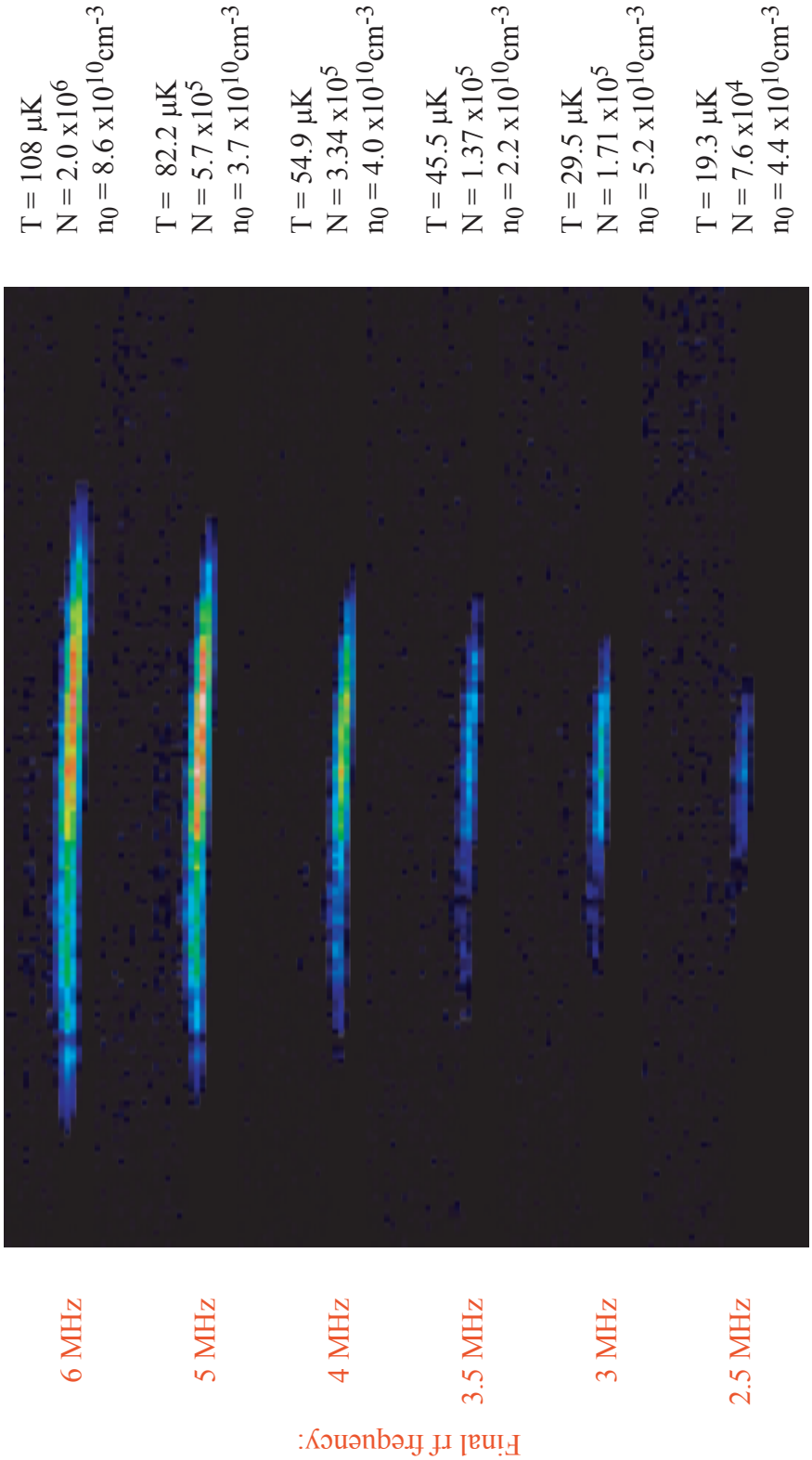

Figure 6.18 *Cooling the cloud by rf evaporation. The width of the images is 6 mm.*

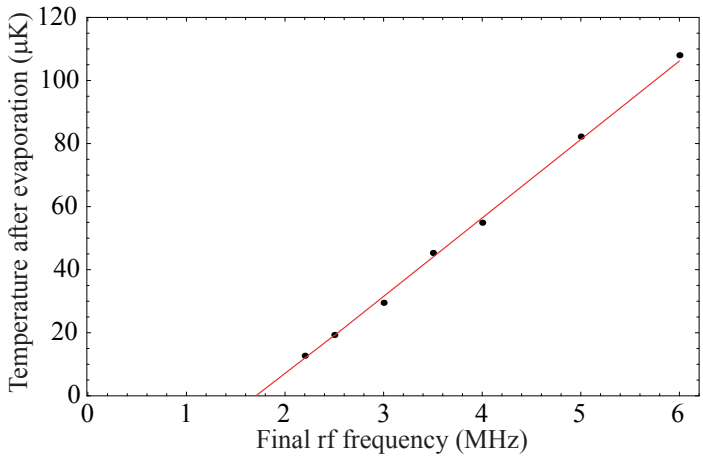

Figure 6.19 *Temperature vs final rf frequency of evaporative cooling ramp. This measurement gives an accurate value for the residual axial field of the trap, by Equation 6.26. The extrapolated frequency is 1.7 MHz, corresponding to 2.44 G axial field.*

for which runaway evaporation is possible. During the evaporation ramp described in this section, the atom number is drastically reduced, such that after evaporation to 5 MHz, the collision rate is reduced to 2 Hz. In practice, the magnetic trap can be compressed further to increase the initial collision rate, but this is limited by density-dependent losses. Optimization of evaporation will probably require control of the trap frequency as well as the rf frequency, in order to maintain a high collision rate, while avoiding increasing the density to the limit where 3-body losses occur. In addition, improvements to the magnetic trap lifetime should be possible, as the mirror-MOT lifetime is significantly higher (25–30 s). This would allow the rf frequency to be ramped more slowly, giving a longer time for rethermalization by elastic collisions.

Chapter 7

Conclusions

7.1 Summary

The central result of this thesis is that we have learned how to load atoms both magneto-optically and magnetically into an array of microscopic traps created using the field above a permanently magnetized videotape. The magneto-optical microtraps do not have very high numbers of atoms in them — typically 10^5 in each trap. However they are among the smallest MOTs ever produced, having a radius of less than $10\,\mu$m. We have not exploited this in the present thesis, but in future applications relating to QIP where small atom numbers are required, this method may well be of interest. The magnetic loading scheme was based on auxiliary current-carrying wires below the videotape surface. This allowed us to collect as many as 2×10^7 atoms in a magnetic trap. Compressing the trap, we have observed exceedingly high densities that result in a density-dependent loss of atoms due to three-body collisions. The low-density lifetime of trapped clouds has been studied in the range $30\,\mu$m – 1 mm from the surface. Over this range, we have found that atoms can be stored with a lifetime of 5.5 s, independent of height, indicating that atom–surface interactions remain negligible, even at these small distances from the surface. Indeed, the most exciting discovery of this thesis is that atoms stored above videotape seem to be significantly less perturbed than those above a metallic surface. We have also demonstrated that we can further cool the atom cloud in the magnetic trap by forced rf evaporative cooling. This has enabled us to reach temperatures as low as $10\,\mu$K and densities very close to the critical value needed to achieve BEC directly in the microtrap.

7.2 Future directions

Bose-Einstein condensation

The next stage of the experiment it to evaporatively cool the trapped clouds to BEC in the microtraps, opening up possibilities for coherent atom optics. This will enable further study of atom–surface interactions at low temperatures and also at smaller distances from the atom chip.

Atom transport

An atom 'conveyor-belt' [47, 129] can be realized by rotating the bias field, used to form the microtrap array, in the x–y plane. The entire array shifts by one wavelength of the recorded pattern for each rotation of the applied field. This will be an extremely useful device for transporting atoms on an integrated atom chip, for example between a storage region and an interaction region.[1] The transport range of the conveyor-belt is limited only by the length of the recorded tape. In the next generation of videotape experiments, it will be interesting to use this transport system to move atoms in and out of a microscopic optical cavity. Coupling between microtraps and optical microcavities has tremendous promise in the field of cavity QED and quantum information processing.

Recording media

Videotape has proved to be a reliable and versatile medium for atom optics experiments. It is simple to record different wavelengths on the surface, the minimum wavelength being limited to a few microns by the recording process. In this thesis we have used a $100\,\mu$m pattern — reducing this wavelength to $10\,\mu$m allows microtraps with a field gradient a factor of 10 higher to be realized. In this way, arrays of thousands of microtraps can be created on a single atom chip.

Future experiments may require smaller, more complex patterns. Should we wish to write patterns with sub-micron resolution, thin magnetic films, such as magneto-optical disk, may be a suitable alternative. The magnetization is written using a focused laser beam, allowing arbitrary patterns to be created. This would allow, for example, patterns for planar beamsplitters and interferometers to be created, similar to those based on microfabricated wires. Unlike microelectromagnet atom chips, miniaturization presents no difficulties caused by power dissipation.

[1] A related conveyor-belt, based on millimetre-scale current-carrying wires, has been demonstrated by the group of Jakob Reichel [46].

Bibliography

[1] W. Gerlach and O. Stern, *Der experimentelle Nachweis des magnetischen Moments des Silberatoms*, Zeitschrift f. Physik **8**, 110 (1921)

[2] N. F. Ramsey, *Molecular Beams* (Oxford: Oxford University Press, 1985)

[3] C. S. Adams and E. Riis, *Laser cooling and trapping of neutral atoms*, Prog. Quant. Electr. **21**, 1 (1997)

[4] H. Metcalf and P. van der Straten, *Cooling and trapping of neutral atoms*, Phys. Rep, **244**, 204 (1994)

[5] M. G. Prentiss and W. D. Phillips (eds.), *Atom Optics*, Proc. SPIE **2995** (1997)

[6] *Special Issue on Atom Optics*, Quantum Semiclass. Opt. **8** (1996)

[7] J. P. Dowling and J. Gea-Banacloche, *Evanescent Light-Wave Atom Mirrors, Resonators, Waveguides, and Traps*, Adv. At. Mol. Opt. Phys. **37**, 1 (1996)

[8] E. A. Hinds and I. G. Hughes, *Magnetic atom optics: mirrors, guides, traps, and chips for atoms*, J. Phys. D: Appl. Phys. **32**, R119 (1999)

[9] P. Rosenbusch, J. A. Retter, B. V. Hall, E. A. Hinds, F. Lison, D. Haubrich and D. Meschede, *Reflection of cold atoms by a cobalt single crystal*, Appl. Phys. B **70**, 661 (2000)

[10] T. Sleator, T. Pfau, V. Balykin and J. Mlynek, *Imaging and focusing of an atomic beam with a large period standing light wave*, Appl. Phys. B **54**, 375 (1992)

[11] J. J. McClelland, R. E. Sholten, E. C. Palm and R. J. Celotta, *Laser-focussed atomic deposition*, Science **262**, 877 (1993)

[12] W. G. Kaenders, F. Lison, A. Richter, R. Wynands and D. Meschede, *Imaging with an atomic beam*, Nature **375**, 214 (1995)

[13] P. J. Martin, B. G. Oldaker, A. K. Miklich and D. E. Pritchard, *Bragg scattering of atoms from a standing light wave*, Phys. Rev. Lett. **60**, 515 (1988)

[14] A. Landragin, L. Cognet, G. Zs. K. Horvath, C. I. Westbrook, N. Westbrook and A. Aspect, *A reflection grating fro atoms at normal incidence*, Europhys. Lett. **39**, 485 (1997)

[15] S. Durr, S. Kunze and G. Rempe, *Pendellosung oscillations in second-order Bragg scattering of atoms from a standing light wave*, Quant. Semiclass. Opt. **8**, 531 (1996)

[16] M. Key, I. G. Hughes, W. Rooijakkers, B. E. Sauer, E. A. Hinds, D. J. Richardson and P. G. Kazansky, *Propagation of cold atoms along a miniature magnetic guide*, Phys. Rev. Lett. **84**, 1371 (2000)

[17] N. H. Dekker, C. S. Lee, V. Lorent, J. H. Thywissen, S. P. Smith, M. Drndić, R. M. Westervelt and M. Prentiss, *Guiding neutral atoms on a chip*, Phys. Rev. Lett. **84**, 1124 (2000)

[18] J. J. Berkhout, O. J. Luiten, I. D. Setija, T. W. Hijmans, T. Mizusaki and J. T. M. Walraven, *Quantum reflection: Focusing of hydrogen atoms with a concave mirror*, Phys. Rev. Lett. **63**, 1689 (1998)

[19] B. Holst and W. Allison, *An atom-focusing mirror*, Nature **390**, 244 (1997)

[20] W. Ketterle, D. S. Durfee and D. M. Stamper-Kurn, *Making, probing and understanding Bose-Einstein condensates*, in *Proceedings of the International School of Physics – Enrico Fermi, Vol. 140*, edited by M. Inguscio, S. Stringari and C. Wieman (Tokyo: IOS Press, 1999)

[21] N. Schlosser, G. Reymond, I. Protsenko and P. Grangier, *Sub-poissonian loading of single atoms in a microscopic dipole trap* Nature **411**, 1024 (2001)

[22] D. Frese, B. Ueberholz, S. Kuhr, W. Alt, D. Schrader, V. Gomer and D. Meschede, *Single atoms in an optical dipole trap: Towards a deterministic source of cold atoms*, Phys. Rev. Lett. **85**, 3777 (2000)

[23] T. Calarco, E. A. Hinds, D. Jaksch, J. Schmiedmayer, J. I. Cirac, and P. Zoller, *Quantum gates with neutral atoms: Controlling collisional interactions in time-dependent traps*, Phys. Rev. A **61**, 022304 (2000)

[24] D. Jaksch, C. Bruder, J. I. Cirac, C. W. Gardiner and P. Zoller, *Cold Bosonic Atoms in Optical Lattices*, Phys. Rev. Lett. **81**, 31083111 (1998)

[25] C. J. Hood, M. S. Chapman, T. W. Lynn and H. J. Kimble, *Real-Time Cavity QED with Single Atoms*, Phys. Rev. Lett. **80**, 4157 (1998)

[26] P. Münstermann, T. Fischer, P. Maunz, P. W. H. Pinkse and G. Rempe, *Dynamics of Single-Atom Motion Observed in a High-Finesse Cavity*, Phys. Rev. Lett. **82**, 3791 (1999)

[27] E. A. Hinds, C. J. Vale and M. G. Boshier, *Two-Wire Waveguide and Interferometer for Cold Atoms*, Phys. Rev. Lett. **86**, 1462 (2001)

[28] W. Hänsel, J. Reichel, P. Hommelhoff and T. W. Hänsch, *Trapped-atom interferometer in a magnetic microtrap*, Phys. Rev. A **64**, 063607 (2001)

[29] E. Andersson, T. Calarco, R. Folman, M. Andersson, B. Hessmo and J. Schmiedmayer, *Multimode Interferometer for Guided Matter Waves*, Phys. Rev. Lett. **88**, 100401 (2002)

[30] D. S. Petrov, G. V. Shlyapnikov and J. T. M. Walraven, *Regimes of quantum degeneracy in trapped 1D gases*, Phys. Rev. Lett. **85**, 3745 (2000)

[31] A. Görlitz, J. M. Vogels, A. E. Leanhardt, C. Raman, T. L. Gustavson, J. R. Abo-Shaeer, A. P. Chikkatur, S. Gupta, S. Inouye, T. P. Rosenband and W. Ketterle, *Realization of Bose-Einstein condensates in lower dimensions*, Phys. Rev. Lett. **87**, 130402 (2001)

[32] R. Folman, P. Krger, D. Cassettari, B. Hessmo, T. Maier and J. Schmiedmayer, *Controlling Cold Atoms using Nanofabricated Surfaces: Atom Chips*, Phys. Rev. Lett. **84**, 4749 (2000)

[33] D. Müller, D. Z. Anderson, R. J. Grow, P. D. D. Schwindt, and E. A. Cornell, *Guiding Neutral Atoms Around Curves with Lithographically Patterned Current-Carrying Wires*, Phys. Rev. Lett. **83**, 5194 (1999)

[34] J. Fortagh, H. Ott, A. Grossmann and C. Zimmermann, *Microelectromagnets for trapping and manipulating ultracold atomic quantum gases*, Appl. Phys. Lett. **81**, 1146 (2002)

[35] J. Reichel, W. Hänsel and T. W. Hänsch, *Atomic micromanipulation with magnetic surface traps*, Phys. Rev. Lett. **83**, 3398 (1999)

[36] M. P. A. Jones, *Bose-Einstein condensation above a wire*, D. Phil. Thesis, University of Sussex (2002)

[37] C. Henkel, S. Pötting and M. Wilkens, *Loss and heating of particles in small and noisy traps*, Appl. Phys. B **69**, 379 (1999)

[38] J. Fortágh, H. Ott, S. Kraft and C. Zimmermann, *Surface Effects on a Bose-Einstein Condensate in a Magnetic Microtrap*, Phys. Rev. A **66**, 041604(R) (2002)

[39] M. P. A. Jones, C. J. Vale, K. Furusawa and E. A. Hinds, XV111 International Conference on Atomic Physics (Cambridge), p 75 (2002)

[40] A. E. Leanhardt, A. P. Chikkatur, D. Kielpinski, Y. Shin, T. L. Gustavson, W. Ketterle and D. E. Pritchard, *Propagation of Bose-Einstein Condensates in a Magnetic Waveguide*, Phys. Rev. Lett. **89**, 040401 (2002)

[41] S. Kraft, A. Günther, H. Ott, D. Wharam, C. Zimmermann and J. Fortágh, *Anomalous Longitudinal Magnetic Field near the Surface of Copper Conductors*, J. Phys. B: At. Mol. Opt. Phys. **35**, L469 (2002)

[42] H. Ott, J. Fortágh, G. Schlotterbeck, A. Grossmann and C. Zimmermann, *Bose-Einstein Condensation in a Surface Microtrap*, Phys. Rev. Lett. **87**, 230401 (2001)

[43] T. L. Gustavson, A. P. Chikkatur, A. E. Leanhardt, A. Görlitz, S. Gupta, D. E. Pritchard and W. Ketterle, *Transport of Bose-Einstein Condensates with Optical Tweezers*, Phys. Rev. Lett. **88**, 020401 (2002)

[44] D. Cassettari, B. Hessmo, R. Folman, T. Maier and J. Schmiedmayer *Beam Splitter for Guided Atoms*, Phys. Rev. Lett. **85**, 5483 (2000)

[45] D. Müller, E. A. Cornell, M. Prevedelli, P. D. D. Schwindt, A. Zozulya and D. Anderson, *A waveguide atom beamsplitter for laser-cooled neutral atoms*, Optics Lett. **25**, 1382 (2000)

[46] W. Hänsel, J. Reichel, P. Hommelhoff and T. W. Hänsch, *Magnetic conveyor belt for transporting and merging trapped atom clouds*, Phys. Rev. Lett. **86**, 608 (2001)

[47] E. A. Hinds, *Controlling cold atoms above a magnetic reflector*, Phil. Trans. R. Soc. Lond. A **357**, 1409 (1999)

[48] W. Hänsel, P. Hommelhoff, T. W. Hänsch and J. Reichel, *Bose-Einstein Condensation on a Microelectronic Chip*, Nature **413**, 498 (2001)

[49] T. W. Hänsch and A. Schawlow, *Cooling of gases by laser radiation*, Opt. Comm. **13**, 68 (1975)

[50] D. Wineland and H. Dehmelt, *Proposed* 10^{14} $\delta\nu < \nu$ *laser fluorescence spectroscopy on* Tl^+ *Mono-Ion Oscillator*, Bull. Am. Phys. Soc. **20**, 637 (1975)

[51] W. Phillips and H. Metcalf, *Laser deceleration of an atomic beam*, Phys. Rev. Lett., **48**, 596 (1982)

[52] S. Chu, L. Hollberg, J. Bjorkholm, A. Cable and A. Ashkin, *Three-dimensional viscous confinement and cooling of atoms by resonance radiation pressure*, Phys. Rev. Lett. **55**, 48 (1985)

[53] E. L. Raab, M. Prentiss, A. Cable, S. Chu and D. E. Pritchard, *Trapping of Neutral Sodium Atoms with Radiation Pressure*, Phys. Rev. Lett. **59**, 2631 (1987)

[54] P. D. Lett, R. N. Watts, C. I. Westbrook, W. D. Phillips, P. L. Gould and H. J. Metcalf, *Observation of atoms laser cooled below the Doppler limit*, Phys. Rev. Lett. **61**, 169 (1988)

[55] J. Fortagh, A. Grossman, C. Zimmermann and T. W. Hänsch, *Miniaturized Wire Trap for Neutral Atoms*, Phys. Rev. Lett. **81**, 5310 (1998)

[56] U. Volz and H. Schmoranzer, *Precision Lifetime Measurements on Alkali Atoms and on Helium by Beam-Gas-Laser Spectroscopy*, Physica Scripta **T65**, 48 (1996)

[57] P. D. Lett, W. D. Phillips, S. L. Rolston, C. E. Tanner, R. N. Watts and C. I. Westbrook, *Optical Molasses*, J. Opt. Soc. Am. B **6**, 2084 (1989)

[58] K. Lindquist, M. Stephens, C. Wieman, *Experimental and theoretical study of the vapor-cell Zeeman optical trap*, Phys. Rev. A **46**, 4082 (1992)

[59] J. Dalibard and C. Cohen-Tannoudji, *Laser cooling below the Doppler limit by polarization gradients: simple theoretical models*, J. Opt. Soc. Am. B **6**, 2023, (1989)

[60] A. M. Steane and C. J. Foot, *Laser cooling below the Doppler limit in a magneto-optical trap*, Europhys. Lett. **14**, 231 (1991)

[61] M. Drewsen, P. Laurent, A. Nadir, G. Santarelli, A. Clairon, Y. Castin, D. Grison and C. Salomon, *Investigation of sub-Doppler cooling effects in a cesium magneto-optical trap*, Appl. Phys. B **59**, 283 (1994)

[62] J. Ye, S. Swartz, P. Jungner and J. L. Hall, *Hyperfine structure and absolute frequency of the* ^{87}Rb $5P_{3/2}$ *state*, Opt. Lett. **21**, 1280 (1996)

[63] S. Bize, Y. Sortais, M. S. Santos, C. Mandache, A. Clairon and C. Salomon, *High-accuracy measurement of the* ^{87}Rb *ground-state hyperfine splitting in an atomic fountain*, Europhys. Lett. **45**, 558 (1999)

[64] G. Breit and I. I. Rabi, *Measurement of Nuclear Spin*, Phys. Rev. **38**, 2082 (1931)

[65] E. A. Cornell, C. Monroe and C. E. Wieman, *Multiply loaded, AC magnetic trap for neutral atoms*, Phys. Rev. Lett. **67**, 2439 (1991)

[66] I. I. Rabi, N. F. Ramsey and J. Schwinger, *Use of rotating coordinates in magnetic resonance problems*, Rev. Mod. Phys. **26**, 167 (1954)

[67] A. Messiah, *Quantum Mechanics, Vol. 2*, (Amsterdam: North Holland, 1961)

[68] E. Majorana, Nuovo Cim. **9**, 43 (1932)

[69] V. V. Vladimirskii, *Magnetic mirrors, channels an bottles for cold neutrons*, Sov. Phys. JETP **12**, 740 (1961)

[70] G. I. Opat, S. J. Wark and A. Cimmino, *Electric and magnetic mirrors and gratings for slowly moving neutral atoms and molecules*, Appl. Phys. B **54**, 396 (1992)

[71] T. M. Roach, H. Abele, M. G. Boshier, H. L. Grossman, K. P. Zetie and E. A. Hinds, *Realization of a magnetic-mirror for cold atoms*, Phys. Rev. Lett. **75**, 629 (1995)

[72] J. D. Jackson, *Classical Electrodynamics* 3rd edition (New York: Wiley, 1998)

[73] I. G. Hughes, P. A. Barton, T. M. Roach and E. A. Hinds, *Atom Optics with Magnetic Surfaces II: Microscopic Analysis of the "Floppy Disk" Mirror*, J. Phys. B **30**, 2119 (1997)

[74] P. A. Barton, *Retro-Reflection of Cold Rubidium Stoms from a Curved Magnetic Mirror*, D. Phil. Thesis, University of Sussex (1998)

[75] A. I. Sidorov, R. J. McLean, W. J. Rowlands, D. C. Lau, J. E. Murphy, M. Walciewicz, G. I. Opat and P. Hannaford, *Specular reflection of cold caesium atoms from a magnetostatic mirror*, Quantum Semiclass. Opt. **8**, 713 (1996)

[76] D. Meschede, I. Bloch, A. Goepfert, D. Haubrich, M. Kreis, F. Lison, R. Schutze and R. Wynands, *Atom optics with permanent magnetic components*, Proc. SPIE **2995**, 191 (1997)

[77] Specification Sheet AMPEX 398 Betacam SP Videocassettes (1998) Contact: Quantegy Europa Ltd., Commerce Park, Theale, RG7 4AB.

[78] S. A. Hopkins, E. A. Hinds, M. G. Boshier, *UHV-compatible magnetic material for atom optics*, Appl. Phys. B **73**, 51 (2001)

[79] P. Goldsmith, Quantegy, Private Communication (1998)

[80] F. Brailsford, *Physical Principles of Magnetism*, (D. Van Nostrand Company Ltd., 1966)

[81] P. Rosenbusch, *Atom Optics with an Adaptable Magnetic Reflector*, D. Phil. Thesis, University of Sussex (2001)

[82] P. J. Flanders, *An alternating-gradient magnetometer*, J. Appl. Phys. **63** 3940 (1988)

[83] P. J. Flanders, *A vertical force alternating-gradient magnetometer*, Rev. Sci. Instrum. **61** 839 (1990)

[84] Record head 0625D, read head 0626D, (19 mm gap width), Phi Magnetronics Specification Sheet (1998)
Contact: Mr. R. J. Pearce, Phi Magnetronics Ltd., Falmouth, England.

[85] E. D. Dahlberg and J.-G. Zhu, *Micromagnetic microscopy and modelling*, Physics Today, April Issue, 34 (1995)

[86] D. Rugar, H. J. Mamin, P. Guethner, S. E. Lambert, J. E. Stern, I. McFadyen and T. Yogi, *Magnetic force microscopy: General principles and application to longitudinal recording media*, J. Appl. Phys. **68**, 1169 (1990)

[87] The garnet film ($(Nd,Lu,Bi)_3(Fe,Al)_5O_{12}$) is kindly lent by Prof. Dieter Meschede at the University of Bonn, and was manufactured at the University of Osnabrück.

[88] R. P. Bertram, *Atomstrahlumlenkung mit Magnetbändern*, Diplomarbeit, University of Bonn (2000)

[89] C. E. Wieman and L. Hollberg, *Using diode lasers for atomic physics*, Rev. Sci. Instrum. **62**, 1 (1991)

[90] A. S. Arnold, J. S. Wilson and M. G. Boshier, *A simple extended-cavity diode laser*, Rev. Sci. Instrum. **69**, 1236 (1998)

[91] Thorlabs Model LD1255, Laser diode 250 mA precision constant current driver.

[92] Wavelength Electronics Temperature Controller MPT-5000

[93] C. Wieman and T. W. Hänsch, *Doppler-Free Laser Polarization Spectroscopy*, Phys. Rev. Lett. **36**, 1170 (1976)

[94] C. P. Pearman, C. S. Adams, S. G. Cox, P. F. Griffin, D. A. Smith and I. G. Hughes, *Polarisation spectroscopy of a closed atomic transition: applications to laser frequency locking*, J. Phys. B: At. Mol. Opt. Phys. **35**,5141 (2002)

[95] W. Demtröder, *Laser Spectroscopy, 2nd edition* (Springer Verlag, Berlin, 1998)

[96] U. Schünemann, H. Engler, R. Grimm, M. Weidemüller and M. Zielonkowski, *Simple scheme for tunable frequency offset locking of two lasers*, Rev. Sci. Intrum. **70**, 242 (1999)

[97] A. Yariv, *Optical electronics in modern communications*, 5th edition, (Oxford: Oxford University Press, 1997)

[98] J. V. Prodan, W. D. Phillips and H. Metcalf, *Laser Production of a Very Slow Monoenergetic Atomic Beam*, Phys. Rev. Lett. **49** 1149 (1982)

[99] K. Gibble, S. Chang and R. Legere, *Direct Observation of s-Wave Atomic Collisions*, Phys. Rev. Lett. **75**, 2666 (1995)

[100] Z. T. Lu, K. L. Corwin, M. J. Renn, M. H. Anderson, E. A. Cornell, and C. E. Wieman, *Low-Velocity Intense Source of Atoms from a Magneto-optical Trap*, Phys. Rev. Lett. **77**, 3331 (1996)

[101] Carl Wieman, Gwenn Flowers and Sarah Gilbert, *Inexpensive laser cooling and trapping experiment for undergraduate laboratories*, Am. J. Phys. **63**, 317 (1995)

[102] J. Fortagh, A. Grossman, T. W. Hänsch and C. Zimmerman, *Fast loading of a magneto-optical trap from a pulsed thermal source*, J. Appl. Phys. **84**, 6499 (1998)

[103] www.saesgetters.com

[104] C. V. Saba, *Reconstruction of a Cold Atom Cloud by Magnetic Focusing*, D. Phil. Thesis, University of Sussex (1999)

[105] C. G. Townsend, N. H. Edwards, C. J. Cooper, K. P. Zetie, C. J. Foot, A. M. Steane, P. Szriftgiser, H. Perrin, J. Dalibard, *Phase-space density in the magneto-optical trap*, Phys. Rev. A **52**, 1423 (1995)

[106] A. S. Arnold, *Preparation and Manipulation of an ^{87}Rb Bose-Einstein Condensate*, D. Phil. Thesis, University of Sussex (1999)

[107] K. B. Davis, M. O. Mewes, M. A. Joffe, M. R. Andrews and W. Ketterle, *Evaporative cooling of sodium atoms*, Phys. Rev. Lett. **74**, 5202 (1995)

[108] M. Prentiss, A. Cable, J. E. Bjorkholm, S. Chu, E. L. Raab and D. E. Pritchard, *Atomic-density-dependent losses in an optical trap*, Optics Lett. **13**, 452 (1988)

[109] R. Loudon, *The Quantum Theory of Light* 2nd edition (Oxford: Oxford University Press, 1983) p76

[110] T. Walker, D. Sesko and C. Wieman, *Collective Behaviour of Optically Trapped Neutral Atoms*, Phys. Rev. Lett. **64**, 408 (1990)

[111] W. Petrich, M. H. Anderson, J. R. Ensher and E. A. Cornell, *Behaviour of atoms in a compressed magneto-optical trap*, J. Opt. Soc. Am. B **11**, 1332 (1994)

[112] M. T. DePue, S. L. Winoto, D. J. Han, D. S. Weiss, *Transient compression of a MOT and high intensity fluorescent imaging of optically thick clouds of atoms*, Opt. Commun. **180**, 73 (2000)

[113] W. Salzmann, Atoms in a long magneto-optical trap, Diplomarbeit, University of Tübingen/University of Sussex (2001)

[114] J. Dalibard, *Laser cooling of an optically thick gas: the simplest radiation pressure trap?*, Opt. Commun. **68**, 203 (1988)

[115] D. W. Sesko, T. G. Walker and C. E. Wieman, *Behaviour of neutral atoms in a spontaneous force trap*, J. Opt. Soc. Am. B **8**, 946 (1991)

[116] A. M. Steane, M. Chowdhury and C. J. Foot, *Radiation force in the magneto-optical trap*, J. Opt. Soc. Am. B **9**, 2142 (1992)

[117] C. D. Wallace, R. P. Dinneen, K. N. Tan, T. T. Grove and P. L. Gould, *Isotopic Difference in Trap Loss Collisions of Laser Cooled Rubidium Atoms*, Phys. Rev. Lett. **69** 897 (1992)

[118] D. Sesko, T. Walker, C. Monroe, A. Gallagher and C. Wieman, *Collisional Losses from a Light-Force Atom Trap*, Phys. Rev. Lett. **63**, 961 (1989)

[119] B. Ueberholz, S. Kuhr, D. Frese, D. Meschede and V. Gomez, *Counting cold collisions*, J. Phys B **33**, L135 (2000)

[120] M. Arndt, M. Ben Dahan, D. Guéry-Odelin, M. W. Reynolds and J. Dalibard, *Observation of a Zero-Energy Resonance in Cs-Cs Collisions*, Phys. Rev. Lett. **79**, 625 (1997)

[121] J. P. Burke, J. L. Bohn, B. D. Esry and C. H. Greene, *Prospects for Mixed-Isotope Bose-Einstein Condensates in Rubidium*, Phys. Rev. Lett. **80**, 2097 (1998)

[122] P. S. Julienne, F. H. Mies, E. Tiesinga and C. J. Williams *Collisional stability of double Bose condensates*, Phys. Rev. Lett. **78**, 1880 (1997)

[123] J. Söding, D. Guéry-Odelin, P. Desbiolles, F. Chevy, H. Inamori and J. Dalibard, *Three-body decay of a rubidium Bose-Einstein condensate*, Appl. Phys. B **69**, 257 (1999)

[124] Y. Kagan, B. V. Svistunov, G. V. Shlyapnikov, JETP Lett. **42**, 209 (1985)

[125] E. A. Burt, R. W. Ghrist, C. J. Myatt, M. J. Holland, E. A. Cornell and C. E. Wieman, *Coherence, correlations and collisions: what one learns about Bose-Einstein condensates from their decay*, Phys. Rev. Lett. **79**, 337 (1997)

[126] B. D. Esry, C. H. Greene and J. P. Burke, *Recombination of three atoms in the ultracold limit*, Phys. Rev. Lett. **83**, 1751 (1999)

[127] W. Ketterle and N. J. van Druten, *Evaporative cooling of trapped atoms*, Advance in Atomic, Molecular and Optical Physics, **37**, 181 (1996)

[128] O. J. Luiten, M. W. Reynolds and J. T. M. Walraven, *Kinetic theory of the evaporative cooling of a trapped gas*, Phys. Rev. A **53**, 381 (1996)

[129] P. Rosenbusch, B. V. Hall, I. G. Hughes, C. V. Saba and E. A. Hinds, *Manipulation of cold atoms using a corrugated magnetic reflector*, Phys. Rev. A **61**, 031404 (2000)

Appendix A

Clebsch-Gordan coefficients

		$F=1$			$F=2$				
F'	m_F	-1	0	+1	-2	-1	0	+1	+2
0	0	$\sqrt{1/3}$	$\sqrt{1/3}$	$\sqrt{1/3}$	0	0	0	0	0
1	-1	$\sqrt{5/12}$	$\sqrt{5/12}$	0	$\sqrt{1/10}$	$\sqrt{1/20}$	$\sqrt{1/60}$	0	0
	0	$\sqrt{5/12}$	0	$\sqrt{5/12}$	0	$\sqrt{1/20}$	$\sqrt{1/15}$	$\sqrt{1/20}$	0
	+1	0	$\sqrt{5/12}$	$\sqrt{5/12}$	0	0	$\sqrt{1/60}$	$\sqrt{1/20}$	1/10
2	-2	$\sqrt{1/2}$	0	0	$\sqrt{1/3}$	$\sqrt{1/6}$	0	0	0
	-1	$\sqrt{1/4}$	$\sqrt{1/4}$	0	$\sqrt{1/6}$	$\sqrt{1/12}$	$\sqrt{1/4}$	0	0
	0	$\sqrt{1/12}$	$\sqrt{1/3}$	$\sqrt{1/12}$	0	$\sqrt{1/4}$	0	$\sqrt{1/4}$	0
	+1	0	$\sqrt{1/4}$	$\sqrt{1/4}$	0	0	$\sqrt{1/4}$	$\sqrt{1/12}$	$\sqrt{1/6}$
	+2	0	0	$\sqrt{1/2}$	0	0	0	$\sqrt{1/6}$	$\sqrt{1/3}$
3	-3	0	0	0	1	0	0	0	0
	-2	0	0	0	$\sqrt{1/3}$	$\sqrt{2/3}$	0	0	0
	-1	0	0	0	$\sqrt{1/15}$	$\sqrt{8/15}$	$\sqrt{2/5}$	0	0
	0	0	0	0	0	$\sqrt{1/5}$	$\sqrt{3/5}$	$\sqrt{1/5}$	0
	+1	0	0	0	0	0	$\sqrt{2/5}$	$\sqrt{8/15}$	$\sqrt{1/15}$
	+2	0	0	0	0	0	0	$\sqrt{2/3}$	$\sqrt{1/3}$
	+3	0	0	0	0	0	0	0	1

Table A.1 *Clebsch-Gordan coefficients for transitions from the ground state $|F, m_F\rangle$ to the exited state $|F', m'_F\rangle$ in ^{87}Rb.*

Appendix B

MFM analysis

The analysis in this section helps us to obtain detailed quantitative information from the MFM scans, by considering the response of the tip to magnetic forces above the surface. It follows the treatment given in [73]. The MFM tip is approximated as a harmonic oscillator of natural frequency $\omega_0 = \sqrt{\kappa/m}$. When it experiences an additional force F_y, the equation of motion becomes:

$$m\ddot{y} = -\kappa y + F_y. \tag{B.1}$$

By making a Taylor expansion of the force: $F_y = F_0 + F_y' y + \ldots$, the shifted resonance frequency is obtained:

$$\begin{aligned} \omega &= \sqrt{(\kappa - F_y')/m} \\ &\simeq \omega_0(1 - \frac{F_y'}{2\kappa}). \end{aligned} \tag{B.2}$$

The MFM measures phase shifts due to this frequency shift, hence the MFM signal is proportional to the vertical force gradient F_y'. This is valid for the approximation that perturbations are small and constant over the range of the cantilever motion. Measured phase shifts are typically $< 10°$.

To calculate the force gradient, we make the approximation that the magnetic moment of the tip, $\boldsymbol{\mu}$, arises from a uniform, vertical magnetization. The dipole interaction, $E = -\boldsymbol{\mu} \cdot \mathbf{B}$, then gives rise to a force on the tip which depends only on the vertical, y-component of the field, $\mathbf{B}$:

$$\mathbf{F} = -\nabla E = \mu \nabla B_y \tag{B.3}$$

The MFM tip scans the magnetic field at a distance of only a few microns from the videotape surface. At such distances it is not possible to neglect the effects of higher

harmonics (as in Section 2.3.1). The periodic magnetic field above the videotape surface is given by:

$$\begin{pmatrix} B_x \\ B_y \end{pmatrix} = \sum_{n=0}^{\infty} B_n e^{-nky} \begin{pmatrix} -\cos(nkx + \delta_n) \\ +\sin(nkx + \delta_n) \end{pmatrix}, \tag{B.4}$$

where B_n is the field strength due to the nth harmonic at the surface and the recorded wavelength is $\lambda = 2\pi/k$. (c.f. Equations 2.39 and 2.42). Hence, the nth Fourier component of the vertical force gradient is:

$$\begin{aligned} F'_y(nk) &= \mu(nk)^2 B_n \sin(nkx + \delta_n) e^{-nky} \\ &= \xi_n B_n \sin(nkx + \delta_n) e^{-nky}. \end{aligned} \tag{B.5}$$

So far we have neglected the details of the magnetic tip geometry, its finite size and magnetization. However, [73] shows that integrating over the volume of an arbitrary magnetic tip geometry yields an equation for the force gradient of the same form as Equation B.5. Therefore we can write

$$\text{MFM Signal} = \sum_n \xi_n B_n \sin(nkx + \varphi_n) e^{-nky} \tag{B.6}$$

where ξ_n and φ_n now include the effects of averaging over the tip volume and allow for the fact that the tip responds to different frequencies with different sensitivities. For a tip of negligible size, Equation B.5 predicts that $\xi_n \propto n^2$. However, for a typical MFM tip, [73] has shown experimentally that ξ_n is roughly constant, in agreement with integration over realistic finite-sized tip geometries.

Appendix C

Doppler-free polarization spectroscopy

This Appendix gives the derivation of the lineshape quoted in Equation 4.1 of Section 4.1.4 for the lineshape of the polarization spectroscopy signal.

Before traversing the vapour cell, the probe beam is linearly polarized at an angle ϕ to the axis of the 'analyser' polarizing beam cube. The electric field vector of the beam is written:

$$\mathbf{E} = \begin{pmatrix} E_x \\ E_y \end{pmatrix} = E_0 \begin{pmatrix} \cos\phi \\ \sin\phi \end{pmatrix}. \tag{C.1}$$

The linear polarization of the probe beam can be considered as the sum of two opposite circular polarizations, rotating in the same and opposite sense as the pump beam polarization:

$$\begin{aligned} \mathbf{E} &= E^+ + E^- \\ &= E_0 \left(\frac{e^{-i\phi}}{2} \begin{pmatrix} 1 \\ i \end{pmatrix} + \frac{e^{i\phi}}{2} \begin{pmatrix} 1 \\ -i \end{pmatrix} \right), \end{aligned} \tag{C.2}$$

On traversing the vapour cell, of length L, the two circularly polarized components of the probe beam acquire different phases:

$$\mathbf{E} = E_0 \left(\frac{e^{-i\phi}}{2} \begin{pmatrix} 1 \\ i \end{pmatrix} e^{-iwn^+L/c} e^{-\alpha^+ L/2} + \frac{e^{i\phi}}{2} \begin{pmatrix} 1 \\ -i \end{pmatrix} e^{-iwn^-L/c} e^{-\alpha^- L/2} \right), \tag{C.3}$$

where $n^\pm$ are the refractive indices of the gas for the $\sigma^\pm$ components, and $\alpha^\pm$ are the corresponding absorption coefficients. (In practice, there are additional phase shifts due to the birefringent windows of the vapour cell. These are neglected here

for the sake of simplicity.) Defining average and difference quantities:

$$n = \frac{1}{2}(n^+ + n^-); \qquad \Delta n = n^+ - n^-;$$
$$\alpha = \frac{1}{2}(\alpha^+ + \alpha^-); \qquad \Delta\alpha = \alpha^+ - \alpha^-, \tag{C.4}$$

Equation C.3 becomes:

$$\mathbf{E} = E_0\, e^{-iwnL/c}\, e^{-\alpha L/2} \left(\frac{e^{-i\phi}}{2} \begin{pmatrix} 1 \\ i \end{pmatrix} e^{-i\Delta} + \frac{e^{i\phi}}{2} \begin{pmatrix} 1 \\ -i \end{pmatrix} e^{+i\Delta} \right), \tag{C.5}$$
$$\text{with} \qquad \Delta = \frac{L}{2}\left(\frac{w\Delta n}{c} - i\frac{\Delta\alpha}{2} \right).$$

The difference signal, $S = E_x E_x^* - E_y E_y^*$ is then given by:

$$\begin{aligned} S &= |E_0|^2\, e^{-\alpha L} \left(\cos^2(\phi + w\Delta nL/2c) - \sin^2(\phi + w\Delta nL/2c) \right) \\ &= |E_0|^2\, e^{-\alpha L} \cos(2\phi + w\Delta nL/c) \\ &= |E_0|^2\, e^{-\alpha L} \left(\cos(2\phi)\cos(w\Delta nL/c) - \sin(2\phi)\sin(w\Delta nL/c) \right). \end{aligned} \tag{C.6}$$

Since the absorption $\Delta\alpha$ is Doppler-free, as in standard saturated absorption spectroscopy, the lineshape of $\Delta\alpha$ is a Lorentzian:

$$\Delta\alpha(\omega) = \frac{\Delta\alpha(\omega_0)}{1 + x^2} \qquad \text{with} \qquad x = \frac{\omega_0 - \omega}{\gamma/2} \tag{C.7}$$

where γ is the power-broadened half-width and ω_0 is the centre frequency. Also, the Kramers-Kronig dispersion relation relates the refractive index to the absorption coefficient:

$$\Delta n^{\pm} = \frac{\Delta\alpha\, x}{\omega/c}. \tag{C.8}$$

Substituting Equations C.7 and C.8 into Equation C.6 gives:

$$S = |E_0|^2\, e^{-\alpha L} \left(\cos(2\phi)\cos(L\,\Delta\alpha_0 \frac{x}{1+x^2}) - \sin(2\phi)\sin(L\,\Delta\alpha_0 \frac{x}{1+x^2}) \right). \tag{C.9}$$

The frequency dependence of the signal depends on the relative orientation of the probe beam polarization and the analyser. Assuming the birefringence in the cell is small, an angle close to $\phi = \pi/4$, as used in this set-up, gives a dispersion shaped signal:

$$S = |E_0|^2\, e^{-\alpha L} L\,\Delta\alpha_0 \frac{x}{1+x^2}. \tag{C.10}$$

Appendix D

Bakeout procedure

After each opening of the chamber, a careful bakeout procedure is followed, in order to attain the lowest possible pressure. The chamber is rough-pumped by a pumping station (turbo-molecular pump backed by a rotary pump) connected to the chamber via a bakeable gate valve. The entire chamber is baked by wrapping heater tape around the body of the chamber and heating it to around 100 °C. The maximum baking temperature is limited by the videotape, which shows signs of chemical decomposition at temperatures above 120 °C (see Section 3.2.1). After a couple days of baking (typically a weekend) the getter pump is activated by passing a current of 4 A through it for 20 minutes. During activation, the getter pump releases a large amount of gas, which is pumped away by the turbo pump. After this initial pressure rise, the activated getter pump steadily reduces the pressure. The rubidium dispenser is then activated by gradually increasing the current to 5 A and then holding this current constant for a further 5 hours. This must be done very slowly, as a pressure rise greater than one order of magnitude would lead to contamination of the dispenser [102]. These activation procedures generally take an entire day. After this, the ion pump is run continuously. Once the pressure stabilizes, the gate valve is closed and the bake continues until the pressure is stable once more. At this point, the ion pump current is usually reading a few μA, corresponding to $< 5\times10^{-9}$ Torr. The heater tapes are then switched off and the chamber cools. Once the chamber cools the ion pump current reading goes off-scale (i.e. below 10^{-9} Torr). The lifetime of the MOT (~ 25 s) is consistent with a pressure of order 10^{-10} Torr.

Appendix E

Circuit diagrams

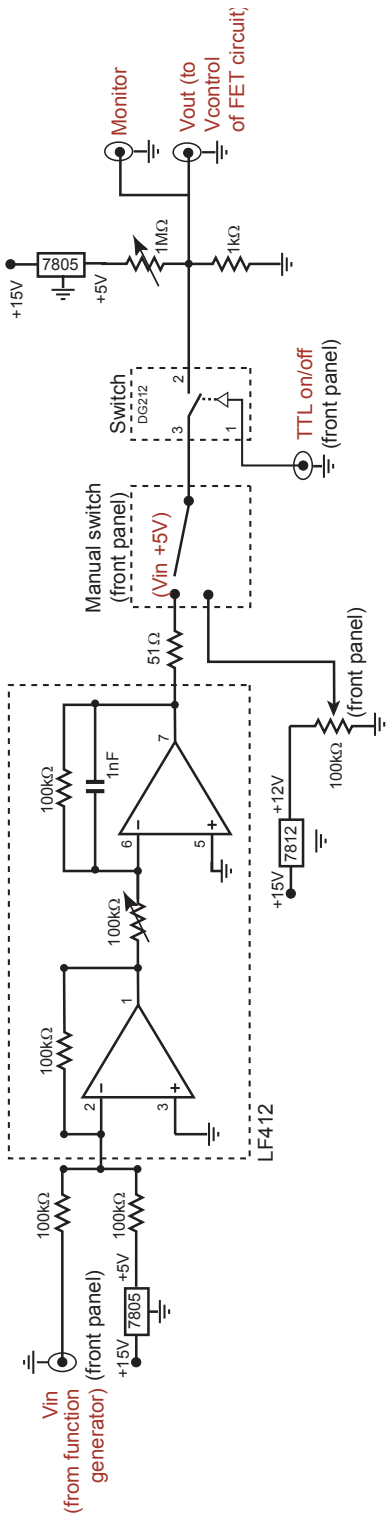

The front panel switch selects input from potentiometer (manual control) or from TTL input (Vin). Vin is the function generator output (range -5 to +5V), so is summed with 5V to shift range (0 to10V) . An electronic switch, computer controlled by a TTL line, switches the output on and off. The final stage of the circuit adds a small voltage (0.5mV) such that Vout is always slightly positive. (Vout is the gate input to the FET circuit (chip wire/bias field coils current control circuit) , which is maintained in a state with active feedback by keeping the gate voltage just above zero.)

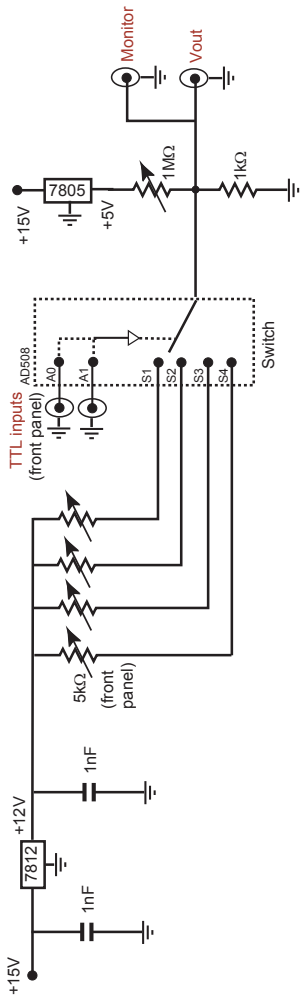

This circuit supplies an input voltage to the FET circuit which controls the atom chip end wires/cancelling bias coils. Two TTL lines select between 4 preset voltage levels. A small voltage (0.5mV) is added to the output, as above, such that Vout is always slightly positive.

Figure E.1 *Switching circuits for control voltage to FET circuits.*